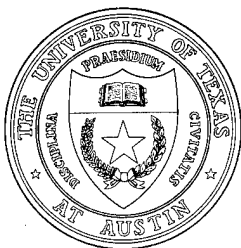


**The Influence of Geometric Imperfections on
Nonlinear Vibrations of Circular Rings**
Technical Report under Applied Research Laboratories Independent Research and
Development Program and Grant N00014-90-J-1366

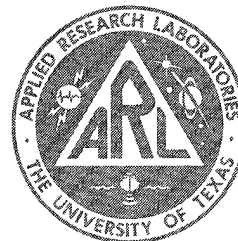
Paul Daniel Till

Applied Research Laboratories
The University of Texas at Austin
P. O. Box 8029 Austin, TX 78713-8029



2 February 1995

Technical Report



Approved for public release;
distribution is unlimited.

Prepared for:
Office of Naval Research
Department of the Navy
Arlington, VA 22217-5660

19960523 131

DEMO QUALITY UNCLASSIFIED 1

UNCLASSIFIED

REPORT DOCUMENTATION PAGE			Form Approved OMB No. 0704-0188	
Public reporting burden for this collection of information is estimated to average 1 hour per response, including the time for reviewing instructions, searching existing data sources, gathering and maintaining the data needed, and completing and reviewing the collection of information. Send comments regarding this burden estimate or any other aspect of this collection of information, including suggestions for reducing this burden, to Washington Headquarters Services, Directorate for Information Operations and Reports, 1215 Jefferson Davis Highway, Suite 1204, Arlington, VA 22202-4302, and to the Office of Management and Budget, Paperwork Reduction Project (0704-0188), Washington, DC 20503.				
1. AGENCY USE ONLY (Leave blank)		2. REPORT DATE 2 Feb 95		3. REPORT TYPE AND DATES COVERED technical
4. TITLE AND SUBTITLE The Influence of Geometric Imperfections on Nonlinear Vibrations of Circular Rings, Technical Report under Applied Research Laboratories Independent Research and Development Program and Grant N00014-90-J-1366			5. FUNDING NUMBERS ARL:UT IR&D Program N00014-90-J-1366	
6. AUTHOR(S) Till, Paul Daniel				
7. PERFORMING ORGANIZATION NAMES(S) AND ADDRESS(ES) Applied Research Laboratories The University of Texas at Austin P.O. Box 8029 Austin, Texas 78713-8029			8. PERFORMING ORGANIZATION REPORT NUMBER ARL-TR-95-3	
9. SPONSORING/MONITORING AGENCY NAME(S) AND ADDRESS(ES) Applied Research Laboratories Office of Naval Research The University of Texas at Austin Department of the Navy Austin, TX 78713-8029 Arlington, VA 22217-5660			10. SPONSORING/MONITORING AGENCY REPORT NUMBER	
11. SUPPLEMENTARY NOTES				
12a. DISTRIBUTION/AVAILABILITY STATEMENT Approved for public release; distribution is unlimited.			12b. DISTRIBUTION CODE	
13. ABSTRACT (Maximum 200 words) (see reverse side)				
14. SUBJECT TERMS bispectrum ring equations circular rings wavenumber decomposition nonlinear vibrations			15. NUMBER OF PAGES 102	
			16. PRICE CODE	
17. SECURITY CLASSIFICATION OF REPORT UNCLASSIFIED	18. SECURITY CLASSIFICATION OF THIS PAGE UNCLASSIFIED	19. SECURITY CLASSIFICATION OF ABSTRACT UNCLASSIFIED	20. LIMITATION OF ABSTRACT SAR	

13. Circular rings are a common, important component in aerospace and marine structures. Investigating the linear and nonlinear vibrations, as well as the transfer of energy in the wavenumber domain, of these structures is essential to understanding their acoustic radiation characteristics. Analytical, numerical, and experimental examinations were performed to address these issues. The analytical study showed that the inclusion of nonlinear features provides for the nonlinear transition of energy from higher order wavenumber responses to lower order wavenumber responses. Also, the presence of imperfections enhances the nonlinear, quadratic features of the response as well as provides for additional energy transfer to low order wavenumbers, now due to linear coupling. The numerical simulation verifies these results. A higher order spectral processing function, the bicoherence, was used to detect and quantify the quadratic features of the simulated response. In the experimental phase of the study, the response of two rings of different thickness to radius ratios and imperfection compositions were tested. The rings were spatially sampled and the data collected was wavenumber filtered such that the response of each wavenumber was extracted. The experimental results submit evidence of the transfer of energy from higher wavenumber responses to the $n=0$ wavenumber response. Also, as indicated by the bicoherence, quadratic features of the $n=0$ wavenumber response are enhanced by the presence of imperfections.

Table of Contents

Preface.....	v
Acknowledgments.....	vii
Chapter 1: Introduction	1
1.1 Motivation for Studying Circular Rings with Imperfections	1
1.2 Historical Development	4
1.3 Overview	7
Chapter 2: Derivation of Ring Equations	9
2.1 Derivation of Equations without Imperfections	9
2.2 Derivation of Equations Including Imperfections	23
Chapter 3: Introduction to Higher Order Spectral Processing	32
3.1 Definition of the Discrete Fourier Transform	33
3.2 The Power Spectrum	33
3.3 The Bispectrum	34
3.4 Application and Interpretation of the Bispectrum	36
Chapter 4: Numerical Simulation of Ring Vibrations	41
4.1 Motivation for Numerical Simulation	41
4.2 Implementation of Numerical Simulation	42
4.3 Discussion of Numerical Solution Results	44
Chapter 5: Experimental Procedure and Results	60
5.1 Description of Experimental Setup	60
5.2 Experimental Procedure	63
5.3 Experimental Results and Discussion	66

Chapter 6: Conclusions and Future Work	81
6.1 Conclusions	81
6.2 Future Work	82
Appendix A: Data Reduction Procedure	84
Appendix B: Additional Experimental Results	87
References	95

Preface

This material was originally published in May 1994 as a thesis, in partial fulfillment of the requirements for the degree of Master of Science in Engineering, The University of Texas at Austin.

This page intentionally left blank.

Acknowledgments

A project such as this is never completed solely through the efforts of the author. Thus, now is the time to express my gratitude to all those who contributed. Hopefully, no one is left out. I would like to thank Dr. Ronald Stearman for providing me with this exciting and rewarding opportunity. Thanks also for allowing me the freedom to explore this area of research and for your assistance in this project's completion. I also express gratitude to Dr. Gary Wilson for not only serving as the second reader of this thesis, but for furnishing an exemplary professional environment in which to conduct this research at the Applied Research Labs. I have gained a great deal of valuable experience under your supervision. Financial support for this project was provided by the Office of Naval Research and ARL Independent Research and Development Program funds.

Appreciation is also granted to Dr. Marti Barlett of the Applied Research Labs. Dr. Barlett's effort in the development and modification of the laser Doppler vibrometer measurement system proved essential to the success of this research project. I'll never forget that late afternoon when, after hours of collective, unsuccessful brainstorming and unabashed guessing, we were enlightened by the revelation, "It's the path links, stupid!" Thanks as well to Andy Anderson and Dave Gage for their assistance in the attenuation of the 60 cycle noise contamination. Gary and Marti, you guys helped out a little there, too, now didn't you? Also, thanks to the ARL Machine Shop crew, who machined the components of the experimental set-up.

I also wish to thank Doug Fox who served not only as a advisor but also as a friend, when all this seemed so confusing and new. Your research laid the groundwork for this project and made my job easier. I express immense gratitude to Dr. Jay Lamb, who executes the duties of good friend and structural mechanics/dynamics consultant with equal aptitude. You have provided me with an excellent example of how an engineer should approach his profession and assure quality in his performance.

This page intentionally left blank.

CHAPTER 1: INTRODUCTION

This thesis addresses the influence of geometric imperfections on nonlinear vibrations of circular rings, with an emphasis on the distribution of the response in the wavenumber domain. This chapter provides introductory information relevant to studying the nonlinear, transverse vibrations of circular rings. Motivating factors for investigating the vibrations of circular rings with geometric imperfections are presented. Historical references reflecting research in the field of nonlinear vibrations of circular rings and cylindrical shells are given, as well. The research on circular ring vibrations completed by Fox (1993), which led to the present study, is summarized. Finally, overviews of the research approach employed in this study as well as the organization of this thesis are submitted.

1.1 Motivation for Studying Circular Rings with Imperfections

Studying the vibrations of circular rings is beneficial for several reasons. Circular rings provide a simplified geometry with only one spatial coordinate. Effects associated with circumferential and radial wavenumbers are therefore not complicated by the presence of axial modes. The coupling of radial and circumferential wavenumber responses with axial modes is a condition present for cylindrical shells which is not present when considering circular rings.

However, circular rings can still provide some insight into the vibrations of cylindrical shells. Evensen (1964) was led to circular ring vibrations while investigating the nonlinear breathing mode response of a cylindrical shell. Vibration of circular rings represents a class of vibrations of cylindrical shells for which the axial variation is not present. Information concerning radial wavenumber responses of a shell is gleaned by investigating a limiting case of the shell, that is, the ring.

Circular rings are an integral component of many structures. Pressure vessels contain rings to improve the structural integrity and increase the buckling load of these structures. Rings are also common in aerospace structures. An aircraft's fuselage possesses supporting rings to increase the strength of this member, which must support a substantial pressure differential necessary to pressurize the interior. Missiles and launch platforms also contain circular rings to increase the stiffness of their thin shell outer structures and improve the buckling and flutter characteristics of these vehicles. Rings are also an integral component of marine structures. The hull of a submarine is reinforced with numerous ring stiffeners located throughout its length.

Studying the influence of geometric imperfections on the vibration and buckling characteristics of cylindrical shells and circular rings has proven to be a significant area of research. The modified vibration characteristics of shells with imperfections have been used to help predict their buckling loads, since imperfections significantly influence the buckling behavior of shells. Imperfections can also enhance the nonlinear vibration features of circular rings and cylindrical shells. O'Donnell (1990) exhibited the influence imperfections can have on the quadratic features of cylindrical shell vibrations. Fox (1993) displayed how the quadratic features of the circular ring response are enhanced by the presence of imperfections.

Studies on the nonlinear vibrations of circular rings show evidence of energy transition from higher order wavenumbers to lower order wavenumbers. In Evensen's (1964) study of inextensional vibrations of circular rings, energy was transferred from flexural wavenumber responses, $n \geq 2$, to the $n=0$ wavenumber response due to nonlinear coupling between these modes. This transfer manifested itself in the presence of a frequency twice that of the excitation frequency responding at the $n=0$ wavenumber. Evensen displayed experimental evidence of this phenomenon. Evensen (1967) also presented a similar energy transfer mechanism present for nonlinear, cylindrical shell vibrations.

In order to understand how the acoustic radiation from marine platforms can be decreased, the linear and nonlinear vibrations of circular rings must be understood. These ring stiffeners, when excited, can produce acoustic waves in the surrounding medium as well as modify the response of the shell. Corrado (1993) exhibited the importance of ring stiffeners in the scattered acoustic field of an insonified cylindrical shell. Observation of target strength measurements of a ring stiffened shell revealed evidence of ring resonance vibrations contributing significantly to the acoustic field.

Vibrations of circular rings need to be investigated to gain insight into the problem of acoustic radiation from rings and shells. Studying the energy transfer mechanism exhibited in nonlinear, circular ring vibrations is important, since not all radial wavenumbers of a ring or shell generate sound with equal effectiveness. Lower order wavenumbers radiate acoustic energy much more efficiently than do the higher order wavenumbers. The most efficient sound radiator is the $n=0$ wavenumber, known as the breathing mode. This motion is modeled acoustically as a monopole; thus, observing the pressure field around the monopole, the pressure drops as $\frac{1}{R}$, where r is distance from the source. This constitutes a sound pressure level (SPL) drop of 6 dB for every doubling of distance. The $n=1$ wavenumber response, known as the rigid body mode, is modeled as an acoustic dipole, for which efficiency is less than that of the monopole. The drop-off for this mode goes as $\frac{1}{R^2}$ in the nearfield ($kR \ll 1$, k =acoustic wavenumber). This represents a 12 dB drop in the SPL for every doubling of distance in the nearfield and a drop-off as $\frac{1}{R}$, or 6 dB, in the farfield ($kr \gg 1$) (Blackstock, 1993). The first flexural response mode corresponds to the $n=2$ wavenumber. It is modeled acoustically as a quadrupole and radiates sound less efficiently than the monopole or dipole. A similar trend continues for the $n=3$ and higher wavenumbers. Therefore, these lower order wavenumber responses are the most significant contributors to the acoustic radiation of rings and shells.

As will be discussed in the next section, the inclusion of initial, geometric imperfections play a significant role in the vibrations of circular rings and cylindrical shells. From a practical consideration, including imperfections in a model of ring vibrations should only improve the accuracy of the model when compared to actual specimens. Whether because of the manufacturing process or processes incidental in nature, it is expected that rings contain some degree of imperfections. An analytical, numerical and experimental approach which includes imperfections should illustrate to what extent individual imperfection components in terms of their amplitudes, wavenumbers, and spatial orientations are significant.

1.2 Historical Development

The study of circular rings and shell structures has an extensive history. Several authors have also studied nonlinear vibration problems associated with cylindrical shells and circular rings. Chu (1961) derived a set of nonlinear shallow shell equations used frequently in the literature. Cwach and Stearman (1968) studied nonlinear flexural vibrations of circular cylinders. They examined experimentally the hysteresis and jump phenomenon exhibited in the amplitude-frequency response curves for nonlinear vibrations as well as the companion mode instability. Mack and Yew (1968) made a similar investigation of the nonlinear flexural vibrations of a circular ring. Liu and Arbocz (1985b) analyzed the nonlinear, dynamic response of a shell including imperfections, as well as ring and longitudinal stiffeners. Perhaps the most comprehensive investigation of nonlinear circular ring vibrations was produced by Evensen (1964). In this work, Evensen derives the equations of motion for inextensional and extensional ring vibrations, solves them analytically, and performs an experimental study to verify and refine these results.

In addition to the extensive history of cylindrical shell and ring vibrations, the influence of imperfections on these vibrations has also received considerable attention. Imperfections were first investigated as a mechanism responsible for the

discrepancy between theoretical and experimental buckling loads of cylindrical shells (Arbocz and Babcock, 1969). Rosen and Singer (1974) extended this research to examine the influence of imperfections on the vibrations of cylindrical shells. They found that imperfections had a significant influence on the vibration characteristics of cylindrical shells. They proposed that imperfection measurements could be made simply by observing the discrepancy between the natural frequencies of a shell specimen and those predicted of a perfect shell; thus, accurately predicting the buckling load. Hol (1983) also investigated the influence of imperfections on cylindrical shell vibrations. He included an asymmetric as well as an axisymmetric imperfection mode in his analysis. Hol found correlation between his numerical results and those obtained through a buckling analysis. Liu and Arbocz (1985a,b;1986) published a series of reports examining the effect of imperfections on shell vibrations. They investigated the forced, nonlinear response of a shell with axisymmetric and asymmetric imperfections, observing how the presence of these imperfections affected the stability characteristics of their solutions.

Fox (1993) extended the work of Evensen on nonlinear ring vibrations to include the effects of geometric type imperfections presented by Liu and Arbocz. Fox investigated the nonlinear features associated with the inextensional theory compared with the nonlinear features associated with the imperfections. He also used higher order spectral processing techniques to verify the presence of nonlinear features in the ring response. Since his investigation led to the study reported in this thesis, a more comprehensive synopsis follows.

Fox derived ring equations similar to those of Evensen, except his equations included the Sanders' form of the strain displacement relation as well as geometric imperfections. The purpose of his study was to determine which feature, inextensionality or imperfections, dominates the nonlinear response of the ring. Both mechanisms create a second harmonic frequency, or a frequency of two times the excitation frequency in the ring response. However, for the

inextensional ring, this double frequency is present at the $n=0$ wavenumber response. For the ring with imperfections, this double frequency appears at the n th wavenumber, where n corresponds to the wavenumber associated with the resonance frequency that is closest to the excitation frequency. Therefore, by making spatial measurements of the ring and resolving the participation of individual wavenumbers, the contribution to the double frequency by each mechanism was evaluated. More clearly, the amplitude of the second harmonic frequency component at the $n=0$ wavenumber response was compared to the amplitude of this frequency component associated with the response at the n th wavenumber.

Analytically, Fox found that the quadratic nonlinear terms associated with the inextensional theory dominated over those terms resulting from the imperfections. However, this result was not demonstrated experimentally. The experimental results demonstrated that the amplitude of the double frequency component was greater at the n th wavenumber than at the $n=0$ wavenumber. Because of this finding, Fox questioned the validity of the inextensional assumption for his theoretical analysis.

In this thesis, the inextensional assumption, as it applies to ring vibrations, is abandoned in favor of the more general extensional case. This leads to a different set of equations describing ring vibrations than those used by Fox. The imperfections are retained in this analysis. However, now the interest is in how the imperfections and geometric nonlinearities influence the response of circular rings in the wavenumber domain. For the analytical and numerical analysis, employing a modal series solution of weighted residuals approach, the response includes contributions from a truncated series of modes. This series is used as opposed to only a given flexural response mode, or selected combination of modes, and the breathing mode ($n=0$). Finally, the higher order spectral signature of individual wavenumber responses is investigated so that the effect of nonlinearities and imperfections on this quantity can be discerned.

1.3 Overview

This research study consists of three parts: an analytical study, a numerical simulation, and an experimental investigation. The purpose of the analytical study is to develop an accurate model of circular ring vibrations, which include the effect of nonlinearities and geometric imperfections. This model is based upon an accurate set of shell equations known as the Donnell or shallow shell equations. The nonlinearity is geometric in nature and is introduced through the strain displacement relation. The effects of geometric imperfections are also introduced through the strain displacement relation.

The numerical simulation portion of the study involves solving the equations derived in the analytical study by an approximate numerical technique. This procedure provides for an approximate quantitative indication of the effect of nonlinearities and imperfections on the ring response. Solutions are obtained for the equations representing rings with and without imperfections.

The experimental effort is conducted to verify the findings of the analytical and numerical studies. By exciting the rings at certain spatial locations, the effect of imperfections is emphasized or de-emphasized. Thus, the effective contribution of imperfections to the ring response is determined experimentally. Also, by spatially sampling the vibrating rings and wavenumber filtering the data, the response of individual wavenumbers is resolved. Therefore, the effect of imperfections and nonlinearities on individual wavenumbers participating in the response is determined.

Higher order spectral processing is also used in the numerical and experimental study to ascertain the significance of nonlinearities and imperfections. Higher order spectral processing is useful in the detection of the nonlinear content of a signal. By applying these techniques to the ring response

data, the nonlinear features of the response are not only detected, but quantified as well. Analyzing higher order spectral signatures of individual wavenumber responses provides additional insight into the energy distribution in the frequency domain and the wavenumber or spatial domain. This distribution is modified by the presence of nonlinear features and imperfections.

The remainder of this thesis is structured in a similar manner to the organization of the research study. Chapter 2 details the derivation of the modal equations for a ring with and without imperfections. Non-dimensional equations are also presented. An explanation of higher order spectral processing and its application in this thesis are contained in Chapter 3. A function named the bicoherence, or bispectrum, is defined, and its application to the detection of quadratic features in a signal is designated. In Chapter 4 the numerical simulation is summarized. Chapter 5 describes the experimental setup used to excite the rings and measure their response. Also included in Chapter 5 are the results of the experimental investigation. The power spectral as well as higher order spectral contents of individual wavenumbers participating in the ring response are presented. The conclusions drawn in this study are specified in Chapter 6.

CHAPTER 2: DERIVATION OF RING EQUATIONS

Presented in this chapter is the analytical study performed to provide insight into nonlinear, circular ring vibrations and to discern the effects of imperfections on these vibrations. The nonlinear equations describing the transverse vibrations of circular rings are derived, first without imperfections and then including geometric type imperfections. Galerkin's procedure is used to derive a set of coupled, modal equations from the set of partial differential equations describing ring vibrations. Discussion concerning the quadratic features and energy transfer due to coupling of modal equations is included. Both sets of equations are non-dimensionalized as well. Comparisons of these equations and their salient features completes the chapter.

2.1 Derivation of Equations without Imperfections

Several different sets of transverse ring vibration equations result from different derivation methods as well as from different initial assumptions, related to the strain displacement relations or force equilibrium equations. The approach used here most closely resembles that of Evensen (1964). The shallow shell equations of Von Karman and Margeare presented by Chu (1961) are modified such that they are applicable to ring vibrations. The strain displacement relation used by Evensen (1964) and derived by Novozhilov (1953) is adopted. First, the ring equations are derived without the presence of imperfections. Then, these equations are derived including imperfections. The shallow shell equations for a shell including imperfections are presented by Liu and Arbocz (1986). They also introduce a strain displacement relation, which models geometric type imperfections. Fox (1993) derives this relation, and a version of his expression is used in this derivation.

The approach for deriving the dynamic ring equations involves substitution of force and moment resultants into the shallow shell equations reduced to a ring geometry. The shallow shell equations are derived by Chu and depend upon the following expression for the circumferential strain displacement relation:

$$\epsilon_y = \frac{\partial v}{\partial y} + \frac{w}{R} - z \frac{\partial^2 w}{\partial y^2} + \frac{1}{2} \left(\frac{\partial w}{\partial y} \right)^2 . \quad (2.1)$$

In Eq. 2.1, w is the radial displacement, v the circumferential displacement, y the circumferential coordinate, R the radius of the ring, and z the radial coordinate. Figures 2.1 and 2.2 depict these quantities on a ring element and full ring. Equation 2.1 includes a second-order, nonlinear term. This term is quadratic in the rotations of the ring cross sections.

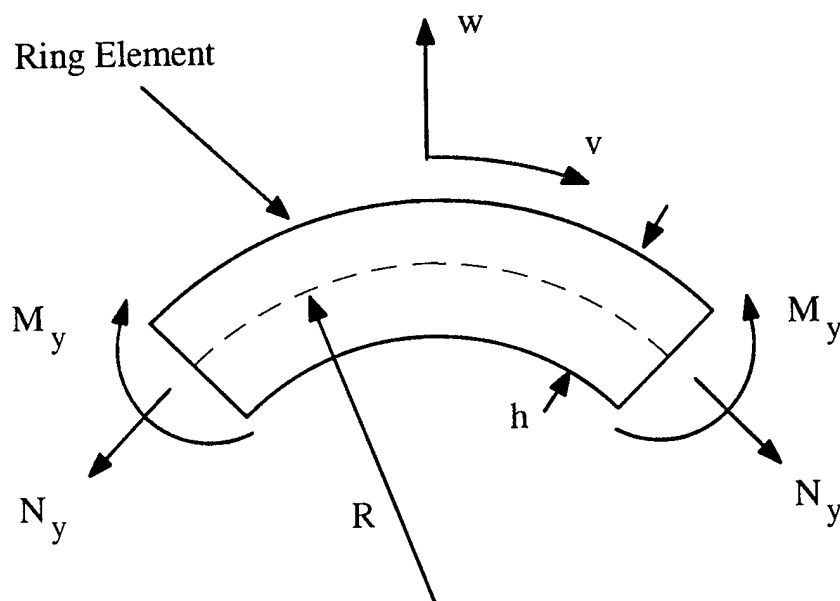


Figure 2.1: Ring Element

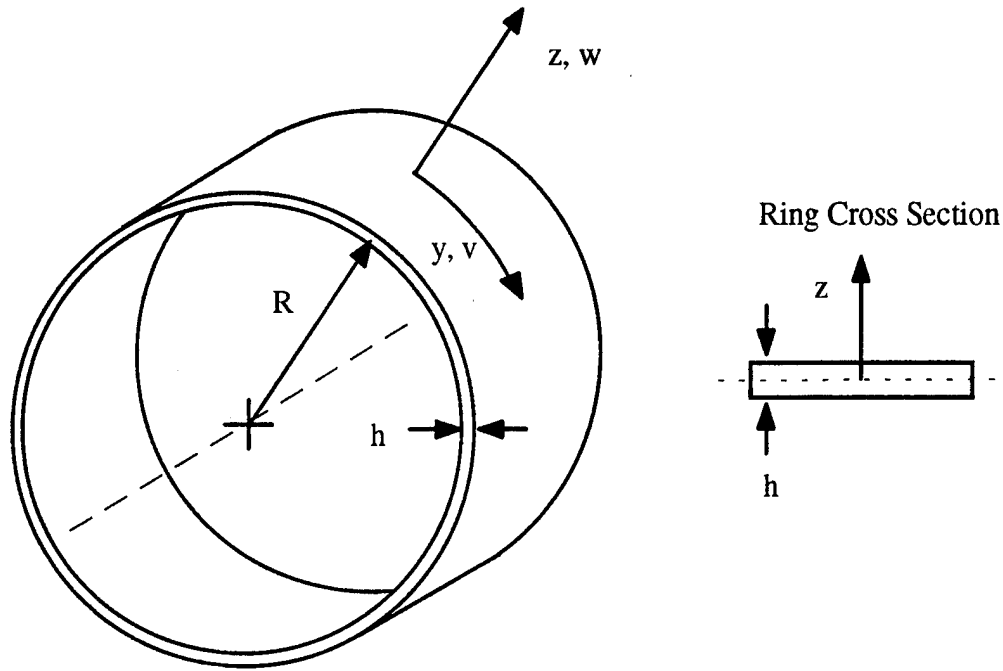


Figure 2.2: Ring Geometry

ARL:UT
AS-95-355
PT - rfg
9-95

When the shallow shell equations of Chu are reduced to the ring, the following equations result:

$$\frac{\partial^2 M_y}{\partial y^2} + \frac{\partial}{\partial y} \left(N_y \frac{\partial w}{\partial y} \right) - \frac{N_y}{R} - \rho h \ddot{w} = -q(y,t) \quad (2.2a)$$

$$\frac{\partial N_y}{\partial y} = \rho h \ddot{v} \quad , \quad (2.2b)$$

where N_y represents the circumferential force resultant and M_y the moment resultant acting on a cross section of the ring, ρ is density, t is time, and the overstrike dots denote differentiation with respect to time. Figure 2.1 displays a differential element of the ring with these forces and moments applied to it. A radially applied forcing function is denoted in Eq. 2.2a by $q(y,t)$.

The following assumptions are inherent in Eqs. 2.2 (Chu, 1961):

- ring thickness is small compared to the radius
- displacements are predominantly flexural
- circumferential wavelengths are large compared to the ring thickness.

Evensen (1964) states an additional assumption inherent in the shallow shell equations. This assumption requires that $\frac{1}{n^2} \ll 1$, which means these equations should be used only when $n > 4$ to 6, depending on the required accuracy. However, in spite of this restriction, Evensen used these equations because of their simplicity. These equations will be used here for similar reasons but also so that comparisons can be made between the results found here and results established previously. Additionally, inclusion of the Morley correction (1959) improves the accuracy of the linear terms while retaining the same nonlinear terms. This correction term is introduced later in the derivation.

The following assumptions, used to reduce the shallow shell equations of Chu to ring equations, are reflected in Eqs. 2.2:

- w and v are taken to be functions of only the circumferential coordinate, y , and time, t (i. e., no axial variation of displacements is allowed).
- The thickness, h , and width, b , of the ring are constant.
- The force resultants, N_x , representing the axial force, and N_{xy} , representing the in-plane shear force, are assumed to be zero throughout the ring.

Equation 2.1 is used to derive expressions for the force and moment resultants in Eqs. 2.2. These resultants are found by integrating the hoop stress across the cross section of the ring. By assuming a Hooke's law relationship between stress and strain, the hoop stress is determined. Therefore,

$$\sigma_y = E\epsilon_y \quad (2.3)$$

and

$$N_y = \int_{-h/2}^{h/2} \sigma_y dz \quad (2.4)$$

$$M_y = \int_{-h/2}^{h/2} \sigma_y z dz \quad , \quad (2.5)$$

where E is Young's Modulus. Making the appropriate substitutions and calculating the integrals, the force and moment are

$$N_y = Eh \left[\frac{\partial v}{\partial y} + \frac{w}{R} + \frac{1}{2} \left(\frac{\partial w}{\partial y} \right)^2 \right] \quad (2.6)$$

$$M_y = -\frac{Eh^3}{12} \frac{\partial^2 w}{\partial y^2} \quad . \quad (2.7)$$

These equations are substituted into the shallow shell equations such that a set of partial differential equations describing the ring motion results. Before these results are presented, a point regarding tangential inertia, \ddot{v} , is made. As stated by Evensen (1964) and also by Fox (1993), neglecting tangential inertia for this class of ring vibrations is a reasonable assumption. Evensen includes the effects of tangential inertia and examines the resulting new terms to determine under what conditions they are significant. His analysis reveals that tangential inertia can be neglected if

$$\omega^2 \ll \frac{E}{\rho R^2} n^2 \quad , \quad (2.8)$$

where ω is the frequency of excitation and $\frac{E}{\rho R^2}$ is the natural frequency of the $n=0$, breathing mode, as will be shown later. Therefore, Eq. 2.8 can be rewritten

$$\omega \ll n\omega_0 \quad . \quad (2.9)$$

For the frequencies of excitation and modes investigated in this study, this requirement is certainly satisfied.

The application of this assumption to Eq. 2.2b results in the following expression:

$$\frac{\partial N_y}{\partial y} = \rho h \ddot{v} = 0 \quad . \quad (2.10)$$

Finally, the partial differential equations representing transverse vibrations of rings are

$$-\frac{Eh^3}{12} \frac{\partial^4 w}{\partial y^4} + Eh \left[\frac{\partial v}{\partial y} + \frac{w}{R} + \frac{1}{2} \left(\frac{\partial w}{\partial y} \right)^2 \right] \frac{\partial^2 w}{\partial y^2} \quad (2.11a)$$

$$-\frac{Eh}{R} \left[\frac{\partial v}{\partial y} + \frac{w}{R} + \frac{1}{2} \left(\frac{\partial w}{\partial y} \right)^2 \right] - \rho h \ddot{w} = -q(y,t)$$

$$\frac{\partial N_y}{\partial y} = 0 \quad . \quad (2.11b)$$

Up to this point, the derivation follows that of Evensen (1964). However, now, when Galerkin's method is applied, the technique differs slightly, in that a different form of the assumed displacement function is used. In this derivation, a truncated series of radial modes is used as an assumed displacement function, as opposed to a single mode plus the breathing mode. Additionally, Evensen (1964) and Fox (1993) present a similar derivation for inextensional vibrations but not for extensional.

Galerkin's method is used to transform the partial differential equations, Eqs. 2.11, to ordinary differential equations with the dependent variable being time, t . This procedure minimizes the error associated with the solution in a least squares manner. The resulting equations represent nonlinear modal equations for the ring.

The first step in the application of Galerkin's method is selection of an assumed function for the radial displacement, w . The assumed displacement function contains a spatial and a time dependent component. A cosine expansion of the following form is selected:

$$w = \sum_{n=0}^N A_n \cos\left(\frac{ny}{R}\right) \quad . \quad (2.12)$$

In this expression, A_n is a dynamic amplitude function, or $A_n = A_n(t)$. A companion set, $B_n \sin\left(\frac{ny}{R}\right)$, could also be included in the assumed displacement form. However, Evensen (1964) showed that these companion modes are excited only if the excitation frequency is within a very narrow region about a natural frequency of the ring. In the present study, this companion mode instability is not investigated. If the reader is interested in a solution which includes the companion mode terms, see Evensen (1964).

The most general form of an expression for w would not only possess the companion set of modes, but also an upper bound of the summation at $n=\infty$. However, since the higher order modes require an extensive amount of energy to excite, they contribute minimally to total response; thus, the series is truncated at N . This is especially true for low frequencies of excitation. This truncation also allows for tractable solutions to the resulting equations to exist.

Now that an expression for w is assumed, an expression for $\frac{\partial v}{\partial y}$ must be solved for, since this term is a remaining unknown in Eq. 2.11a. Since the derivative of N_y with respect to y must be equal to zero due to neglecting tangential inertia, N_y must be a function of time only, or

$$\frac{\partial N_y}{\partial y} = 0 \quad \therefore N_y = f(t) = Eh \left[\frac{\partial v}{\partial y} + \frac{w}{R} + \frac{1}{2} \left(\frac{\partial w}{\partial y} \right)^2 \right]. \quad (2.13)$$

This equation is used to solve for $\frac{\partial v}{\partial y}$ and eliminates the final remaining unknown. Solving for $\frac{\partial v}{\partial y}$ yields

$$\frac{\partial v}{\partial y} = \frac{f(t)}{Eh} - \frac{1}{R} \sum_{n=0}^N A_n \cos\left(\frac{ny}{R}\right) - \frac{1}{2} \left(\frac{1}{R} \sum_{n=0}^N -n A_n \sin\left(\frac{ny}{R}\right) \right)^2, \quad (2.14)$$

which when expanded gives

$$\frac{\partial v}{\partial y} = \frac{f(t)}{Eh} - \frac{1}{R} \sum_{n=0}^N A_n \cos\left(\frac{ny}{R}\right) \quad (2.15)$$

$$- \frac{1}{4R^2} \sum_{m=0}^N \sum_{n=0}^N mn A_m A_n \left[\cos(m-n) \frac{y}{R} - \cos(m+n) \frac{y}{R} \right] .$$

The continuity condition is now used to solve Eq. 2.15 for $f(t)$. The continuity condition requires periodicity of $2\pi R$ with respect to displacements about the circumference of the ring. This restraint is imposed due to closure of the ring. The continuity condition can be stated mathematically as

$$v(y + 2\pi R, t) - v(y, t) = \int_y^{y+2\pi R} \frac{\partial v}{\partial y} dy = 0 \quad (2.16)$$

Equation 2.16 requires that $\frac{\partial v}{\partial y}$ contain only periodic terms in y . Therefore, the first term in Eq 2.15 must cancel with all the non-periodic terms, or terms which are functions of time only, in the remainder of the expression. The following equation results:

$$f(t) = N_y = \frac{Eh}{R} \left[A_0 + \frac{1}{4R} \sum_{n=0}^N n^2 A_n^2 \right] \quad (2.17)$$

The solution for N_y and the assumed displacement form, Eq. 2.12, are now substituted into the shallow shell equations, Eq. 2.11, so that Galerkin's procedure can be applied. These substitutions yield

$$\begin{aligned}
& -\frac{Eh^3}{12R^4} \sum_{n=0}^N n^4 A_n \cos\left(\frac{ny}{R}\right) \\
& + \frac{Eh}{R} \left[A_0 + \frac{1}{4R} \sum_{n=0}^N n^2 A_n^2 \right] \times \left[\frac{1}{R^2} \sum_{n=0}^N -n^2 A_n \cos\left(\frac{ny}{R}\right) \right] \\
& - \frac{Eh}{R^2} \left[A_0 + \frac{1}{4R} \sum_{n=0}^N n^2 A_n^2 \right] - \rho h \sum_{n=0}^N \ddot{A}_n \cos\left(\frac{ny}{R}\right) - q(y,t) = R(w) \quad , \quad (2.18)
\end{aligned}$$

where $R(w)$ is the differential equation residual.

The application of Galerkin's method is represented mathematically as

$$\int_0^{2\pi R} R(w) \cos\left(\frac{ny}{R}\right) dy = 0 \quad n = 0, 1, 2, \dots, N \quad . \quad (2.19)$$

According to the Galerkin method, the residual of Eq. 2.18 is multiplied by the approximating functions, $\cos\left(\frac{ny}{R}\right)$, and integrated with respect to y from 0 to $2\pi R$, or about the full circumference of the ring.

The orthogonality condition of the cosine approximating functions is used to produce the following equations:

$$n \geq 1; -\frac{Eh^3}{12R^4}n^4A_n(\pi R) - \frac{Eh}{R^3}\left[A_0 + \frac{1}{4R}\sum_{m=0}^N m^2A_m^2\right](n^2A_n\pi R)$$

$$-\rho h\ddot{A}_n(\pi R) = -F_n(t) \quad (2.20a)$$

$$n = 0; -\frac{Eh}{R^2}A_0(2\pi R) - \frac{Eh}{4R^3}\sum_{m=0}^N m^2A_m^2(2\pi R)$$

$$-\rho h\ddot{A}_0(2\pi R) = -F_0(t) \quad , \quad (2.20b)$$

where

$$F_n(t) = \int_0^{2\pi R} q(y,t) \cos\left(\frac{ny}{R}\right) dy \quad (2.20c)$$

$$F_0(t) = \int_0^{2\pi R} q(y,t) dy \quad . \quad (2.20d)$$

Equations 2.20a and 2.20b can be simplified to yield

$$n \geq 1; \ddot{A}_n + \frac{Eh^2n^4}{12\rho R^4}A_n + \frac{En^2}{\rho R^3}A_n\left[A_0 + \frac{1}{4R}\sum_{m=0}^N m^2A_m^2\right] \quad (2.21a)$$

$$= -\frac{F_n(t)}{\pi R \rho h}$$

$$n = 0; \ddot{A}_0 + \frac{E}{\rho R^2}A_0 - \frac{E}{4\rho R^3}\sum_{m=0}^N m^2A_m^2 = -\frac{F_0(t)}{2\pi R \rho h} \quad . \quad (2.21b)$$

A set of nonlinear modal equations describing the radial vibrations of circular rings is thus derived. As stated earlier, the linear form of these equations is improved by the addition of a term known as the Morley correction factor (Morley, 1959). The Morley correction results in the addition of two linear terms to the ring equations, improving the linear features of these equations while leaving the nonlinear terms untouched. Addition of this term results in the following expression for the natural frequency of the n th mode:

$$\omega_n^2 = \frac{Eh^2(n^2 - 1)^2}{12\rho R^4} \quad (2.22)$$

The new equations representing the response of the $n \geq 1$ modes or wavenumbers and $n=0$ mode or wavenumber are now

$$\begin{aligned} n \geq 1; \quad \ddot{A}_n + \frac{Eh^2(n^2 - 1)^2}{12\rho R^4} A_n + \frac{En^2}{\rho R^3} A_n \left[A_0 + \frac{1}{4R} \sum_{m=0}^N m^2 A_m^2 \right] \\ = -\frac{F_n(t)}{\pi R \rho h} \end{aligned} \quad (2.23a)$$

$$n = 0; \quad \ddot{A}_0 + \frac{E}{\rho R^2} A_0 - \frac{E}{4\rho R^3} \sum_{m=0}^N m^2 A_m^2 = -\frac{F_0(t)}{2\pi R \rho h} \quad (2.23b)$$

The expression for the breathing mode response remains the same after the Morley correction is implemented. However, it is listed again above for completeness.

Observation of these coupled equations describing the ring vibrations, Eqs. 2.23, reveals several interesting features concerning the transfer of energy in

the wavenumber and frequency domains. Most notably, the mechanism for quadratic transfer of energy between the n th mode or wavenumber and breathing mode ($n=0$ wavenumber) is now visible. The term $-\frac{E}{4\rho R^3} \sum_{m=0}^N m^2 A_m^2$ in Eq. 2.23b, for example, couples all wavenumbers participating in the motion to the $n=0$ wavenumber, breathing mode response. Therefore, a quadratic mechanism exists which transfers energy from a higher order n th wavenumber response to the $n=0$ wavenumber response. The frequency components present in the response of the n th wavenumber appear at twice their value in the $n=0$ wavenumber response. More clearly, a frequency component, f_n , appearing in the response of the n th mode, is present in the breathing mode response as $2f_n$. It should also be noted that the phase associated with this frequency component, ϕ_n , is present in the breathing mode response as $2\phi_n$.

Depending on the form of the excitation, $q(y,t)$, wavenumbers will or will not be excited in a linear fashion. For this study, the spatial component of the excitation is represented by the Dirac delta function. Thus,

$$q(y,t) = f(t)\delta_D(y). \quad (2.24)$$

This form of excitation approximates a spatially localized type of excitation, possessing a wide spectrum of wavenumbers.

With the excitation represented by Eq. 2.24, all wavenumbers are theoretically excited and participate in the response. However, the amplitude of a given wavenumber in the response depends on the proximity of frequency components in the excitation to the natural frequencies of the respective modes. Nonetheless, a linear response of the $n=0$ wavenumber is expected, even though its amplitude may be small relative to those of other wavenumbers responding.

Now, Eq. 2.23 is non-dimensionalized, so that order of magnitude comparisons can be made between terms. The following parameters are necessary to non-dimensionalize the equations of motion:

$$a_n = \frac{A_n}{h} \quad \tau = \omega_0 t \quad \varepsilon = \frac{h}{R} \quad . \quad (2.25a-c)$$

Substituting these parameters into Eq. 2.23 and making some simplifications, the following expressions result:

$$a_{n\tau\tau} + \frac{(n^2 - 1)^2 \varepsilon^2}{12} a_n + n^2 \varepsilon a_n a_0 + \frac{n^2 \varepsilon^2 a_n}{4} \sum_{m=1}^N (ma_m)^2 = \frac{F_n(\tau)}{b\pi R \rho h^2 \omega_0^2} \quad ; \quad (2.26a)$$

$$a_{0\tau\tau} + 2\zeta_n a_{0\tau} + a_0 + \frac{\varepsilon}{4} \sum_{m=1}^N (ma_m)^2 = \frac{F_0(\tau)}{2b\pi R \rho h^2 \omega_0^2} \quad . \quad (2.26b)$$

These non-dimensional equations will be used later to compare the order of magnitude of the terms present here to the additional terms created by imperfections.

In summary, Eqs. 2.23a and 2.23b, representing the nonlinear transverse vibrations of circular rings, have been derived. These equations are also presented in a non-dimensional form to allow for comparison between important terms. Some of the features associated with the transfer of energy in the wavenumber

and frequency domain have been cited and discussed. A new set of equations will be derived in the next section that include the effects of geometric imperfections.

2.2 Derivation of Equations Including Imperfections

This derivation follows the same guidelines as that of the equations without imperfections. Some of the methods are presented more briefly since they are concurrent with those discussed in the previous section.

Identical to the derivation of the perfect ring equations, the first step is selection of a circumferential strain displacement relation. This relation will now include the effects of imperfections. Before the strain displacement relation is presented, an explanation and comments regarding the nature of the imperfections are necessary. The imperfections represent an initial, static deformation of the ring. The quantity, $\bar{w}(y)$, represents this static deformation as a function of the circumferential location. This is shown more clearly in Fig. 2.3. From this figure, it can be seen that $\bar{w}(y)$ represents the deviation of the ring surface, in its static state, from a perfect ring of radius R . For this study, it is assumed that the static state of the ring is stress free.

A strain displacement relation, including the presence of imperfections, is derived by Fox (1993). This relation is also presented by Liu and Arbocz (1986). A form resembling that used by Fox and identical to the circumferential strain expression presented by Liu and Arbocz in their shell study is used here. Fox includes terms related to the Sanders derivation which are neglected in this derivation. Also, the form used in this derivation is not simplified to the middle surface strain displacement relation, as the form used by Liu and Arbocz. Therefore, the z term is present since $z \neq 0$.

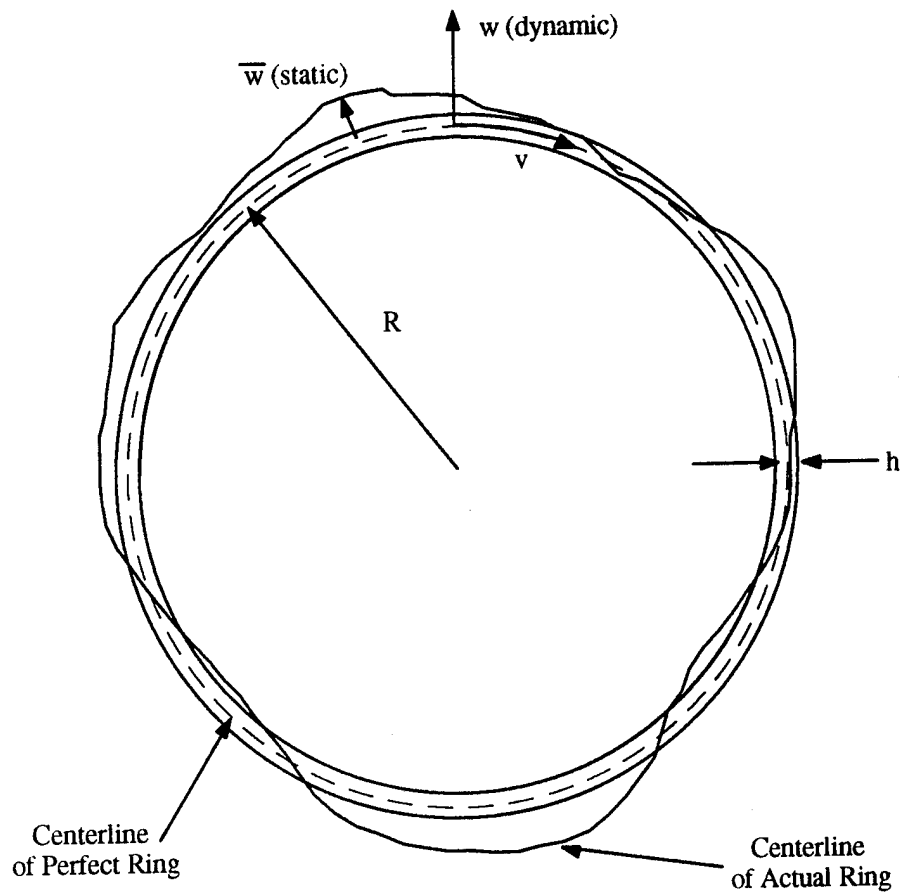


Figure 2.3: Ring with Imperfections

ARL:UT
AS-95-356
PT - rfg
9-95

The strain displacement relation including imperfections is

$$\epsilon_y = \frac{\partial v}{\partial y} + \frac{w}{R} - z \frac{\partial^2 w}{\partial y^2} + \frac{1}{2} \left(\frac{\partial w}{\partial y} \right)^2 + \frac{\partial w}{\partial y} \frac{\partial \bar{w}}{\partial y} \quad (2.27)$$

A form of the shallow shell equations including imperfections is also presented by Liu and Arbocz (1986). Reducing these Liu and Arbocz shell equations to ring

equations by applying the assumptions introduced in Sec. 2.1, the following expression results:

$$\frac{\partial^2 M_y}{\partial y^2} + N_y \left(\frac{\partial^2 w}{\partial y^2} + \frac{\partial^2 \bar{w}}{\partial y^2} \right) - \frac{N_y}{R} - \rho h \ddot{w} = -q(y,t) \quad . \quad (2.28)$$

The second ring equation, Eq. 2.2b, remains unchanged when imperfections are included. Equation 2.2a has one additional term due to the presence of imperfections. This term, $N_y \frac{\partial^2 \bar{w}}{\partial y^2}$, actually appears to be a nonlinear term, but in essence it contributes additional linear terms, as well as nonlinear terms. \bar{w} , and thus $\frac{\partial \bar{w}}{\partial y}$, is a static quantity. As shown in Sec. 2.1, N_y must be a function of time only due to neglect of tangential inertia. Therefore, the static, imperfection term multiplying the linear components of the time varying force resultant produces additional linear terms. Additional nonlinear terms arise due to the presence of nonlinear terms in the expression for N_y .

Proceeding in the same manner as the derivation for the perfect ring, neglect of tangential inertia forms the following expression for the force resultant,

$$N_y = f(t) = Eh \left[\frac{\partial v}{\partial y} + \frac{w}{R} + \frac{1}{2} \left(\frac{\partial w}{\partial y} \right)^2 + \frac{\partial w}{\partial y} \frac{\partial \bar{w}}{\partial y} \right] \quad . \quad (2.29)$$

Galerkin's method is again used; thus, an assumed radial displacement must be selected. However, due to presence of imperfections, an assumed form must be selected for \bar{w} also. Equation 2.12 is used in this derivation to express the radial displacement. A similar form is chosen to represent the imperfections, as well. The imperfections are expressed as

$$\bar{w} = \sum_{n=2}^N \delta_n \cos\left(\frac{ny}{R} + \phi_n\right) \quad . \quad (2.30)$$

In this equation, δ_n is the amplitude of the n th imperfection waveform component, while ϕ_n is the spatial phase of this component with respect to an arbitrary fixed location. This expression is a Fourier type expansion of the general imperfection shape of the ring. The summation commences at $n=2$ because the $n=0$, breathing mode, and the $n=1$, rigid body mode, do not represent flexural deformation and are thus excluded.

Solving for $\frac{\partial v}{\partial y}$,

$$\begin{aligned} \frac{\partial v}{\partial y} = & \frac{f(t)}{Eh} - \frac{1}{R} \sum_{n=0}^N A_n \cos\left(\frac{ny}{R}\right) - \frac{1}{2} \left(\frac{1}{R} \sum_{n=0}^N -nA_n \sin\left(\frac{ny}{R}\right) \right)^2 \\ & - \frac{1}{R^2} \left(\sum_{n=0}^N -nA_n \sin\left(\frac{ny}{R}\right) \right) \left(\sum_{m=2}^N -m\delta_m \sin\left(\frac{my}{R} + \phi_m\right) \right) \quad . \quad (2.31) \end{aligned}$$

The expression for $\frac{\partial v}{\partial y}$ may contain terms which are a function of time only due to the continuity condition. Therefore, the following equation is formed:

$$f(t) = N_y = \frac{Eh}{R} \left[A_0 + \frac{1}{4R} \left(\sum_{n=0}^N n^2 A_n^2 + \sum_{m=2}^N m^2 A_m \delta_m \cos \phi_m \right) \right] \quad . \quad (2.32)$$

Now this expression, along with the assumed form of the radial displacement, Eq. 2.12, and the expression representing the imperfections, Eq. 2.30, are substituted into the shallow shell equation, Eq. 2.28, to yield

$$\begin{aligned}
 & -\frac{Eh^3}{12R^4} \sum_{n=0}^N n^4 A_n \cos\left(\frac{ny}{R}\right) + \frac{Eh}{R} \left[A_0 + \frac{1}{4R} \left(\sum_{n=0}^N n^2 A_n^2 + \sum_{m=2}^N m^2 A_m \delta_m \cos \phi_m \right) \right] \\
 & \times \left[\frac{1}{R^2} \left(\sum_{n=0}^N -n^2 A_n \cos\left(\frac{ny}{R}\right) + \sum_{m=2}^N -m^2 \delta_m \cos\left(\frac{my}{R} + \phi_m\right) \right) \right] \\
 & - \frac{Eh}{R^2} \left[A_0 + \frac{1}{4R} \left(\sum_{n=0}^N n^2 A_n^2 + \sum_{m=2}^N m^2 A_m \delta_m \cos \phi_m \right) \right] \\
 & - \rho h \sum_{n=0}^N \ddot{A}_n \cos\left(\frac{ny}{R}\right) + q(y,t) = R(w) \quad . \quad (2.33)
 \end{aligned}$$

The derivation of the equations of motion for a ring with imperfections now proceeds with the application of Galerkin's method. The procedure is conducted in the same manner as before. Equation 2.33 is multiplied by the approximating functions, $\left(\frac{ny}{R}\right)$, and the product is integrated with respect to y , about the circumference of the ring. Again, the Morley correction term is added, modifying the natural frequency expression. The following approximate equations of motion for the ring with imperfections result:

$$n \geq 1; \ddot{A}_n + \frac{Eh^2(n^2 - 1)^2}{12\rho R^4} A_n + \frac{En^2}{\rho R^3} A_n \left[A_0 + \frac{1}{4R} \left(\sum_{m=0}^N m^2 A_m^2 + \sum_{m=2}^N m^2 \delta_m A_m \cos \phi_m \right) \right] \quad (2.34a)$$

$$+ \frac{En^2}{\rho R^3} \left[\delta_n A_0 \cos \phi_n + \frac{\delta_n \cos \phi_n}{4R} \left(\sum_{m=1}^N m^2 A_m^2 + \sum_{m=2}^N m^2 \delta_m A_m \cos \phi_m \right) \right]$$

$$= -\frac{F_n(t)}{\pi R \rho h}$$

$$n = 0; \ddot{A}_0 + \frac{E}{\rho R^2} A_0 - \frac{1}{4R} \left(\sum_{m=0}^N m^2 A_m^2 + \sum_{m=1}^N m^2 A_m \delta_m \cos \phi_m \right)$$

$$= -\frac{F_0(t)}{2\pi R \rho h} \quad (2.34b)$$

Equations 2.34 contain all of the terms found in the equations for the vibrations of a perfect ring. The presence of imperfections results in terms being added to those original equations. These additional terms are linear and quadratic. Each of these additional terms includes an imperfection amplitude and phase component. The discussion here addresses the effect of these terms on the linear and quadratic response features of the ring.

The additional terms now present due to imperfections also provide for the transfer of energy from higher order wavenumbers to lower order wavenumbers. However, now linear coupling terms are also present, whereas the perfect ring equations contained only quadratic coupling terms. An example of this linear coupling is the term $\sum_{m=1}^N m^2 A_m \delta_m \cos \phi_m$ present in Eq. 2.34b. All wavenumbers which contain a non-zero imperfection amplitude are coupled to the $n=0$ wavenumber response, with the strength of this coupling depending on the size and phase of the imperfection components. To illustrate, a wavenumber, m , with an imperfection present, responding at a frequency, f_m , will also create a response at the breathing mode ($m=0$) at this frequency, f_m .

Additional quadratic coupling terms due to the imperfections arise, as well. An example of these terms can be found in Eq. 2.34a, namely the term $\frac{En^2}{\rho R^3} A_n \sum_{m=2}^N m^2 \delta_m A_m \cos \phi_m$. The n th wavenumber is quadratically coupled to the m th wavenumber, where the m th wavenumber represents a wavenumber with an imperfection component present. This coupling manifests itself in the production of excitation frequency harmonics in the response of the n th wavenumber. This assumes that both the m th and n th wavenumbers are responding and that the m th wavenumber contains an imperfection component not orthogonal to the excitation, i.e., $\phi_m \neq \pm 90^\circ$. Thus, quadratic as well as linear energy transfer take place in the wavenumber domain due to the presence of these imperfections.

Now, as with the perfect ring equations, Eqs. 2.34 are non-dimensionalized so that comparisons can be made between terms. The following non-dimensional quantities are necessary:

$$\omega_0 = \frac{1}{R} \sqrt{\frac{E}{\rho}} \quad a_0 = \frac{A_0}{h} \quad a_n = \frac{A_n}{h} \quad (2.35a-c)$$

$$\bar{\delta}_n = \frac{\delta_n}{h} \quad \tau = \omega_0 t \quad . \quad (2.35d-e)$$

Substituting these expressions into Eqs. 2.34 and simplifying,

$$a_{n\tau\tau} + \frac{\epsilon}{12}(n^2 - 1)^2 a_n + \epsilon n^2 \left[a_n a_0 + \bar{\delta}_n a_0 \cos \phi_n \right] \\ + \left(\frac{\epsilon n}{2} \right)^2 a_n \left[\sum_{m=1}^N m^2 a_m^2 + \sum_{m=2}^N m^2 \bar{\delta}_m a_m \cos \phi_m \right] \quad (2.36a)$$

$$+ \left(\frac{\epsilon n}{2} \right)^2 \bar{\delta}_n \cos \phi_n \left[\sum_{m=1}^N m^2 a_m^2 + \sum_{m=2}^N m^2 \bar{\delta}_m a_m \cos \phi_m \right] = \frac{F_n(t)}{\pi R \rho h^2 \omega_0^2}$$

$$a_{0\tau\tau} + a_0 + \frac{\epsilon}{4} \sum_{m=1}^N m^2 a_m^2 + \frac{\epsilon}{4} \sum_{m=2}^N m^2 a_m \bar{\delta}_m \cos \phi_m = \frac{F_0(t)}{2\pi R \rho h^2 \omega_0^2} \quad . \quad (2.36b)$$

To summarize, the nonlinear ring equations predict the presence of frequencies twice that of the excitation frequency, i. e., a second harmonic frequency, in the ring response. This double frequency is present at the n th wavenumber in the response as well as in the breathing mode, where n represents a wavenumber excited by the excitation source. Therefore, nonlinear transfer of energy takes place in the wavenumber domain due to the coupling of the response of the $n=0$ wavenumber to that of the n th wavenumber.

When effects of imperfections are added to the equations, additional linear as well as nonlinear coupling terms result. Therefore, the aforementioned energy transfer from the n th mode to the breathing mode exists, but additional features are present as well. Linear coupling now exists between the $n=0$ wavenumber and

the n th wavenumber response, provided that the n th wavenumber possesses an imperfection component properly aligned with the excitation. This results in linear energy transfer to the breathing mode. Therefore, additional energy is now present at the $n=0$ wavenumber response at the excitation frequency, resulting in an increased response of this wavenumber at this frequency. A similar effect is experienced by other wavenumbers with imperfections present, allowing for the linear transfer of energy between higher order and lower order wavenumber responses.

The addition of imperfections also results in the strengthening of the nonlinear features of the ring. Observation and comparison of the non-dimensionalized equations, Eqs. 2.26 and Eqs. 2.36, reveal that depending on the size of the imperfections, the quadratic nature of these equations can increase significantly due to their presence. For example, in Eq. 2.26, the term $n^2 \epsilon_n a_0$ represents some of the quadratic features. In Eq. 2.36, additional quadratic terms are present due to imperfections, such as $\frac{n^2 \epsilon_n^2}{4} \bar{\delta}_n \cos \phi_n \sum_{m=1}^N (m a_m)^2$, which do not depend on the amplitude of the breathing mode response. Thus, with imperfections present, the quadratic signatures in the ring response are more likely to be observed at low excitation force levels, due to strengthening of these features.

This concludes the presentation of the introductory information as well as the analytical development and discussion of the nonlinear ring vibrations. The next chapter addresses the use of higher order spectral processing (HOSP) to detect and quantify the nonlinear features of the ring response. Background information concerning HOSP is presented as well as an explanation for using it in this application.

CHAPTER 3: INTRODUCTION TO HIGHER ORDER SPECTRAL PROCESSING

The purpose of this chapter is to introduce the reader to higher order spectral processing (HOSP) and its application in this thesis. Higher order spectral processing has recently enjoyed widespread use in a number of research areas. The introduction presented here is meant to explain the use of HOSP for this particular application. More extensive summaries can be found in the following references: O'Donnell (1990), Lamb (1993), Wolinsky (1988), and Wilson (1990).

HOSP techniques have enjoyed a variety of applications in numerous fields. These techniques have proved successful in the identification of nonlinear and parametric mechanisms in structural vibrations research. Stearman and Lamb (1992) used HOSP functions to investigate the parametric and nonlinear aeroelastic response of damaged aircraft wings, wings with stores and wings with winglets attached. Analytical modeling of these features was verified by the higher order spectral features observed when data from wind tunnel tests was processed. Lamb (1993) used the tricoherence, a normalized HOSP function, to detect small amplitude, parametric interaction features in periodic beams. The tricoherence successfully identified the spectral coherence present between a carrier and sum and difference frequencies produced by a parametric process, even though these spectral components were small in amplitude. O'Donnell (1990) investigated the higher order spectral signature created by the application of active controls to cylindrical shell vibrations. O'Donnell found that even though linear features of shell vibrations were suppressed due to active control, higher order spectral signatures were enhanced.

3.1 Definition of the Discrete Fourier Transform

Some preliminary definitions are necessary before HOSP functions can be introduced. The discrete Fourier transform is defined as follows:

$$X_j = \frac{1}{N} \sum_{n=0}^{N-1} x_n e^{-i2\pi jn/N} \quad , \quad (3.1)$$

where x is the digitized time series and N the number of digitized data points in x .

Therefore, a time signal, digitized and represented by x , is Fourier transformed using Eq. 3.1 such that the result, X , approximates the frequency and phase composition of the data. A magnitude and phase component exists for each frequency. The utilization of the phase information, or the detection of phase coherence among different frequencies, is an essential feature of HOSP.

3.2 The Power Spectrum

The most common spectral function used to analyze dynamic signals is the power spectrum. The power spectrum is used to determine the spectral or frequency content of a signal. This function is defined as

$$S(f_i) = \langle X_i \bar{X}_i \rangle \quad , \quad (3.2)$$

where the overstrike denotes complex conjugate and the brackets denote the expectation operator. Actually, the power spectrum yields the distribution of the mean square value of the signal over the frequency domain (Powers, 1990). While amplitude information is retained, the power spectrum does not retain phase information. As shown in Eq. 3.2, the power spectrum is composed of the product

of a complex quantity and its complex conjugate. Therefore, the remaining quantity represents an amplitude only, lacking a phase component.

The power spectrum is useful for determining the frequency composition of a signal. However, if the relationships between energy present at different spectral locations in a signal is sought, a different technique is necessary. HOSP is adequately suited to fulfill this role. By retaining phase information and processing it accordingly, coherence between different frequencies is detected.

3.3 The Bispectrum

The member of the family of HOSP functions used to analyze the nonlinear ring vibrations described in this thesis is known as the bispectrum. This function is useful for detecting and quantifying quadratic features of a signal. The bispectrum is approximated as follows:

$$B(f_i, f_j, f_k) = \langle X_i X_j X_k \rangle \quad . \quad (3.3)$$

This quantity is a function of three frequencies: f_i , f_j , and f_k ; thus, it is useful for determining the coherence present among three spectral locations, or "waves." If all three components, X_i , X_j , and X_k , in Eq. 3.3 represent the same signal, then $B(f_i, f_j, f_k)$ is known as the auto-bispectrum. If one of the components represents a different signal, this is referred to as the cross-bispectrum. Only the auto-bispectrum is discussed in this thesis.

Applying the assumption of stationarity, the bispectrum is reduced to a function of two frequencies. Stationarity restricts the third component of Eq. 3.3 as such:

$$k = -(i + j) \quad . \quad (3.4)$$

Now Eq. 3.3 is modified such that

$$B(f_i, f_j) = \langle X_i X_j \bar{X}_{i+j} \rangle \quad . \quad (3.5)$$

Equation 3.5 represents the stationary bispectrum.

Several symmetry properties exist for the stationary bispectrum which reduce its domain considerably. These symmetries are stated as follows (Powers, 1990):

$$B(-f_i, -f_j) = B(f_i, f_j) \quad (3.6a)$$

$$B(f_i, f_j) = B(f_j, f_i) \quad (3.6b)$$

$$B(-f_j, -f_i) = \bar{B}(f_i, f_j) \quad (3.6c)$$

$$B(f_i, -f_j) = \bar{B}(f_i - f_j, f_j) \quad . \quad (3.6d)$$

Equation 3.6a states that all values computed in the left hand side are redundant with those on the right hand side. Equations 3.6b and 3.6c signify that the $\pm 45^\circ$ lines emanating from the origin are lines of symmetry. Symmetry also exists about the x-axis between the two octants created by the $\pm 45^\circ$ lines and the x-axis as indicated by Eq. 3.6d. This property holds for the auto-bispectrum only, not the cross-bispectrum. Of course the domain of the bispectrum is also limited by the Nyquist frequency, $f_N = \frac{f_s}{2}$, where f_s is the sampling frequency. The bispectrum

is computed only over the region where f_i and f_j are less than f_N , due to aliasing considerations. Because of these symmetries and restrictions, the stationary bispectrum is represented completely by its principle domain, shown in Fig. 3.1.

3.4 Application and Interpretation of the Bispectrum

HOSP techniques are especially suited for the detection of nonlinear features present in a signal, where the bispectrum detects quadratically nonlinear features. This property is now explained. In order for the stationary bispectrum to achieve detection, the following frequency and phase relationships must be satisfied:

$$f_i + f_j - f_{i+j} = 0 \quad (3.7a)$$

$$\phi_i + \phi_j - \phi_{i+j} = \text{constant} , \quad (3.7b)$$

where ϕ represents the phase of the Fourier transform component. As shown in Fig. 3.2, these relationships are satisfied by a system which possesses linear as well as quadratic features. The frequencies exciting the system are transferred to the response due to the linear component of the system. The quadratic component of the system results in sum and difference interactions. Harmonics of the frequencies of excitation and the sum and difference of these frequencies are present in the response. The phases associated with the input frequencies pass through these systems in a similar manner. Referring to Fig. 3.2 and assigning of the value of f_1 to f_i and f_j in Eq. 3.7a and its associated phase components in Eq. 3.7b, the following expressions result:

$$f_1 + f_1 - 2f_1 = 0$$

$$\phi_1 + \phi_1 - 2\phi_1 = 0 = \text{constant} ,$$

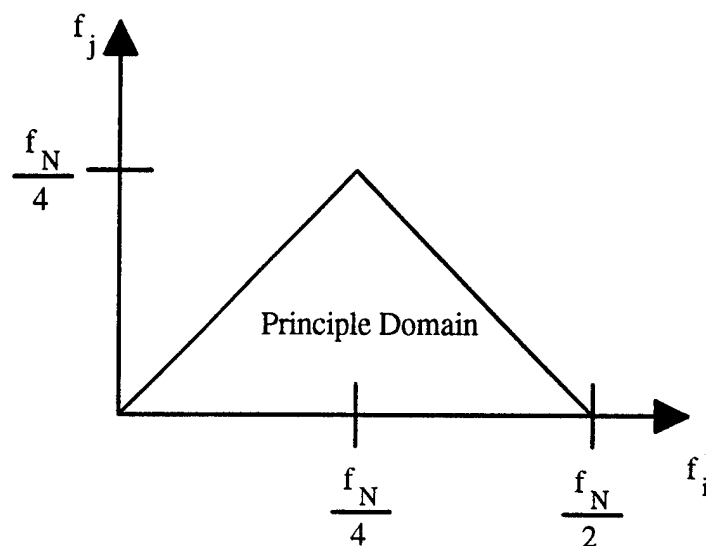


Figure 3.1: Principle Domain of the Bispectrum

ARL:UT
AS-95-357
PT - rlg
9-95

displaying the satisfaction of the frequency and phase criteria. A similar example is illustrated by substitution of f_1 for f_i and f_2 for f_j in Eq. 3.7a along with their associated phase components into Eq. 3.7b. Therefore, as shown by these examples, a system which possesses linear as well as quadratic features produces the necessary frequency and phase relationships for detection by the bispectrum.

The bispectrum can be normalized such that it returns values bounded by zero and one. The normalized bispectrum is known as the bicoherence and is presented below (Kim and Powers, 1979):

$$b^2(f_i, f_j) = \frac{\left| \langle X_i X_j \bar{X}_{i+j} \rangle \right|^2}{\langle |X_{i+j}|^2 \rangle \langle |X_i X_j|^2 \rangle} \quad (3.8)$$

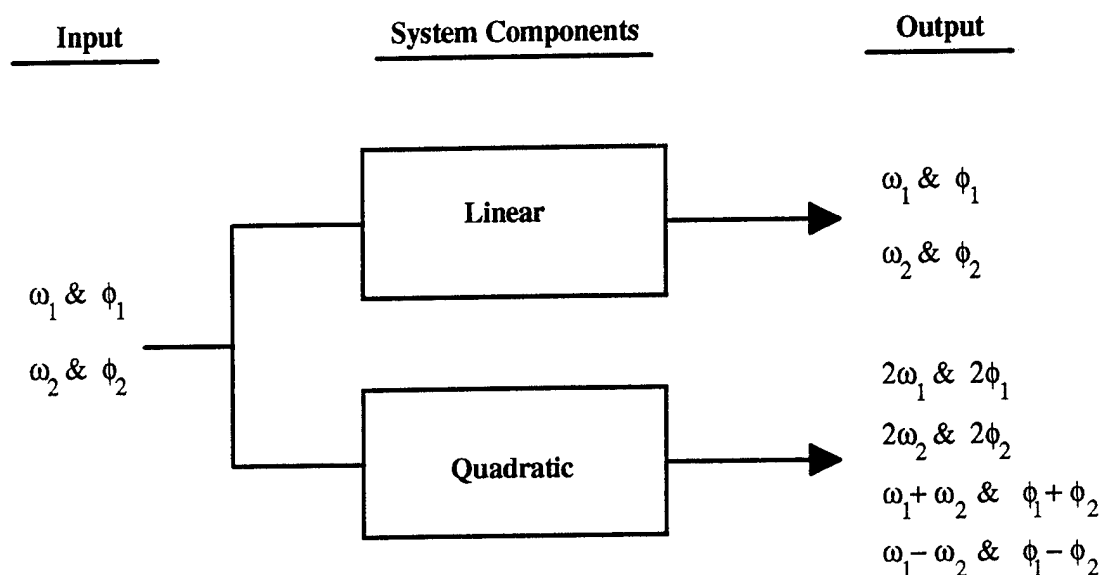


Figure 3.2: Linear and Quadratic System Responses

ARL:UT
AS-95-358
PT - rfg
9-95

The bicoherence also indicates the degree to which the energy present at frequencies f_i and f_j is coupled. More clearly, the quantity returned by the bicoherence function represents the energy present at f_{i+j} due to the coupling of energy or "waves" at f_i and f_j . This is explained more clearly by the expression which relates the bicoherence to the ratio of uncorrelated and total power present at a spectral location (Lamb, 1993):

$$b^2(f_i f_j) = 1 - \frac{P'_{i+j}}{P_{i+j}}, \quad (3.9)$$

where the P'_{i+j} represents the uncorrelated power and P_{i+j} the total power. The total power represents the power present at a spectral location due to all sources. The uncorrelated power in Eq. 3.9 refers to that which is not produced by the quadratic process, or interactions of energy, "waves," at f_i and f_j . This component refers to energy present produced by all other sources, such as noise or possibly

linear or other nonlinear processes. To summarize, for three spectral components satisfying the frequency criterion for detection of Eq. 3.7a, the bicoherence assumes the following range of values:

$$b^2(f_i, f_j) = 0 \quad \text{waves are not quadratically coupled,}$$

$$0 < b^2(f_i, f_j) < 1 \quad \text{waves are partially coupled,}$$

$$b^2(f_i, f_j) = 1 \quad \text{waves are fully coupled.}$$

The bicoherence is a good detector of quadratic interactions even when the signal is contaminated by Gaussian noise. In fact, the bicoherence of pure Gaussian noise is zero in the limit as the number of averages goes to infinity. However, only a finite number of records can be used to compute the bicoherence; thus, information concerning convergence is necessary. Elgar and Guza (1988) calculated the statistics of the bicoherence in order to address this issue. They calculated bicoherence levels for signals composed solely of noise for various numbers of averages. A relationship between the number of records averaged to compute the bicoherence and a minimum significant bicoherence value resulted. Elgar and Guza found that the bicoherence follows a chi-square distribution. This exercise was also performed, and results were verified by Lamb (1993) for the bicoherence algorithm used in this thesis. A plot of the chi-square for the 95% significance level, which is equal to $\sqrt{\frac{6}{\text{D.O.F.}}}$, is shown in Fig. 3.3. The degrees of freedom is equal to two times the number of records averaged to compute the bicoherence. Therefore, computed levels of the bicoherence should lie above this curve for a given number of averages so that the "noise only" hypothesis can be rejected. If a computed level lies below this curve, this hypothesis cannot be rejected. In this case, one is unable to determine whether this value is due to a quadratic interaction process or noise

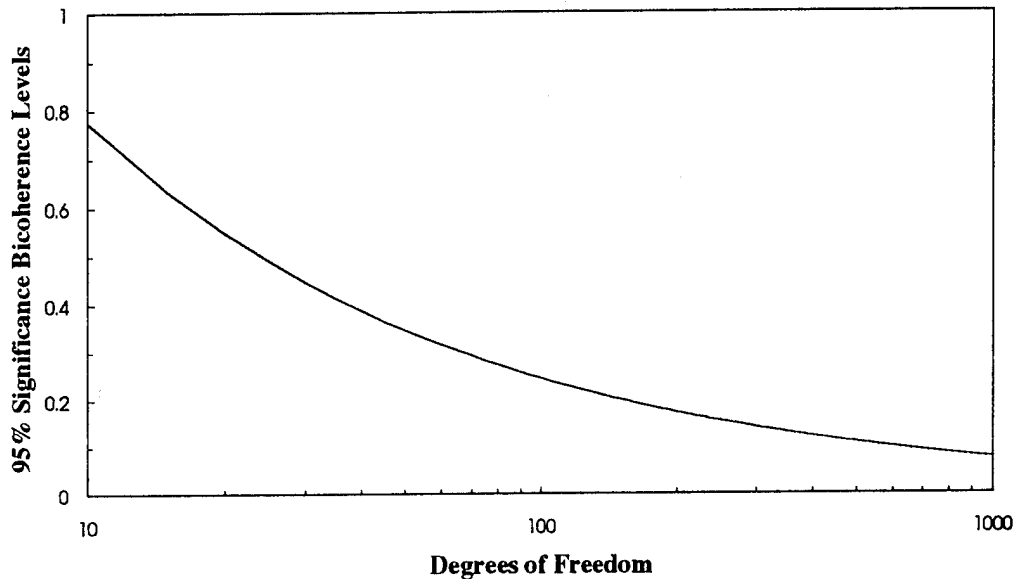


Figure 3.3: 95% Significance Level for the Bicoherence

ARL:UT
AS-95-359
PT - rfg
9-95

contaminating the signal. If a value lies above this curve, the noise only hypothesis can be rejected, and a 95% certainty of a significant bicoherence is realized.

A HOSP function, the bicoherence, has been described and can be used to interpret the strength of quadratic interactions in circular ring vibrations with geometric imperfections. As stated in Chapter 1, geometric imperfections and nonlinearities result in the linear as well as nonlinear transfer of energy in the frequency and wavenumber domain. The bicoherence allows for this transfer to be verified and quantified. By comparing bispectral signatures of individual wavenumber responses of rings with and without imperfections, the effect of geometric imperfections on this energy transfer is revealed.

CHAPTER 4: NUMERICAL SIMULATION OF RING VIBRATIONS

The subject of this chapter is the numerical simulations performed to obtain approximate solutions to the nonlinear ring equations used in this thesis. Motivating factors for obtaining these solutions are given. The solution procedure is explained and reasons for its selection are presented. Additionally, the results of the numerical simulations in the form of power spectra and bicoherence plots are displayed. Finally, some summary remarks are made to provide insight into these approximate solutions.

4.1 Motivation for Numerical Simulation

Much information can be gleaned by observing Eqs. 2.23 and 2.34. For example, quadratic features are enhanced by the presence of imperfections. Also, the presence of imperfections produces linear as well as nonlinear coupling terms between various wavenumbers. Thus, qualitatively, the effect of imperfections on the nonlinear response of a ring is clearly seen by observing Eqs. 2.34. Namely, linear as well as nonlinear transfer of energy between individual wavenumber responses is predicted, due to the coupling. Also, bicoherence levels are expected to reflect the enhancement of quadratic features occurring for rings with imperfections. However, nothing quantitative, even in an approximate sense, can be determined unless a solution to these equations is calculated. This is the primary motivation for obtaining a numerical solution to the ring equations.

The numerical simulation also assists in the preparation of the experimental portion of the study. An approximate relationship between drive force levels and vibration amplitudes, including harmonics due to nonlinear terms, is obtained. Numerical simulations also provide an expedient manner in which to develop a relationship between drive force levels and bicoherence values observed for individual wavenumber responses. It should also be noted that an approximate

analytical solution would serve these purposes as well. However, due to the complex nature of these equations, a solution through numerical integration is deemed more tractable and appropriate for this study.

4.2 Implementation of Numerical Simulation

The numerical solution method employed in this study was a Fourth Order Runge-Kutta technique. Equations 2.23 and 2.34 were integrated to a time of 2 seconds to allow for transients associated with the ring natural frequencies to sufficiently attenuate. Forty records of 512 points each were created, each with a random drive force phase. Nine modes, $n=0$ through $n=8$, were included in the integration. Higher order modes were truncated due to the high energy levels required to excite them. The data recorded was in the form of velocities, to match with the measurements to be collected in the experiment by the laser Doppler vibrometer (LDV) system, discussed in the next chapter.

As stated, solutions were calculated for a ring with imperfections as well as a ring without imperfections. The imperfection configuration of the imperfect ring matches that of the thinner ring used in the experimental study. This ring is referred to as ring B; the ring without imperfections is referred to as ring A. The amplitudes measured for the different imperfection wavenumbers for this configuration are listed in Table 4.1. Simulations were performed for drive force amplitudes of 0.1, 0.2, 0.5, 0.8, and 1.2 N (0.022, 0.045, 0.11, 0.18, 0.27 lbf) and an excitation frequency of 187.5 Hz. Broadband, random noise was added to each record at a level comparable with the sensitivity expected from the LDV measurement system. This corresponded to a noise floor of approximately

$$1 \times 10^{-11} \frac{\text{m}^2}{\text{s}^2} \left(1.6 \times 10^{-8} \frac{\text{in}^2}{\text{s}^2} \right)$$

in the power spectrum.

The physical properties of the ring with imperfections and the ring without imperfections used in numerical simulation were as follows:

$$E = 1.95 \times 10^{11} \text{ Pa } (30 \times 10^6 \text{ psi}) \quad \rho = 7.7 \times 10^3 \text{ kg/m}^3 (.28 \text{ lbf/in}^3)$$

$$h = .86 \text{ mm } (.034 \text{ in}) \quad b = 2.22 \text{ cm } (.875 \text{ in})$$

$$R = 12.2 \text{ cm } (4.80 \text{ in}) \quad \beta_n = 15 + .000004 \omega_n^2 \text{ sec}^{-1}$$

where b is the "height" of the ring and the material properties are those of steel. These properties matched those of the rings considered in the experimental study, except for the thickness, which matched only the thinner ring of the experiment. The theoretical natural frequencies of ring A are presented in Table 4.2. These natural frequencies were calculated using Eq. 2.22. Since the excitation frequency was 187.5 Hz, the $n=4$ wavenumber responded with the greatest amplitude.

Table 4.1: Imperfection Wavenumber Amplitudes for Ring B

n	δ	$\bar{\delta} = \frac{\delta}{h}$
2	$1.15 \times 10^{-1} \text{ mm } (4.53 \times 10^{-3} \text{ in})$	0.133
3	$7.43 \times 10^{-2} \text{ mm } (2.93 \times 10^{-3} \text{ in})$	0.0860
4	$3.18 \times 10^{-2} \text{ mm } (1.25 \times 10^{-3} \text{ in})$	0.0368
5	$3.11 \times 10^{-2} \text{ mm } (1.22 \times 10^{-3} \text{ in})$	0.0360

The excitation orientation for the simulation of the ring with imperfections was an affine configuration; i. e., the excitation was "aligned" with the imperfection waveforms. Therefore, all of the imperfection phase components ($\cos\phi$) were set equal to unity. This assumes all imperfection wavenumber anti-nodes can be aligned with the excitation. In practice, this may be unachievable; yet, it effectively displays the maximum effect of the imperfection set on the ring response, rather than the effect of an individual imperfection component.

Table 4.2: Theoretical Natural Frequencies of Ring A

n	Natural Frequency (Hz)
0	6587.
2	40.51
3	108.0
4	202.6
5	324.1
6	472.6
7	648.2
8	850.7

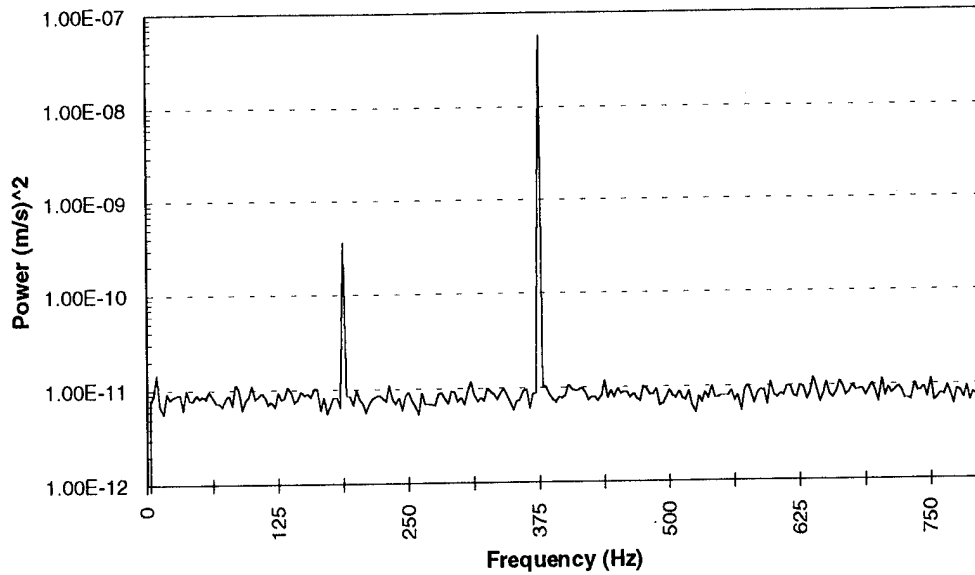
4.3 Discussion of Numerical Solution Results

The power spectrum and bicoherence of the $n=0$ wavenumber response to an 187.5 Hz excitation frequency and 1.2 N drive force level for ring A are shown

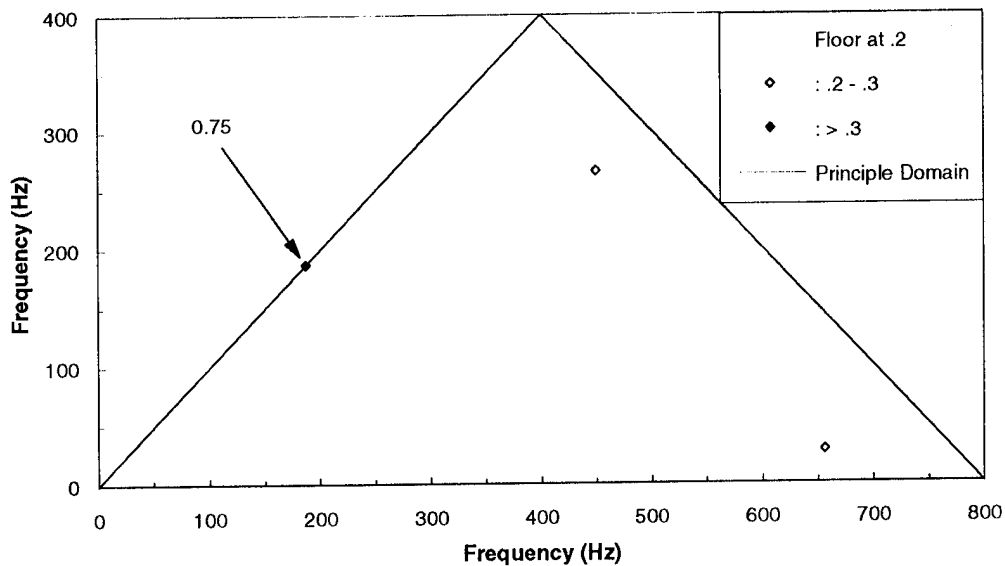
in Fig. 4.1. The strong second harmonic of 375 Hz is the dominant feature of the power spectrum. The significant amplitude of this peak is due to the nonlinear coupling between all wavenumbers included in the response and the $n=0$ wavenumber, as referred to in Eq. 2.23b. The linear response at 187.5 Hz corresponds to the direct excitation of the $n=0$ wavenumber due to the excitation condition. That is, a concentrated or spatially localized force input excites all wavenumbers. For this drive force level, the nonlinear coupling is actually stronger than the direct linear excitation of the breathing mode. With a drive force level of 1.2 N, the response amplitudes of the $n \geq 1$ wavenumbers are large enough such that more energy is present at the second harmonic, 375 Hz, of the $n=0$ wavenumber than at the linear peak.

Figure 4.1b shows that the value of the bicoherence at $f_1=187.5$ Hz, $f_2=187.5$ is 0.75. Referring back to Chapter 3, detection by the bicoherence requires energy present at frequency f_1+f_2 to be quadratically coupled to energy present at frequencies f_1 and f_2 . More clearly, the bicoherence will detect a quadratic interaction process, where "waves" at f_1 and f_2 are interacting to produce a "wave" at f_1+f_2 . In this case the interacting waves are actually the single wave present at the linear frequency, 187.5 Hz. The energy at 375 Hz is due to quadratic coupling with the $n \geq 1$ wavenumbers (see Eqs. 2.23). These $n \geq 1$ wavenumbers are responsible for the energy at the second harmonic, 375 Hz. This energy transfer arises from the third term in Eq. 2.23b, which does not contain a contribution from the $A_0(t)$ term. Thus, the interacting "waves" are actually the energy present at the 187.5 Hz frequency of the $n \geq 1$ wavenumbers, due to linear response of the excitation. The wave these interacting waves are producing is the energy at the 375 Hz peak of the $n=0$ wavenumber.

From Eq. 2.23b, it is evident that the $A_0(t)$ response is driven in a linear manner by the forcing function wavenumber component, $F_0(t)$, and in a quadratic manner by the higher wavenumber terms $A_n^2(t)$, with $n \geq 1$. Even though for the $n=0$ wavenumber, energy at the quadratic peak is not produced by the energy at



a.) Power Spectrum of n=0 Wavenumber Response



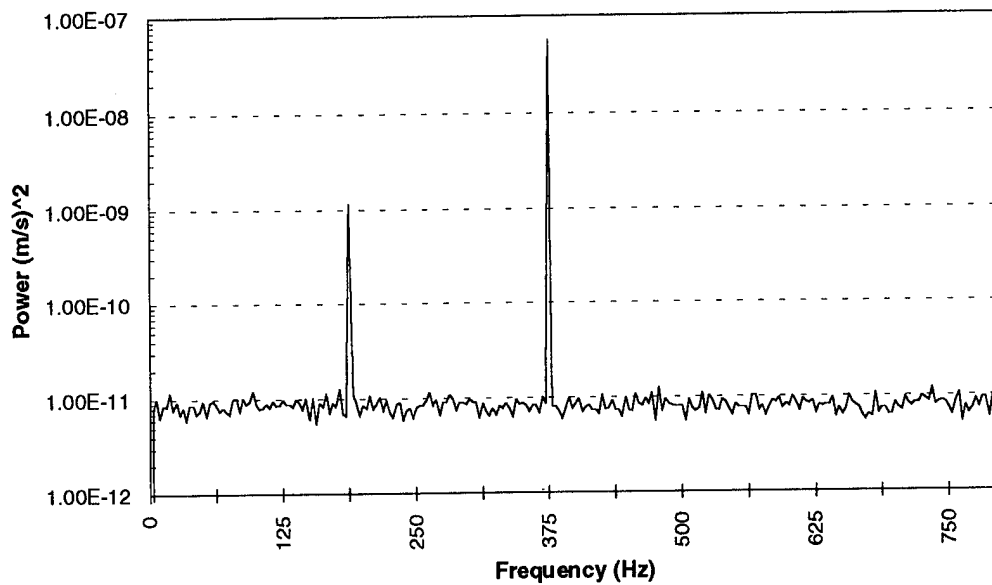
b.) Bicoherence of n=0 Wavenumber Response

Figure 4.1: Numerical Simulation Results for Ring A, Drive Force Level=1.2 N

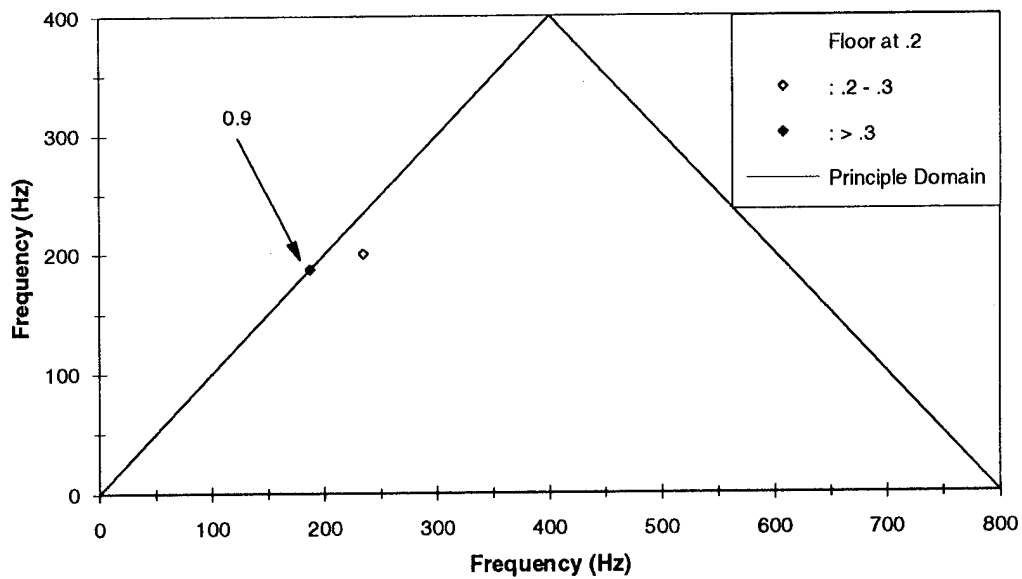
the linear peak, the energy at 187.5 Hz for this wavenumber and all the other wavenumbers is produced by the same source. Thus, the bicoherence frequency and phase relationships for the response of the $n=0$ wavenumber are satisfied. Referring back to Eq 3.9, a bicoherence value of 0.75 means that approximately 75% of the energy at 375 Hz is due to the quadratic interaction at 187.5 Hz.

Initially, the effect of imperfections are displayed in Fig. 4.2. These figures represent the power spectrum and bicoherence for the same excitation configuration as Fig. 4.1, but for ring B, the ring with imperfections. The magnitude of the second harmonic, 375 Hz, remains the same. However, the amplitude of the linear frequency, 187.5 Hz, is greater by a factor of 2.5. This is due to the linear coupling which is present for the ring with imperfections, yet absent for the perfect ring. This can be seen by comparing Eqs. 2.23 and 2.34. All wavenumbers with an imperfection present are linearly coupled to the breathing mode ($n=0$); thus, energy is transferred in a linear fashion to this lower order wavenumber. The effect of imperfections is also reflected in the bicoherence. The value of the bicoherence is now 0.90, 20% greater than for Ring A. This difference is due to the increase in the signal to noise ratio of the linear peak.

The numerical simulation results for the excitation force amplitude of 0.8 N are shown in Figs. 4.3 and 4.4. As expected, the linear response amplitudes for both rings A and B have decreased. However, a more dramatic decrease is observed for ring A, as displayed in Fig. 4.3a. The power spectrum for ring B indicates that the energy present at 187.5 Hz due to coupling is an order of magnitude greater than that due solely to the linear excitation of the $n=0$ wavenumber. This is seen by comparing Fig. 4.4a, representing the direct excitation due to the source, and Fig. 4.4b, representing the result of this direct excitation plus the linear coupling due to the presence of imperfections. The bicoherence plots for rings A and B also reflect the effect of the imperfections for this excitation condition. The value of the bicoherence is 0.96 for ring B, while its

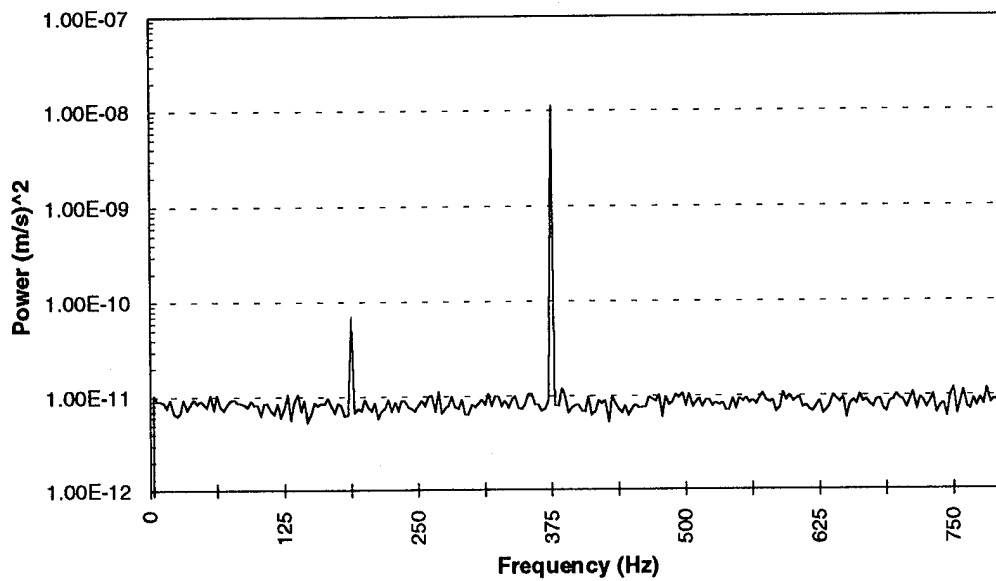


a) Power Spectrum of n=0 Wavenumber Response

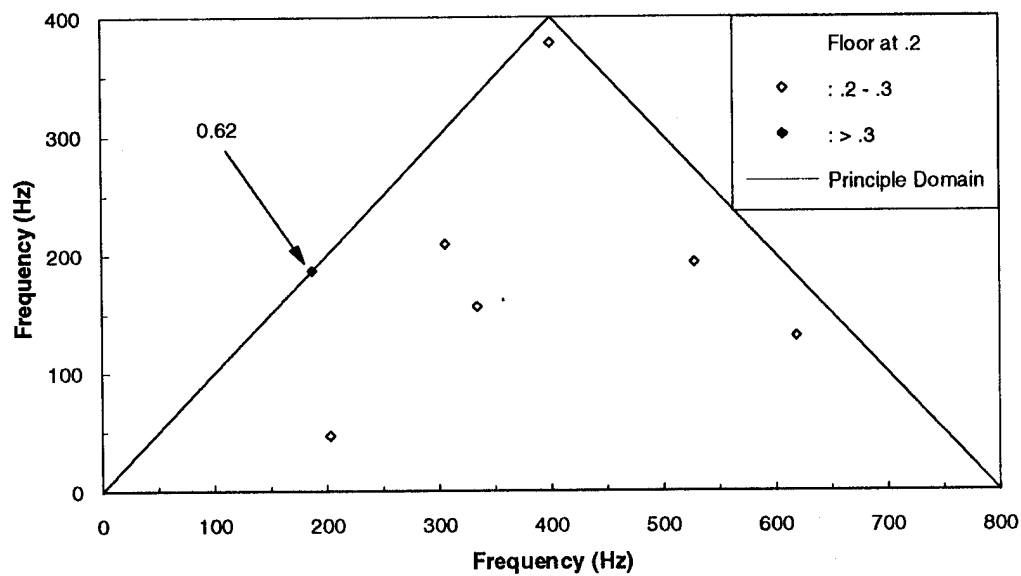


b.) Bicoherence of n=0 Wavenumber Response

Figure 4.2: Numerical Simulation Results for Ring B, Drive Force Level=1.2 N

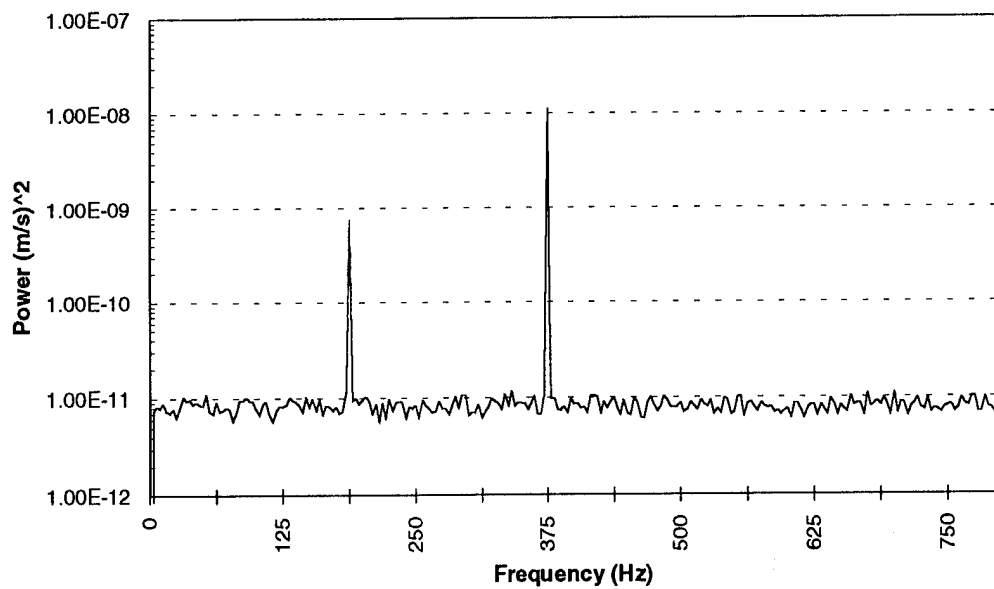


a.) Power Spectrum of n=0 Wavenumber Response

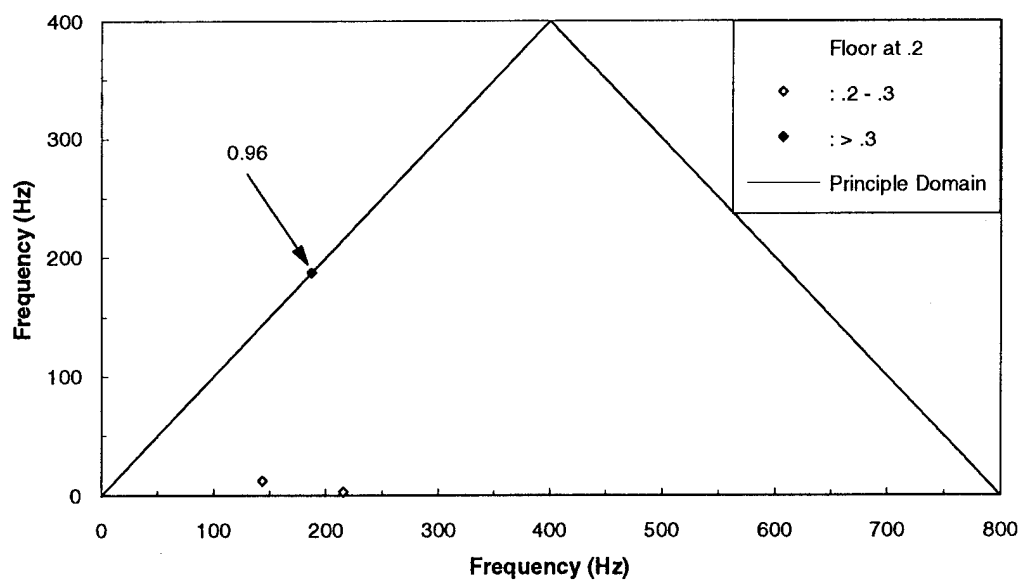


b.) Bicoherence of n=0 Wavenumber Response

Figure 4.3: Numerical Simulation Results for Ring A, Drive Force Level = 0.8 N



a.) Power Spectrum of n=0 Wavenumber Response



b.) Bicoherence of n=0 Wavenumber Response

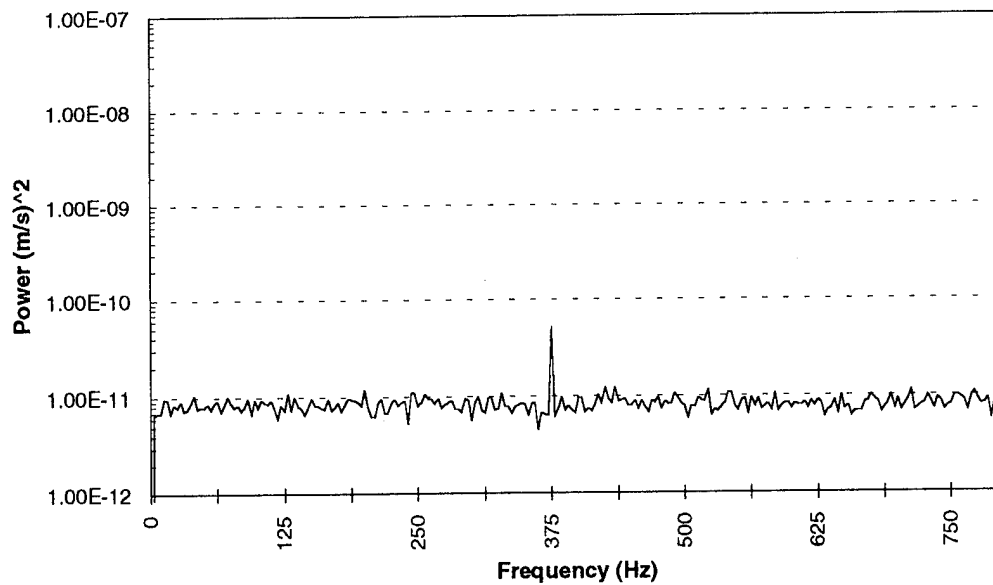
Figure 4.4: Numerical Simulation Results for Ring B, Drive Force Level = 0.8 N

value is 0.67 for ring A, a 30% difference. Once again, the increase in signal to noise ratio of the linear peak for ring B over ring A explains the bicoherence trend.

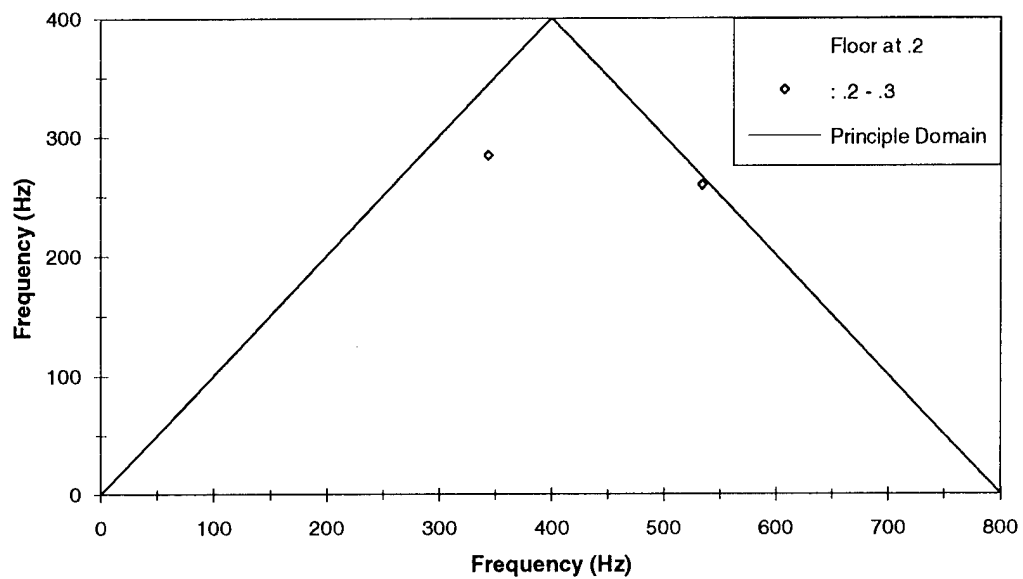
The power spectrum and bicoherence of the $n=0$ wavenumber response for rings A and B with a drive force level of 0.2 N are displayed in Figs. 4.5 and 4.6. As displayed by Fig. 4.5a, the linear response peak is now buried in the noise while the second harmonic is still visible. For 40 averages, the bicoherence does not produce a significant value as indicated in Fig. 4.5b. For the ring with imperfections, however, ring B, the 187.5 Hz and 375 Hz peaks are now of the same relative magnitude. The value of the bicoherence at $f_1=f_2=187.5$ Hz is now 0.48, half the value for the 0.8 N level case.

Finally, the numerical simulation results for the 0.1 N excitation drive force level are shown in Fig. 4.7. The results for ring A are not displayed since neither the linear or quadratic response peaks were discernible from the noise floor. As in the 0.2 N case, the bicoherence did not produce a value above the 95% significance level for 40 averages. However, it should be noted that for both cases, 0.1 N and 0.2 N, an increased number of averages would have presumably permitted the bicoherence to detect the coupling. The power spectrum of the $n=0$ response for ring B indicates that the linear response peak is still detectable, above the noise floor. The bicoherence is now unable to detect the quadratic nature of the response. Thus, threshold drive force levels and response amplitudes to produce a significant value in the bicoherence are established for this noise floor and number of averages.

The effect of the linear and nonlinear coupling on the $n=0$ wavenumber response due to imperfections is clearly seen. For the drive force level of 0.2 N, the linear response peak of the $n=0$ response for the ring without imperfections, ring A, is not discernible. However, for ring B, this peak is clearly distinguishable from the background noise. For the 0.1 N drive force level, the response of the $n=0$ wavenumber does not produce a significant bicoherence value for either ring.

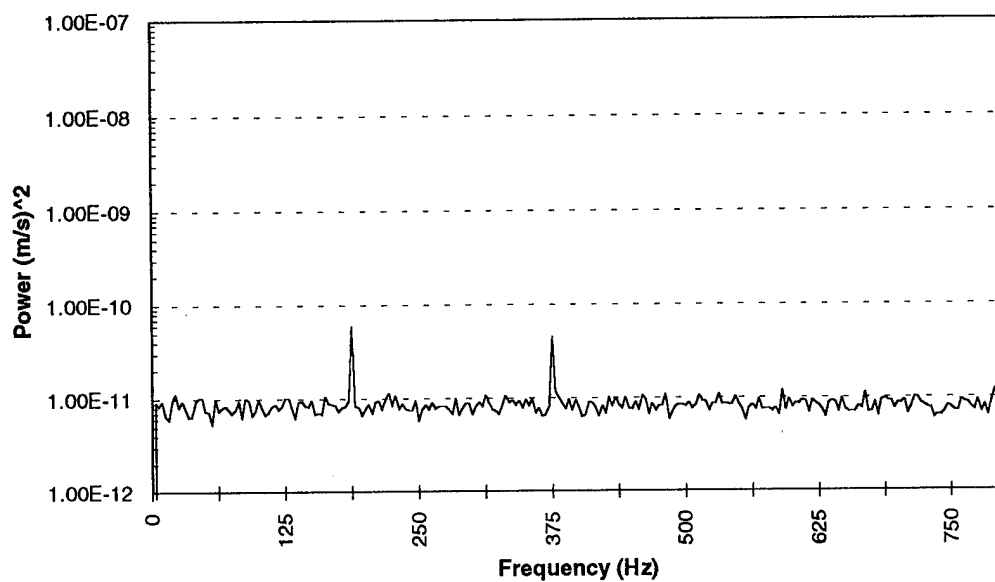


a.) Power Spectrum of n=0 Wavenumber Response

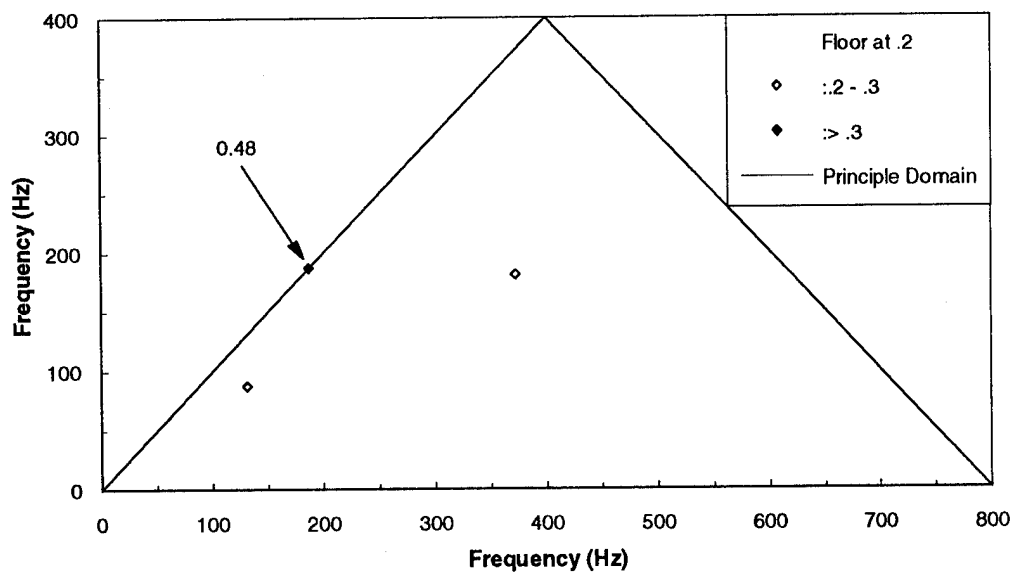


b.) Bicoherence of n=0 Wavenumber Response

Figure 4.5: Numerical Simulation Results for Ring A, Drive Force Level = 0.2 N

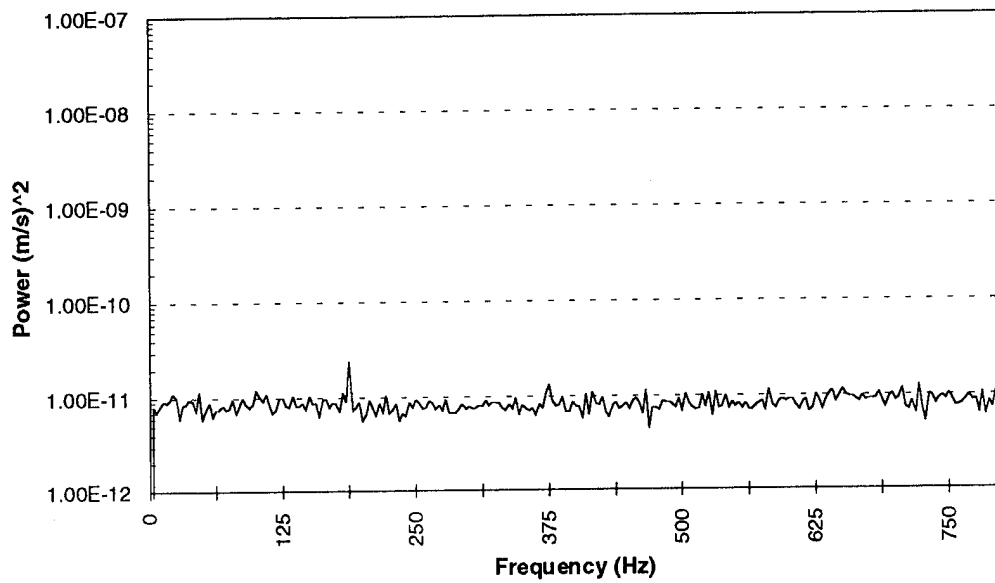


a.) Power Spectrum of n=0 Wavenumber Response

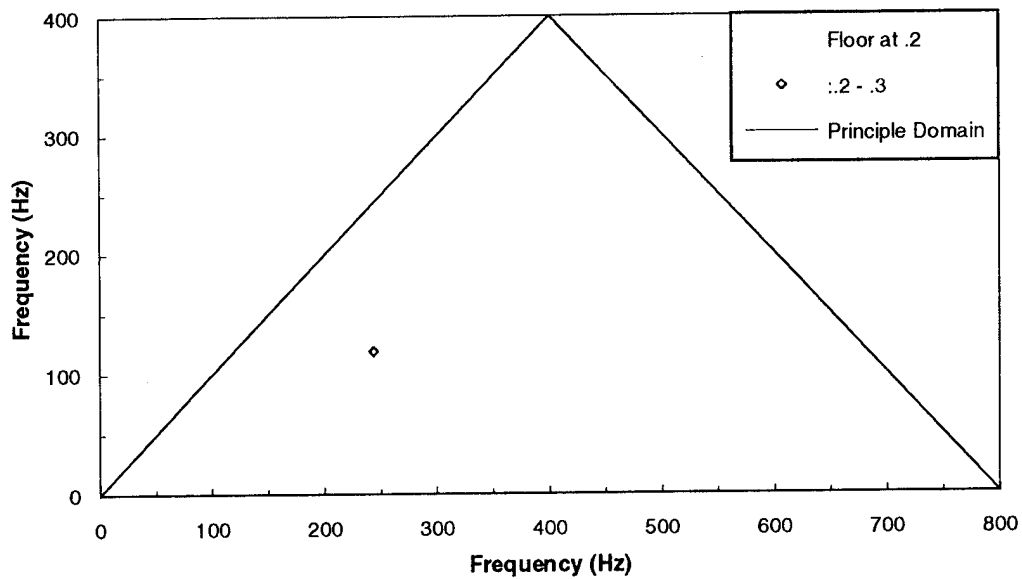


b.) Bicoherence of n=0 Wavenumber Response

Figure 4.6: Numerical Simulation Results for Ring B, Drive Force Level = 0.2 N



a.) Power Spectrum of n=0 Wavenumber Response



b.) Bicoherence of n=0 Wavenumber Response

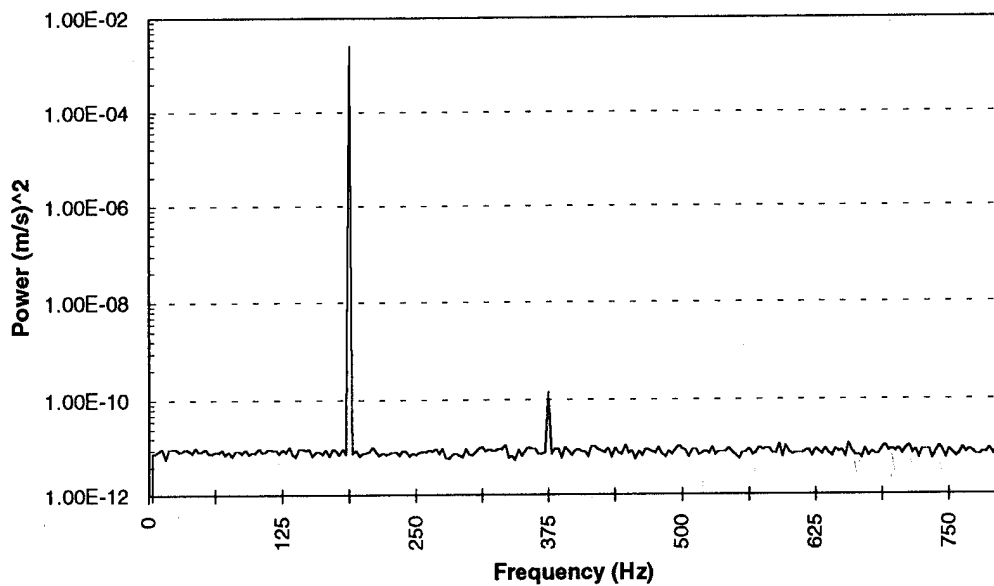
Figure 4.7: Numerical Simulation Results for Ring B, Drive Force Level = 0.1 N

However, the linear response is still visible for ring B. This is due to the linear coupling present between the wavenumbers with imperfections present and the $n=0$ wavenumber. Thus, not only have the quadratic features of the response of the $n=0$ wavenumber been enhanced due to imperfections, the linear features have as well.

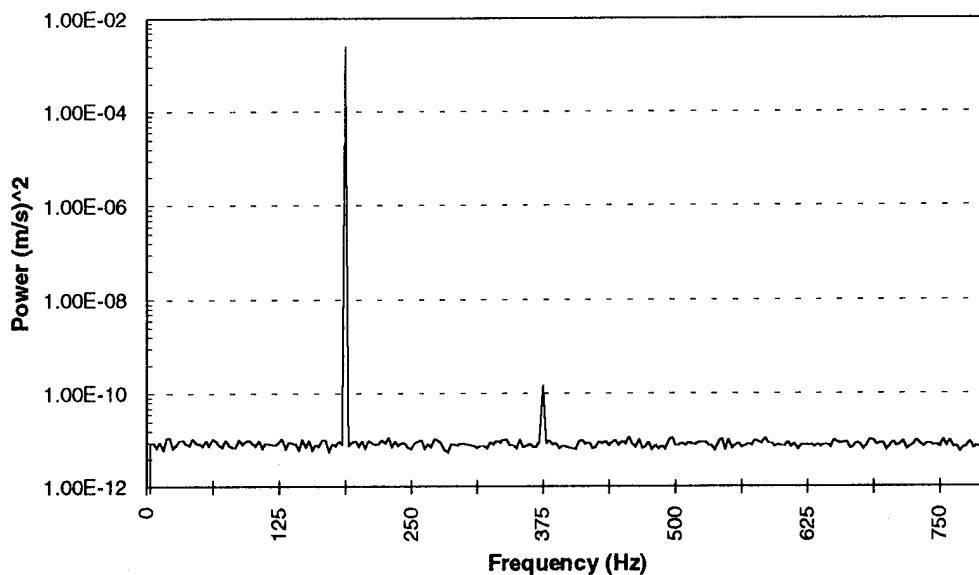
The response of the $n=3$ and $n=4$ wavenumbers of ring A and B for the 0.8 N case are shown in Figs. 4.8 and 4.9. The quadratic features are easily noted in the $n=4$ wavenumber response power spectra. Since the excitation frequency is closest to the natural frequency of the $n=4$ wavenumber, this wavenumber responds at the largest amplitude. Thus, the nonlinear features of this wavenumber are the most prominent, as well. The bicoherence values computed for the response of this wavenumber are displayed in Tables 4.3 and 4.4. As indicated by their bicoherence values, the quadratic features of this wavenumber response are almost identical for rings A and B. The slight difference between the two can be attributed to noise.

The 375 Hz peak is virtually hidden by the noise in the $n=3$ wavenumber response power spectrum. However, as indicated by Table 4.3, the bicoherence is able to detect the quadratic interaction present. Even though the power spectra of the $n=3$ wavenumber response for rings A and B are quite similar, the bicoherence values are not. For ring B, a bicoherence value of 0.48 is recorded, while for ring A it is only 0.30.

The numerical simulations show the effect that imperfections can have on the linear and nonlinear vibration response of circular rings. Due to linear coupling present for the ring with imperfections, the amplitude of the linear response of the $n=0$ mode increased. The bicoherence values of the $n=0$ wavenumber responses were also greater for the ring with imperfections than for the ring without. The effect of imperfections were exhibited by the response of the $n=2$ and $n=3$

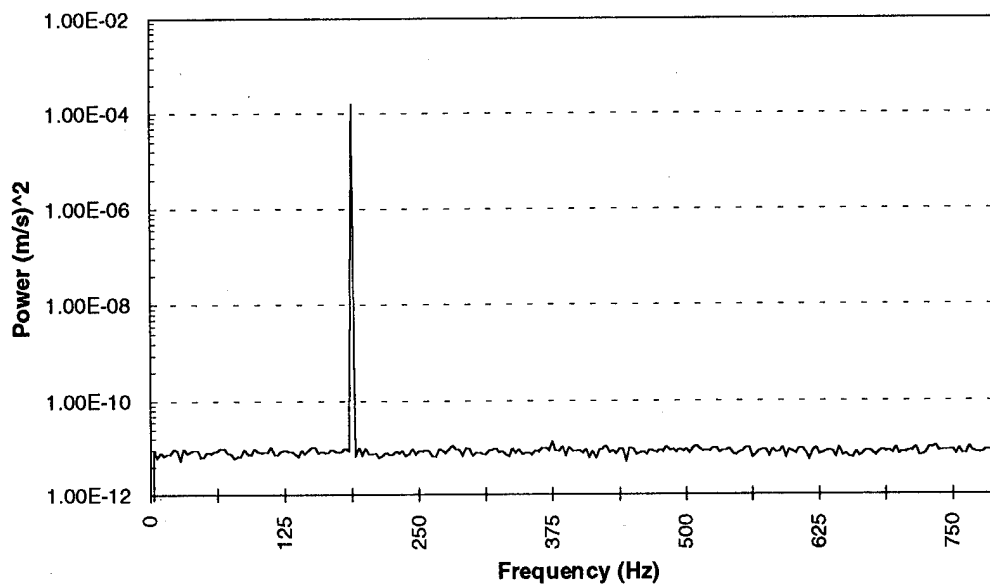


a.) Power Spectrum of Ring A Response

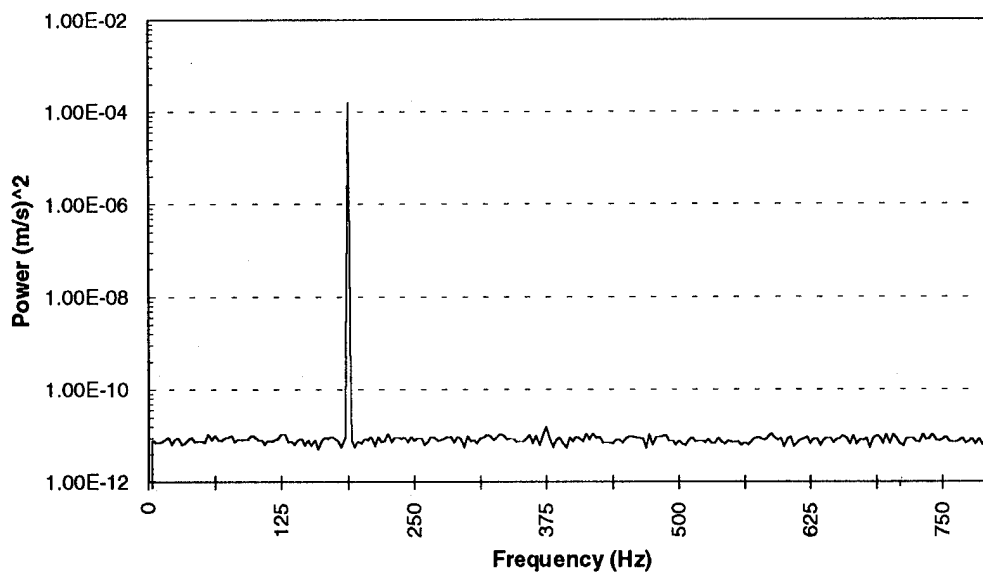


a.) Power Spectrum of Ring B Response

Figure 4.8: Numerical Simulation Results for $n=4$ Wavenumber,
Drive Force Level = 0.8 N



a.) Power Spectrum of Ring A Response



b.) Power Spectrum of Ring B Response

Figure 4.9: Numerical Simulation Results for $n = 3$ Wavenumber,
Drive Force Level = 0.8 N

Table 4.3: Bicoherence Levels at $f_1=187.5$, $f_2=187.5$ for Ring A *

Drive Force Level (N)	n=0	n=2	n=3	n=4
.2	-	-	-	-
.5	-	-	-	.74
.8	.62	-	.30	.96
1.2	.75	-	.45	.99

(* "-" denotes bicoherence value is below 95% significance level)

Table 4.4: Bicoherence Levels at $f_1=187.5$, $f_2=187.5$ for Ring B *

Drive Force Level (N)	n=0	n=2	n=3	n=4
.2	.48	-	-	-
.5	.91	-	.24	.7
.8	.96	-	.48	.95
1.2	.90	.54	.85	.98

(* "-" denotes bicoherence value is below 95% significance level)

wavenumbers, as well. The response of these wavenumbers experienced the same trend for the bicoherence. Namely, the ring with imperfections present exhibited greater bicoherence values than the ring without imperfections. However, the $n=4$ wavenumber response displayed no effect of the imperfections. For a given drive force level, the bicoherence returned similar values for both rings. Referring back to Table 4.1, it is evident that the $n=4$ imperfections wavenumber is significantly smaller in amplitude than that of the $n=2$ or $n=3$. Hence, by Eq. 2.34a, the response of this wavenumber should not exhibit the same pronounced impact of imperfections as that of the $n=2$ or $n=3$ wavenumbers.

Another significant finding of the numerical simulations involves the strength of the second harmonic, 375 Hz, peak for both the case with imperfections and the case without. As stated, the presence of this peak in the $n=0$ wavenumber response is due to the nonlinear, quadratic coupling between the $n=0$ and $n \geq 1$ wavenumber responses. This suggests that the effect of nonlinearities on transition of energy from higher order modes to the breathing mode is significant. In fact, the nonlinear features of the $n=0$ wavenumber response are more prominent than those of the $n=4$ wavenumber, which has the greatest linear response amplitude. This is seen by comparing the responses of the $n=0$ and $n=4$ wavenumbers for the 0.8 N case, Figs. 4.3a, 4.4a, and 4.8. In fact, the energy at the 375 Hz frequency is 100 times, or 20 dB, greater for the $n=0$ wavenumber response than for the $n=4$ wavenumber response. This is consistent for the case without imperfections as well.

The numerical simulation results provided useful insight into the nonlinear vibrations of rings with imperfections. The next chapter describes the experimental portion of the study. The experimental setup and procedure are described and explained. The results of the experiment are presented and discussed. Comparisons with the trends observed in the numerical simulation results are also discussed.

CHAPTER 5: EXPERIMENTAL PROCEDURE AND RESULTS

This chapter details the setup and procedure used to measure the influence of geometric imperfections on the nonlinear vibrations of circular rings. The results obtained from this experimental investigation are also included. A description of the procedure used for data reduction is reserved for Appendix A; however, a description of the data collection procedure and a diagram of the experimental setup are presented. Two rings of different thicknesses were each excited at two different spatial locations. One location was selected to emphasize the effect of imperfections, the other to de-emphasize the effect. The response characteristics of individual wavenumbers are presented for each ring and each excitation configuration.

5.1 Description of Experimental Setup

The experimental setup is depicted in Fig 5.1. The dynamic force was applied to the ring via an electrodynamic shaker and connecting stinger. The force gage, attached to the stinger, was used to monitor the input force to the ring. The electrodynamic shaker was driven by the source module contained in a Hewlett-Packard 3567A Dynamic Signal Analyzer (HP 3567A DSA) system. The source module provided a single frequency, variable amplitude signal with low harmonic distortion (<60 dB). The rings were supported with lightweight nylon string and allowed to hang from the support plate at three circumferential locations.

A laser Doppler vibrometer (LDV) measurement system was used to measure the response of the rings at multiple spatial locations. The probe head of the LDV measurement system was attached to a traversing arm, allowing it to traverse about the circumference of the ring. The transmission and collecting optics were both housed in the probe head. The beam produced by a HeNe laser

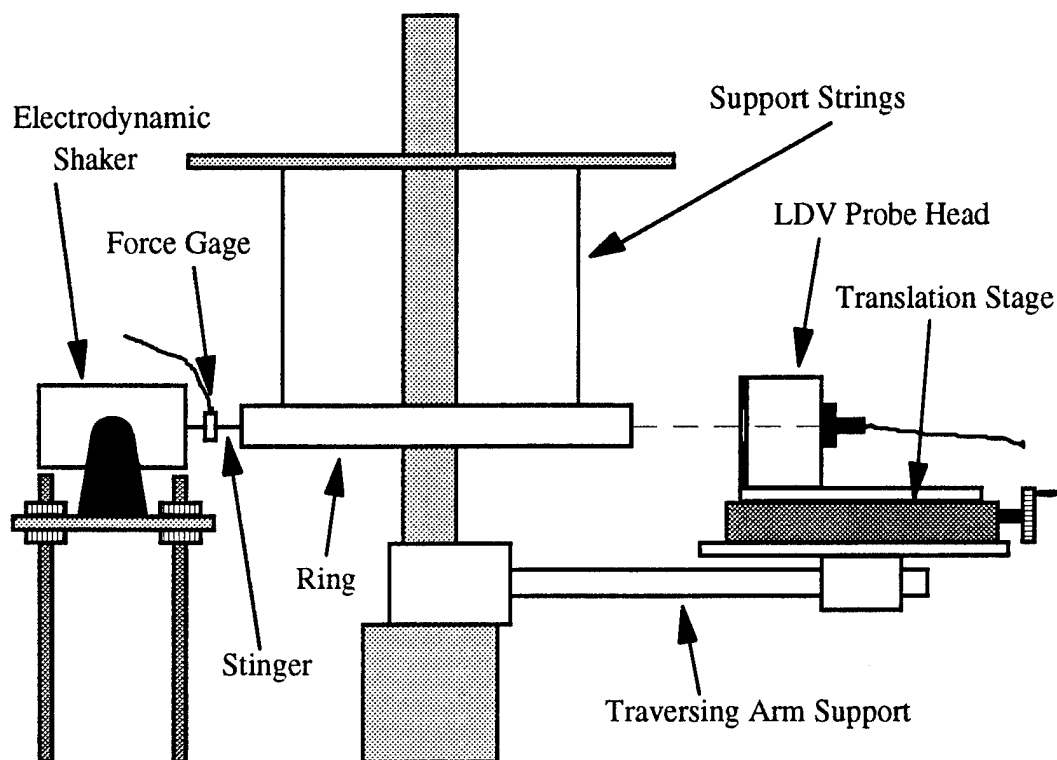


Figure 5.1: Diagram of Experimental Setup

ARL:UT
AS-95-369
PT - rfg
9-95

(12 mW) was projected onto the surface of the ring, and the reflected beam collected by the collection collimator. The LDV measurement system produced a voltage proportional to the velocity of the surface on which the beam was projected. The velocity component measured was that which was collinear to the bisector of the incident and reflected beam. The calibration curve for the LDV system is shown in Fig. 5.2. The calibration constant for this system, the slope of the best fit line in Fig. 5.2, was $2.28 \times 10^{-2} \text{ (m/s)/V}$.

As shown in Fig. 5.1, the probe head was mounted on a translation stage. The signal to noise ratio characteristics of the LDV system were very sensitive to the alignment of the collection optics and the ring surface. The translation stage

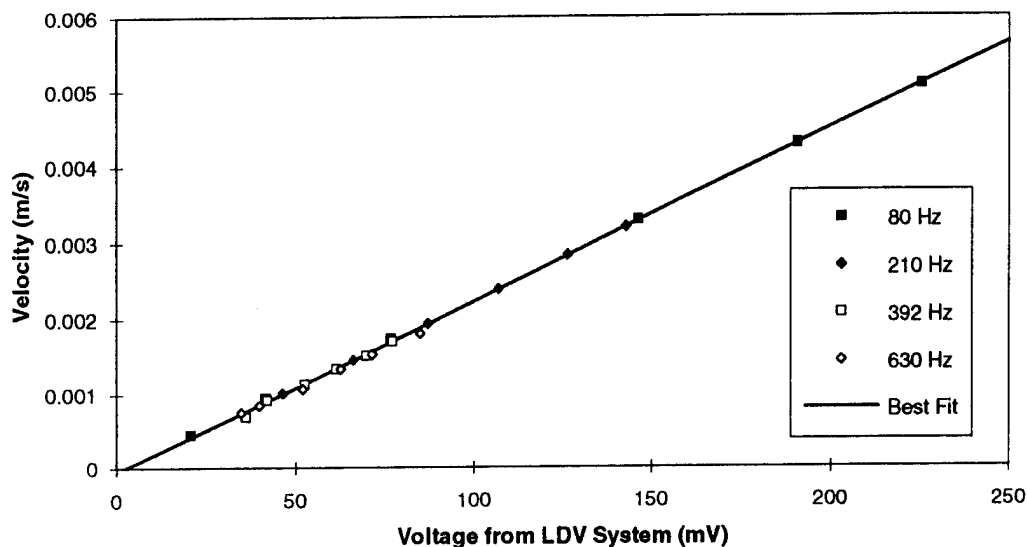


Figure 5.2: Calibration Curve of the LDV Measurement System

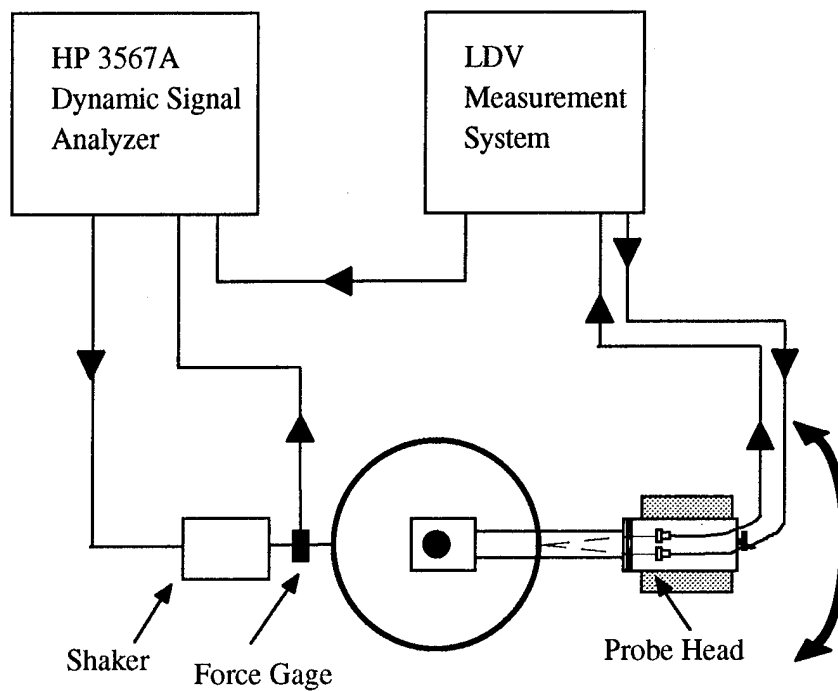
ARL:UT
AS-95-370
PT - rfg
9-95

was used to optimize this alignment by allowing for the radial distance between the collection optics and the ring surface to be modified, thus maximizing the signal to noise ratio characteristics of the LDV signal. The mounting screw, which attached the probe head to the traversing arm, was also adjusted to make minor corrections in the orientation of the probe head in the vertical plane. Lamb (1993) presents a detailed description of the LDV measurement system. In fact, the system used in this experimental investigation is identical to that detailed by Lamb, with the exception of the focal length of the lens used in the collection and transmission optics. For this system the focal length is 125 mm, whereas Lamb used a lens of 500 mm focal length.

5.2 Experimental Procedure

The rings were sampled at eight equally spaced spatial locations, from $\theta = \frac{\pi}{8}$ to $\theta = \pi$ ($\theta = 0$ corresponds to the point of excitation). This limited the response wavenumbers measured to $n \leq 7$. The data reduction procedure which produced the wavenumber or modal responses of the ring is described in Appendix A. The response at a given spatial location, as measured by the LDV system, was digitized using the HP 3567A DSA. The signals from the force gage and the LDV system were sampled, simultaneously, at a frequency of 2048 Hz. Eleven seconds of data were acquired at each location to allow for at least 40 records of 512 points to be collected. A schematic of the experimental setup and acquisition system is shown in Fig. 5.3.

Two rings of different thicknesses and imperfection configurations were tested. The two rings used in the experimental investigation had thicknesses of 0.86 mm (0.034 in) and 1.7 mm (0.070 in). They were constructed of steel with the same assumed properties as presented in Section 4.2. The imperfection configuration of the 0.86 mm thickness ring is presented in Table 4.1 on page 43. The imperfection configuration of the 1.73 mm thickness ring is presented in Table 5.1. The imperfections were measured by Fox (1993), and a detailed description of the procedure employed is contained in this reference. The measured natural frequencies of the first seven modes for both rings are presented in Tables 5.2 and 5.3. The rings were excited at two different spatial locations, one considered "affine," the other "orthogonal" to the imperfection configuration. "Affine" means the excitation was aligned with an individual wavenumber imperfection component such that the effect of the imperfection component is maximized, as outlined in Section 2.2. "Orthogonal" refers to the location at which the effect of the imperfections is minimized; i. e., the excitation is completely out of phase with an individual imperfection component.



5.3 Schematic of Experimental Setup and Data Acquisition System

ARL:UT
AS-95-371
PT - rlg
9-95

Table 5.1 : Imperfection Configuration of 1.7 mm Thickness Ring

n	δ	$\bar{\delta} = \frac{\delta}{h}$
2	5.82×10^{-2} mm (2.29×10^{-3} in)	0.0342
3	9.28×10^{-2} mm (3.65×10^{-3} in)	0.0546

Table 5.2: Measured Natural Frequencies of 0.86 mm Thickness Ring

n	Natural Frequency (Hz)
2	31.3
3	93.8
4	188.
5	313.
6	469.
7	641.

Table 5.3: Measured Natural Frequencies of 1.7 mm Thickness Ring

n	Natural Frequency (Hz)
2	78.1
3	219.
4	413.
5	663.
6	1013.
7	1338.

For the 0.86 mm thickness ring, the spatial location for the affine configuration was such that the excitation was approximately aligned with all of the imperfection components, or waveforms. Therefore, the effect of each individual imperfection component was maximized. A similar arrangement was achieved for the orthogonal case for this ring as well. A location was selected which approximately minimized the effect of each imperfection configuration. However, for the 1.7 mm ring, the affine and orthogonal configurations refer to an emphasis and de-emphasis of only the $n=3$ waveform imperfection component. The imperfection components were arranged in this ring such that only one waveform in the imperfection configuration could be made affine or orthogonal to the excitation. Thus, the dominant imperfection wavenumber, $n=3$, was selected.

The 0.86 mm thickness ring was excited at a frequency of 80 Hz for the affine and orthogonal configurations. This excited predominantly the $n=3$ wavenumber. The 1.7 mm thickness ring was excited at a frequency of 204 Hz for the affine and orthogonal cases. This excitation frequency also resulted in a dominant response of the $n=3$ wavenumber, as expected when reviewing Table 5.2. The rings were excited at these frequencies because of the inability to excite nonlinear responses at higher frequencies, or higher modes, and the limitations of the electrodynamic shaker used. Both rings were excited at a drive force level of approximately 160 mN (0.036 lbf).

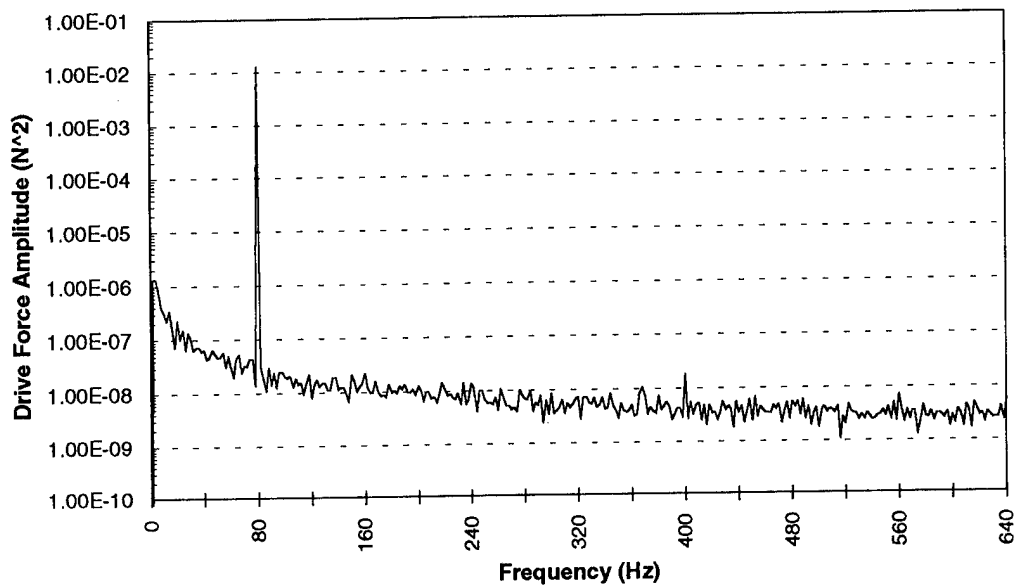
5.3 Experimental Results and Discussion

As obtained from the results of the analytical and numerical studies, the main hypotheses of this thesis are now presented. First, the transition of energy from higher order wavenumbers to lower order wavenumbers due to nonlinear coupling is predicted. This feature does not seem to be affected by imperfections. A similar energy transition due to linear coupling is also expected. However, in this case of linear coupling, the energy transfer mechanism is due solely to imperfections. The bicoherence of the $n=0$ wavenumber response should increase

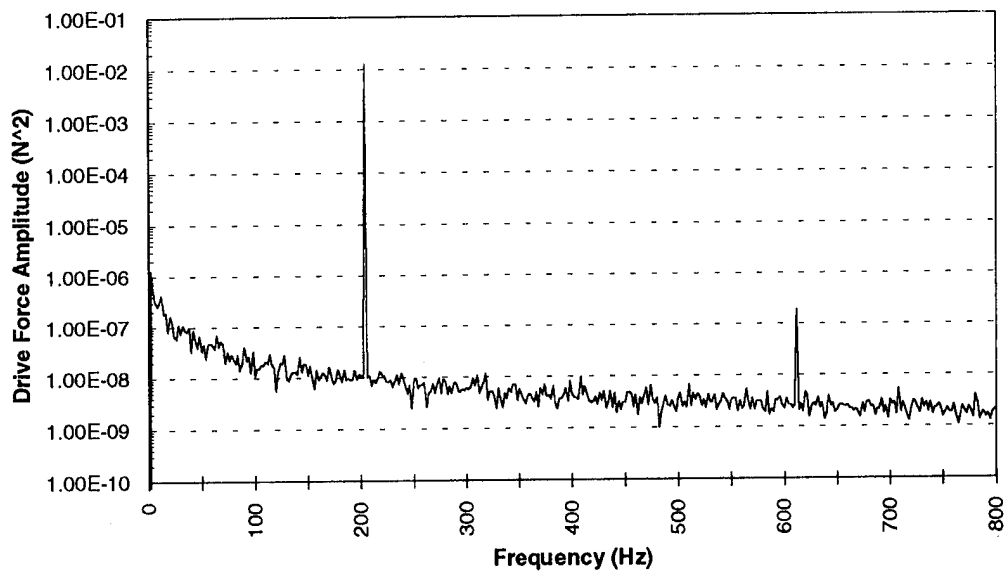
due to the impact of imperfections introducing more wavenumber coupling. For the numerical simulations, this was due to an increase in the signal to noise ratio of the linear response peak. The bicoherence of the primary response mode shows no effect of the imperfections; yet, for the numerical simulation, the imperfection amplitude at this wavenumber is very small. The analytical study suggests that for larger imperfection amplitudes, quadratic response features are enhanced. Finally, the $n=0$ wavenumber response contains stronger quadratic features than the other wavenumbers responding. This is evidenced by more energy present at the second harmonic frequency of the $n=0$ wavenumber response than at this frequency for the other wavenumber responses.

The data collected at the eight spatial locations for two of the experimental runs is contained in Appendix B. As stated in section 5.2, the source signal amplitude was such that the rings were excited at a drive force level of approximately 160 mN with low harmonic distortion. The input force to the rings, as measured by the force gage connected to the stinger, is shown in Fig. 5.4. In each case, no evidence of a second harmonic component in the input to the rings is evident. Thus, quadratic features in the ring response are not attributable to the input from the shaker. For the 1.7 mm thickness ring, as shown in Fig. 5.4b, a strong cubic component is observed. This is most likely due to the inherent cubic nature of electrodynamic shakers (Tomlinson, 1979). This feature seemed to be frequency dependent, present when driving the shaker at 204 Hz but not at 80 Hz. However, since only quadratic features are of interest in this study, a cubic peak of this relatively small magnitude is not significant.

The power spectrum of the response of the $n=0$ wavenumber for the 0.86 mm thickness ring, affine and orthogonal excitation configurations, is shown in Fig. 5.5. The dominant feature of both power spectra is the linear response peak at 80 Hz. This is due to the spatially concentrated force input, which is broadband in the wavenumber or spatial domain (including a $n=0$ wavenumber contribution). Thus, a linear response is generated at the $n=0$ wavenumber. A significant peak is also present at the second harmonic frequency, 160 Hz, for both

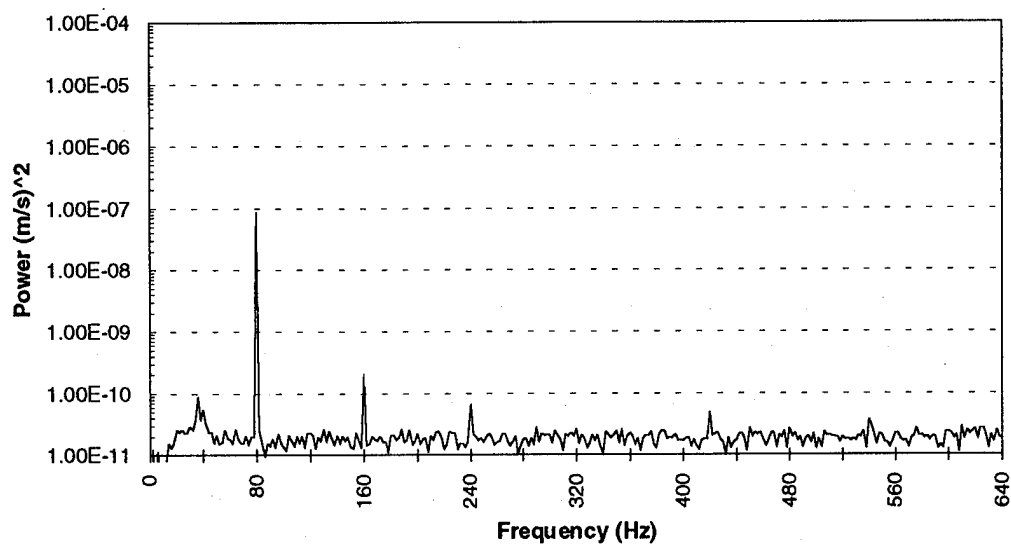


a.) 0.86 mm Thickness Ring

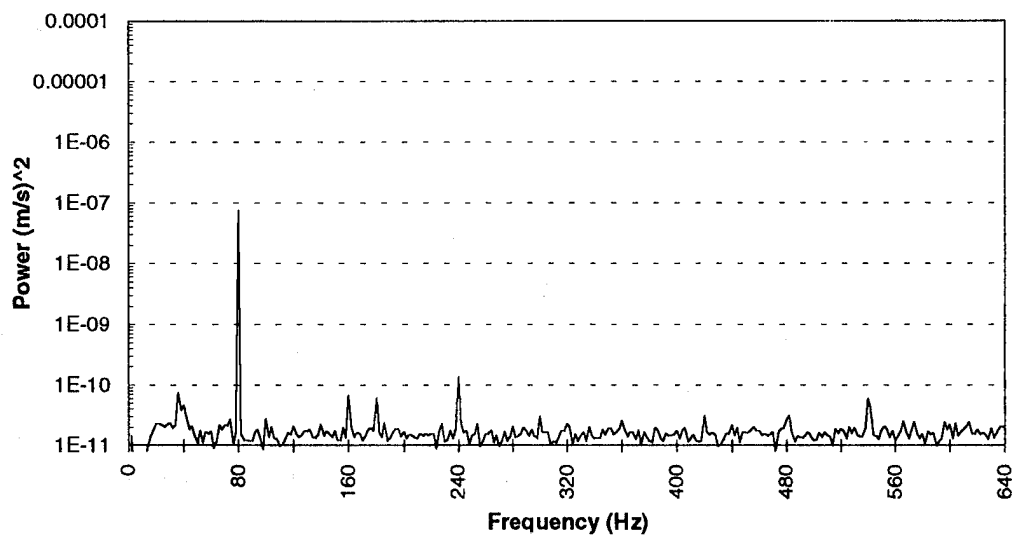


b.) 1.7 mm Thickness Ring

Figure 5.4: Frequency Spectrum of Excitation to Rings



a.) Affine Excitation Configuration



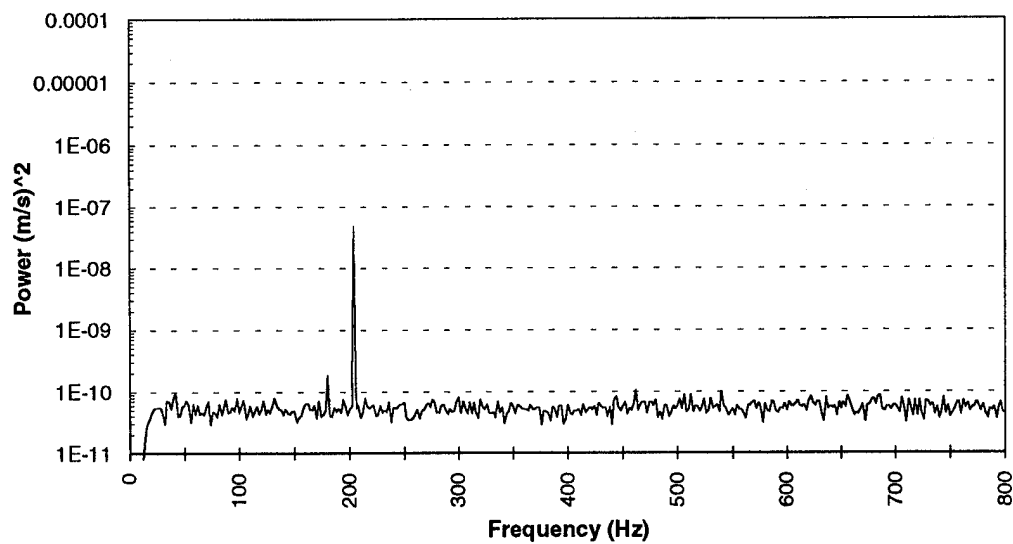
b.) Orthogonal Excitation Configuration

Figure 5.5: Power Spectrum of $n=0$ Wavenumber Response
for 0.86 mm Thickness Ring

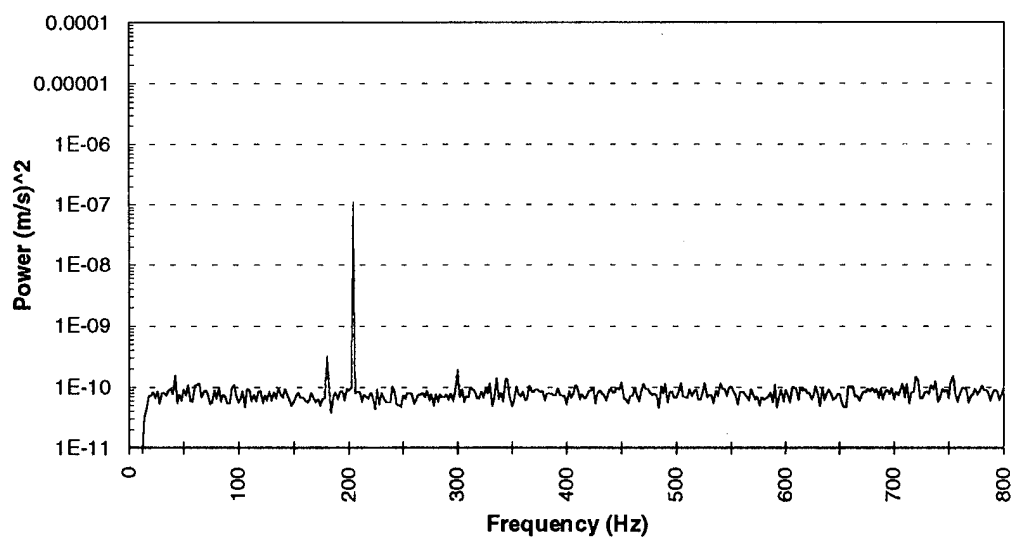
cases. Other peaks are present as well. However, these peaks are located at harmonics of 60 Hz and are attributed to contaminating 60 cycle noise. The peak at 35-40 Hz is also considered spurious. This peak was observed during the LDV calibration and is thus attributed to low-level noise produced by the hardware of this measurement system.

Comparing Figs. 5.5a and 5.5b, the amplitude of the 80 Hz peak is slightly greater, about 16%, for the affine configuration than for the orthogonal. However, for 20 averages, the standard deviation of the power spectral estimate is $\pm 22\%$ (Wilson, 1990); thus, this difference is not deemed significant. The same trend is observed for the 160 Hz peak associated with the quadratic response features. However, the difference here is much greater. This 160 Hz peak associated with the affine case is three times, or almost 5 dB, greater than the peak resulting from the orthogonal configuration. These results definitely submit evidence of the nonlinear coupling predicted. The quadratic response peaks of the $n=0$ wavenumber are of significant amplitude, only 25 dB below the linear response peaks. However, the enhancement of the linear response expected, due to imperfections, is absent. Also, the quadratic features of the $n=0$ wavenumber response seem to be strengthened by imperfections. This was not predicted by the numerical simulations of Chapter 4.

Figure 5.6 displays the response of the $n=0$ wavenumber for the 1.7 mm thickness ring. The linear response peaks are of the same order of magnitude as those of the 0.86 mm thickness ring. Yet, the quadratic peaks are now buried in the noise. The 204 Hz peak is greater, by a factor of approximately 2.2, for the orthogonal excitation configuration than for the affine case. Additionally, as observed by comparing Figs. 5.5 and 5.6, the noise floor for the 1.7 mm thickness ring measurements is higher, by approximately a factor of three, than the 0.86 mm thickness ring measurements. The same is also true when comparing the noise floor of the orthogonal case of Fig. 5.6b to that of the affine case. The noise floor for the orthogonal excitation is 2 to 3 dB greater than that for the affine excitation.



a.) Affine Excitation Configuration



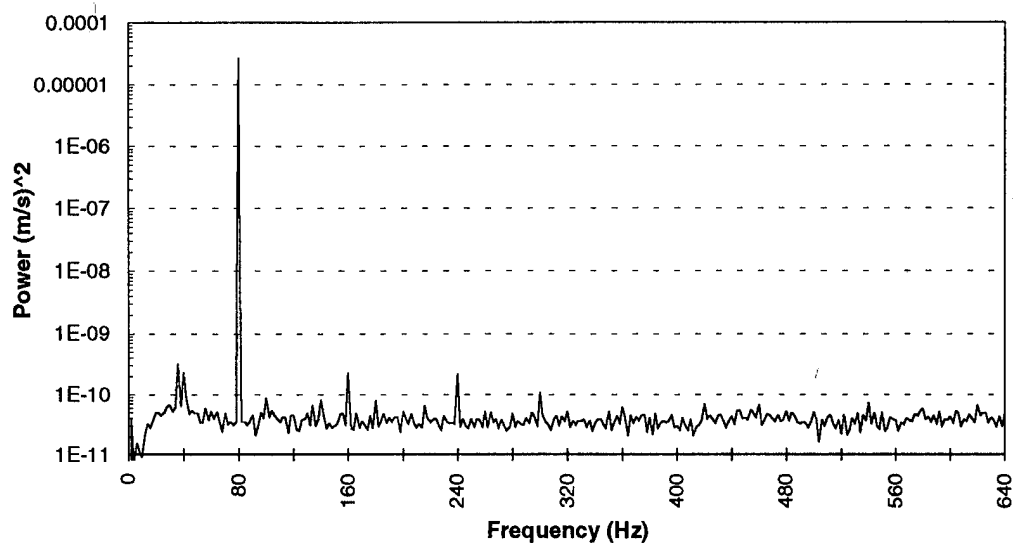
b.) Orthogonal Excitation Configuration

Figure 5.6: Power Spectrum of $n=0$ Wavenumber Response
for 1.7 mm Thickness Ring

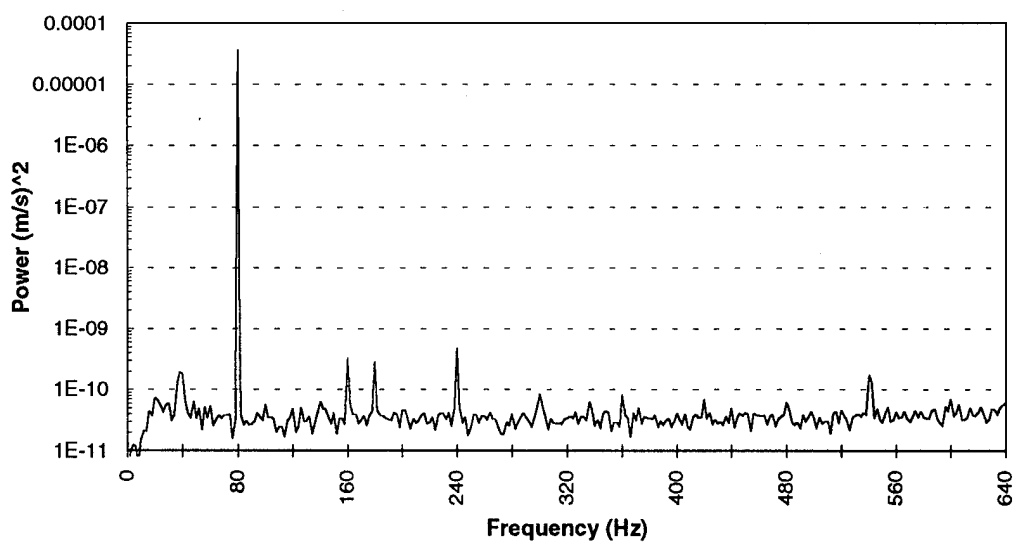
The increase in the noise floor is most likely responsible for the absence of discernible second harmonic peaks in the $n=0$ wavenumber responses. This is also a possible explanation for the increase in the linear response amplitude for the orthogonal case, as opposed to the affine case as predicted. The increase in the noise floor approximately matches the increase in amplitude between the two cases. This influence of noise is not as predominant in the response of the 0.86 mm thickness ring.

The $n=3$ wavenumber response power spectrum for the 0.86 mm thickness ring is shown in Fig. 5.7. Again the linear and quadratically nonlinear components at 80 and 160 Hz, respectively, are evident. The spurious 60 cycle noise peaks at 180 and 240 Hz should be neglected. The linear response peaks are of the same order of magnitude for the affine and orthogonal configurations, with the peak for the orthogonal case of slightly greater amplitude, about 35%. Similarly, the amplitude of the quadratic peaks are also approximately equal, with the peak associated with the orthogonal case slightly greater, about 25%. This is again unexpected, based on the hypotheses established and demonstrated numerically in Chapter 4.

These features could be attributed to the shifting of the natural frequencies due to the presence of imperfections, as indicated by the third term in Eq. 2.34a. This influence should be more prominent for thinner rings. The magnitude and direction of the shift is proportional to the amplitude of the n th imperfection component and the sign of the $\cos \phi_n$ term. For the excitation configuration used in this study, the theoretical natural frequency would be shifted up by about 2%. This shift would mean that for the same frequency, below the resonance frequency, the affine configuration produces a decreased response amplitude when compared to the orthogonal configuration. Thus, the linear and nonlinear features would be slightly attenuated and reflect this diminution of energy for the affine case.



a.) Affine Excitation Configuration



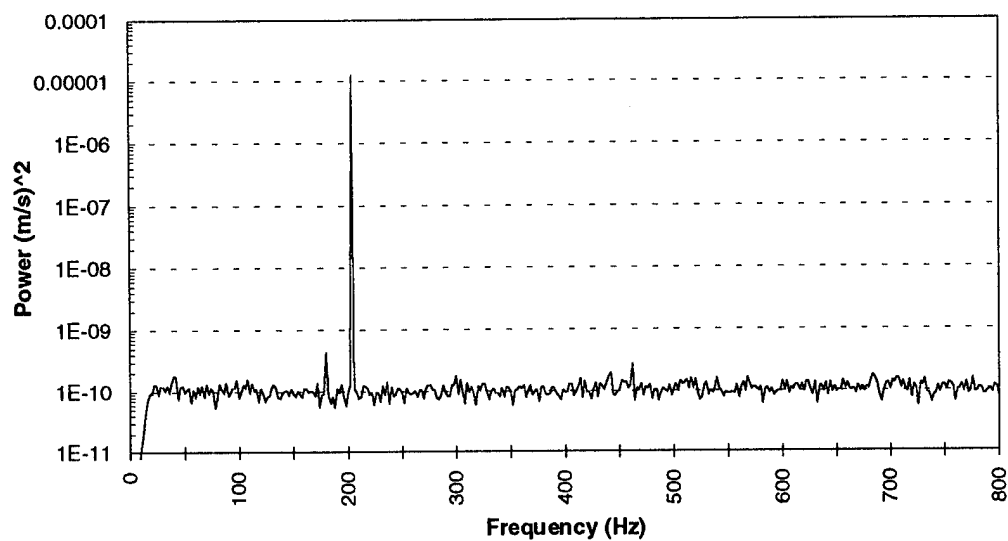
b.) Orthogonal Excitation Configuration

Figure 5.7: Power Spectrum of $n=3$ Wavenumber Response
for 0.86 mm Thickness Ring

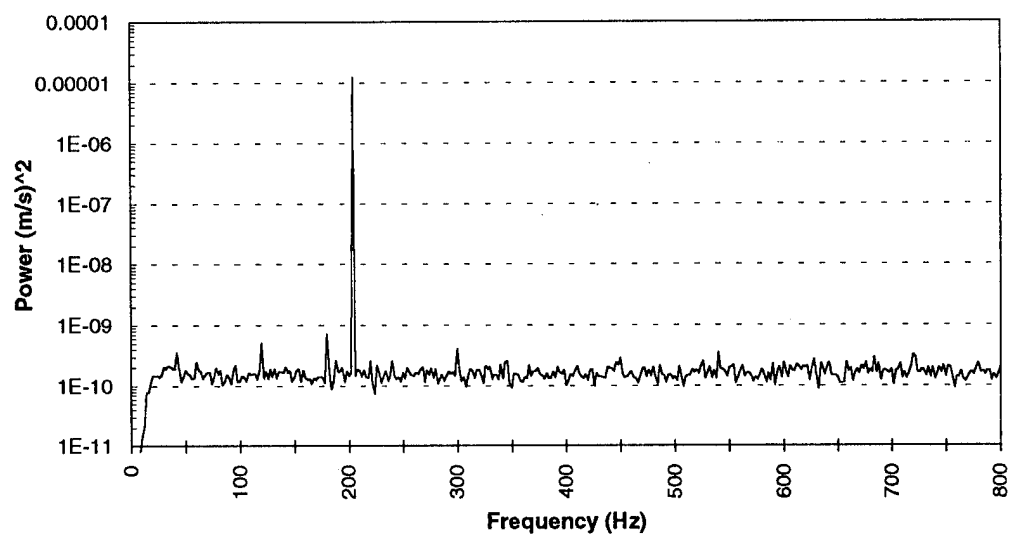
The increase in the strength of the quadratic features of the $n=0$ wavenumber response was not predicted by the numerical simulation, yet potential evidence of this trend is supported by the analytical study. The fourth term of Equation 2.36b reveals the linear coupling present for imperfections. This form of coupling also allows for the nonlinear, quadratic response of other wavenumbers to be coupled to the $n=0$ wavenumber response, thus enhancing the quadratic features of this mode. Another discrepancy between the numerical simulation and the experimental results is the strength of the linear response of the $n=0$ wavenumber compared to the quadratic response. This is likely due to disparate damping between the actual ring and the ring in the numerical simulation. It is suspected that the actual ring is more lightly damped than the numerical simulation ring; thus, the linear response amplitude in the experiment is greater.

The power spectrum of the $n=3$ wavenumber response for the 1.7 mm thickness ring is presented in Fig. 5.8. Again, the linear features are evident for both excitation configurations, while the quadratic features are not. For the affine and orthogonal excitation configurations, the magnitude of the 204 Hz peak is identical, as well. Also, consistent with the $n=0$ wavenumber response plots, the noise floor is higher for the power spectral response of this ring than it is for that of the thinner ring.

Figure 5.9 displays the bicoherence plots for the $n=0$ wavenumber response for the 0.86 mm thickness ring. For the affine configuration, the bicoherence value of the $f_1=f_2=80$ Hz is 0.79. As indicated in Fig. 5.9b, the bicoherence value of the $f_1=f_2=80$ Hz is 0.41 for the orthogonal configuration. This is consistent with the results of the numerical simulation and is expected when observing Fig. 5.5. However, now the increase in the bicoherence is not due to an increase in the signal to noise ratio of the linear peaks, as was predicted by the numerical simulations. The apparent cause now is the increase in the strength of the

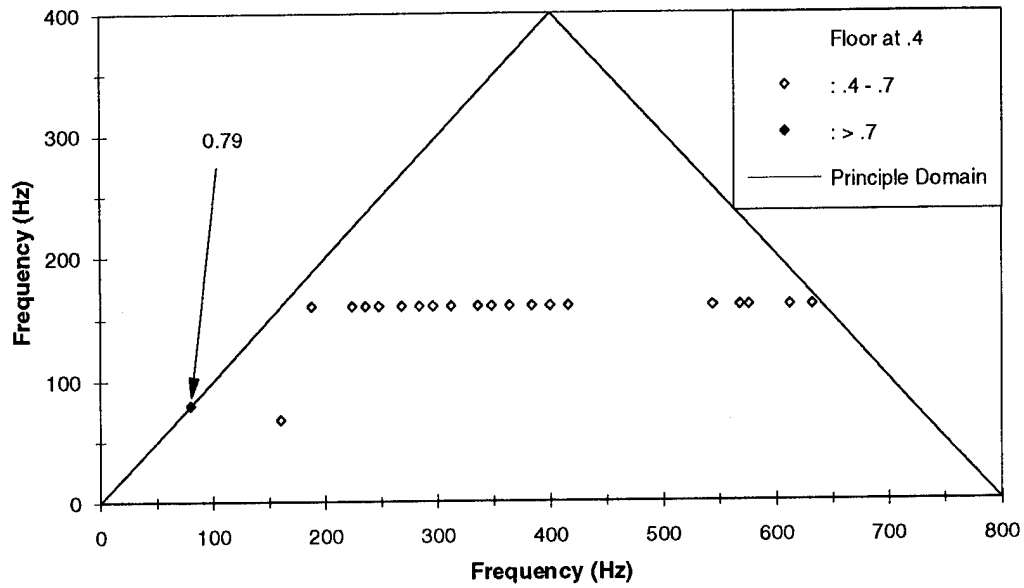


a.) Affine Excitation Configuration

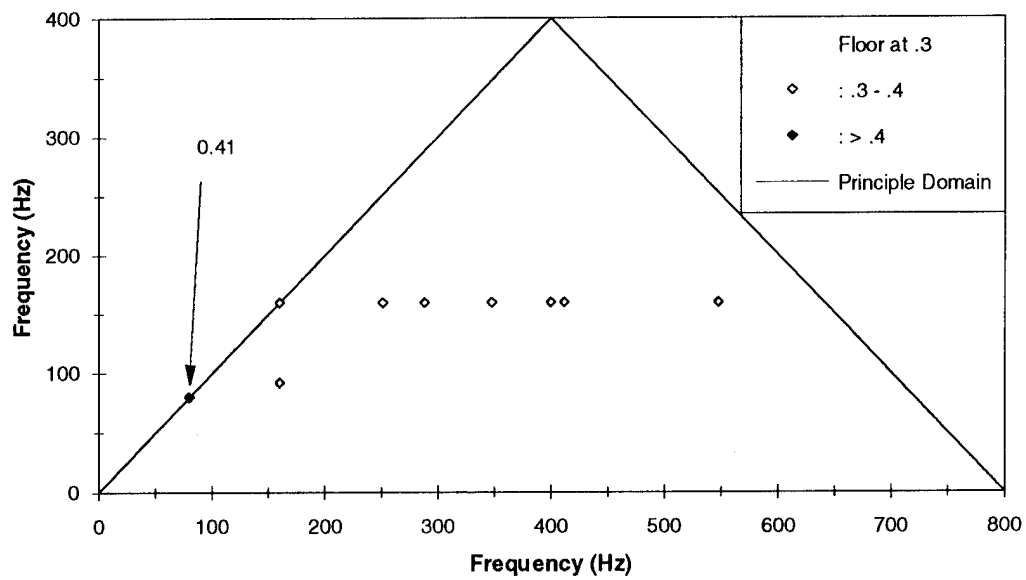


b.) Orthogonal Excitation Configuration

Figure 5.8: Power Spectrum of $n=3$ Wavenumber Response
for 1.7 mm Thickness Ring



a.) Affine Excitation Configuration



b.) Orthogonal Excitation Configuration

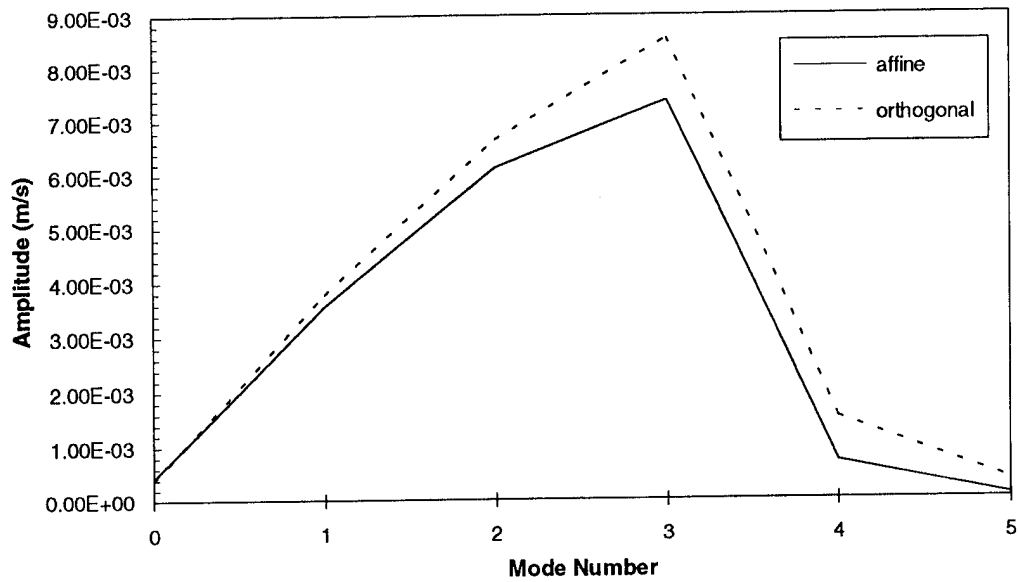
Figure 5.9: Bicoherence of $n=0$ Wavenumber Response
for 0.86 mm Thickness Ring

quadratic peak due to the affine excitation promoting enhanced quadratic coupling as seen from Eq. 2.34.

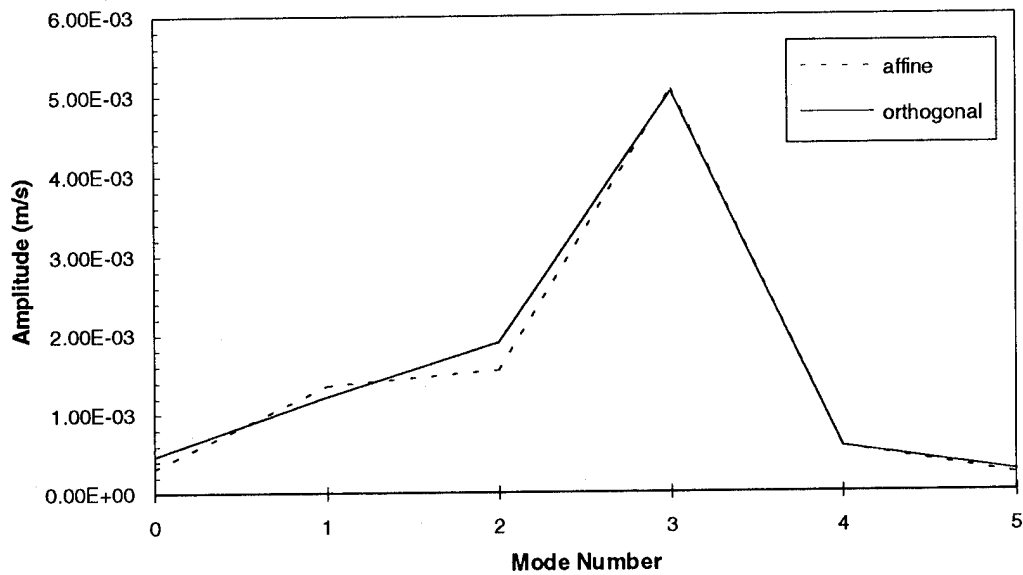
The wavenumber amplitudes for the linear response of each ring for both excitation cases is shown in Fig. 5.10. That is, this is the response of the ring, in the wavenumber domain, band filtered to the excitation frequency. For the 0.86 mm thickness ring, the response amplitudes of wavenumbers 1 through 5 for the affine configuration are less than for the orthogonal configuration. However, the distribution of energy for each excitation case is similar. As stated, a slight shift in the natural frequency of the $n=3$ wavenumber due to imperfections is the probable cause of this reduction. This wavenumber response is coupled to the other wavenumber responses due to imperfections; thus, a decrease in the linear response amplitude of this wavenumber can account for similar decreases in the other wavenumber response amplitudes.

The wavenumber response amplitudes are virtually equal for both excitation cases of the 1.7 mm thickness ring, with slight discrepancies at the $n=0$, 1, and 2 wavenumbers. The $n=0$ wavenumber response amplitude is greater for the orthogonal case than for the affine. For the response of the thinner ring, the energy is more evenly distributed over the spatial or wavenumber domain than for the 1.7 mm thickness ring.

Table 5.4 summarizes the bicoherence values produced by the responses of wavenumbers $n=0$, 2, 3, 4 for the 0.86 mm thickness ring. The highest bicoherence value, 0.79, is recorded for the $n=0$ wavenumber response of the affine configuration. This is almost twice the value obtained for the $n=0$ wavenumber response for the orthogonal case. A similar trend is observed for the bicoherence of the $n=4$ wavenumber response, where the bicoherence value for the orthogonal case is below the significance level. The opposite trend is present for the $n=3$ case, where the orthogonal configuration produces a higher bicoherence value



a.) 0.86 mm Thickness Ring, 80 Hz



b.) 1.7 mm Thickness Ring, 204 Hz

Figure 5.10 : Contribution of Individual Wavenumbers to Total Response

Table 5.4 : Bicoherence Levels at $f_1=80$ Hz, $f_2=187.5$ Hz
for 0.86 mm Thickness Ring *

Excitation Configuration	n=0	n=2	n=3	n=4
Affine	0.79	-	0.57	0.57
Orthogonal	0.41	-	0.68	-

(* "-" denotes bicoherence value is below 95% significance level)

than the affine case. No significant bicoherence values were produced by the wavenumber responses of the 1.7 mm thickness ring. This is expected since the thicker ring does not manifest as extensive nonlinear features as the thinner ring. Finally, Tables 5.5 and 5.6 summarize the magnitude of the linear response of the $n=0$ wavenumber for both rings and excitation cases.

This concludes this chapter on the experimental procedure and results. The next and final chapter presents the conclusions drawn concerning the effect of imperfections on the nonlinear vibrations of circular rings. These conclusions are based on the analysis of the experimental results, relying also on the results of the analytical study and predictions of the numerical simulations.

Table 5.5 : Amplitude of $n=0$ Linear Response Peak for 0.86 mm Thickness Ring

Excitation Configuration	Response Velocity (m/s)	Response Displacement (m)
Affine	4.20×10^{-4}	8.35×10^{-7}
Orthogonal	3.89×10^{-4}	7.75×10^{-7}

Table 5.6 : Amplitude of $n=0$ Linear Response Peak for 1.7 mm Thickness Ring

Excitation Configuration	Response Velocity (m/s)	Response Displacement (m)
Affine	3.16×10^{-4}	2.46×10^{-7}
Orthogonal	3.92×10^{-4}	3.67×10^{-7}

CHAPTER 6: CONCLUSIONS AND FUTURE WORK

This chapter provides concluding statements concerning the results and overall objectives of the study. Commentary regarding insight gained from the analytical, numerical, and experimental phases is included. Also, suggestions are proposed concerning possible reasons for unexpected or discrepant results. Finally, some remarks advising potential future work in the area of nonlinear vibrations of circular rings with imperfections finishes the chapter.

6.1 Conclusions

The results of the analytical study indicate the coupling present between wavenumbers and enhancement of nonlinear features in circular ring vibrations due to imperfections. The strength of these features depends on the amplitude and orientation of the imperfection composition. The coupling can provide for energy transfer from higher order wavenumber responses to lower order wavenumber responses. Even without the presence of imperfections, the inclusion of nonlinear features allows for the transfer of energy from higher order wavenumbers to the breathing mode, or $n=0$ wavenumber response. This transfer is due to nonlinear coupling between the $n=0$ and $n \geq 1$ wavenumbers.

The numerical simulation verifies some of the features predicted by the analytical study, namely, the transfer of energy from higher order wavenumbers to the $n=0$ wavenumber response. The imperfections provide for enhancement of the linear response of the $n=0$ wavenumber, due to linear coupling with higher order wavenumber responses. Similar features are displayed, in the absence of imperfections, due solely to the inclusion of nonlinearities. A strong nonlinear coupling component is present in the $n=0$ wavenumber response. The bicoherence

is also successful in both cases for detecting the quadratic relationship between the linear and second harmonic peaks in the responses of individual wavenumbers.

Perhaps the most definitive conclusion of the study is that evidence of nonlinear vibrations involving quadratic features is verified experimentally. Similarly, the results of the experimental study also indicate the nonlinear transfer of energy from higher order wavenumbers to the $n=0$ wavenumber response. This nonlinear transfer of energy manifests itself in a second harmonic response present at the $n=0$ wavenumber due to nonlinear coupling. The bicoherence is also successful in detecting the quadratic relationship between peaks in the response of individual wavenumbers.

Experimental evidence of the influence of imperfections on nonlinear ring vibrations also exists. However, the results here are not as definitive. The presence of imperfections does appear to enhance the nonlinear, quadratic response of the ring. They also appear to act as an energy transfer mechanism, transferring energy from higher order wavenumbers to the $n=0$ wavenumber response (breathing mode). Yet, the impact of imperfections was not as predicted by the numerical simulation. Namely, no significant effect on the linear response of the $n=0$ wavenumber due to geometric imperfections is observed. There is some support, present in the analytical study, explaining the findings regarding the impact of imperfections exhibited in the experimental results. However, further study is necessary to confirm these hypotheses.

6.2 Future Work

The results of the present study provide many suggestions for future and continuing work in the area of geometric imperfections and nonlinear ring vibrations. The numerical simulation results clearly exhibit an enhancement in the linear response of the $n=0$ wavenumber, breathing mode, due to coupling with the

wavenumbers containing imperfections. Verifying this experimentally would be of primary significance. One way this could be achieved is to compare the response of two rings of the same thickness, one with no or minimal imperfections, the other with a more exaggerated composition. In most practical situations, only one imperfection component can be emphasized or de-emphasized. Yet, the attenuation of other imperfection wavenumbers is not guaranteed. The anti-node, or maximum, of one imperfection component can coincide with the anti-node of another component. Conversely, the anti-node of one component can be in the proximity of the node, or minimum, of another component, thus complicating the results obtained from an affine or orthogonal excitation configuration.

An interesting research effort, extending the findings of the present work, would include the effects of a radially applied pre-load about the ring circumference. The pre-load creates a static deformation much as that associated with imperfections. Depending on the spatial distribution of pre-load, certain waveform components will have greater amplitudes, and thus greater influence on the response, than others. Also, nonlinear features could be more readily detectable. The addition of pre-load could create a static deformation large enough that the dynamic response would exhibit nonlinear features. The nonlinearities would be geometric in nature.

Other suggestions for continuation of the present study involve using increased spatial resolution to measure the wavenumber responses. This would help to minimize the experimental error associated with the spatial discretization technique. Also, testing rings comparable to the 1.7 mm thickness ring at a greater drive force level could prove fruitful. This is achieved simply by using a shaker capable of driving the ring at a larger drive force level without harmonic distortion. The rings under consideration for this study, of this thickness and greater, have a simpler imperfection composition than the thinner ring. Thus, analyzing the effect of a given imperfection component would be more tractable.

Appendix A: Data Reduction Procedure

This appendix describes the data reduction procedure used to process the laser Doppler vibrometer (LDV) and force gage signals obtained from each spatial location, such that the response of individual wavenumbers was estimated. Use of this procedure requires the following assumptions: the vibrations are steady state in nature and no companion modes or "traveling waves" are excited.

The response of the ring at a given spatial location and the input force to the ring are recorded simultaneously. The force gage output is used to synchronize the response data. As stated, the vibrations are assumed to be stationary. Thus, the force gage signals recorded with the LDV probe head at two different spatial locations are identical, provided the second signal is shifted to account for the time delay between the two measurements. The value of this shift is found using the cross correlation function. The cross correlation function is defined as follows:

$$R_j = \frac{1}{N} \sum_{i=1}^N a_i b_{i+j}, \quad 1 \leq j \leq N \quad . \quad (A.1)$$

In Eq. A.1, a is the force gage signal recorded for the first spatial measurement and b is the force gage signal recorded for any successive spatial measurement. The maximum value of R_j corresponds to the proper shift, j , necessary to align the two signals from the force gage. Thus, all signals are aligned with the signal recorded at the first spatial location.

For a single frequency excitation, the ring vibrations and excitation source have the same period. Therefore, shifting the LDV system signals by the appropriate values calculated by the correlation function synchronizes the response measurements as well. Now, the shifted response measurements represent the synchronous response of the ring at each spatial location. The shifted signals are

equivalent to signals which would be recorded at each spatial location by a separate measurement probe, sampling in parallel or simultaneously.

Now that the response signals are shifted, the data can be transformed to identify the wavenumber or modal content of the response. As stated, it is assumed that companion modes or "traveling waves" do not participate in the response. Therefore, the response is of the following form:

$$w(y,t) = \sum_{n=0}^N A_n(t) \cos\left(\frac{ny}{R}\right) \quad . \quad (A.2)$$

Representing Eq. A.2 in a discretized form, the following relation results:

$$w[y_m, i] = \sum_{n=0}^N A_n[i] \cos\left[\frac{ny_m}{R}\right] \quad , \quad (A.3)$$

where i and m are the temporal and spatial indices, respectively. Since the ring was sampled at eight equally spaced locations, from $\theta = \frac{\pi}{8}$ to $\theta = \pi$,

$$y_m = \frac{m\pi}{M} = \frac{m\pi}{8} \quad m = 1, \dots, M \quad ,$$

where M is the total number of spatial measurement locations.

Equation A.3 can be represented in matrix form:

$$\overline{CA}[i] = \overline{w}[i] \quad , \quad (A.4)$$

where \bar{C} is defined as follows:

$$C_{m,n} = \cos\left(\frac{ny_m}{R}\right) = \cos\left(\frac{nm\pi}{MR}\right) \quad m = 1, \dots, M; n = 0, \dots, M-1 \quad . \quad (A.5)$$

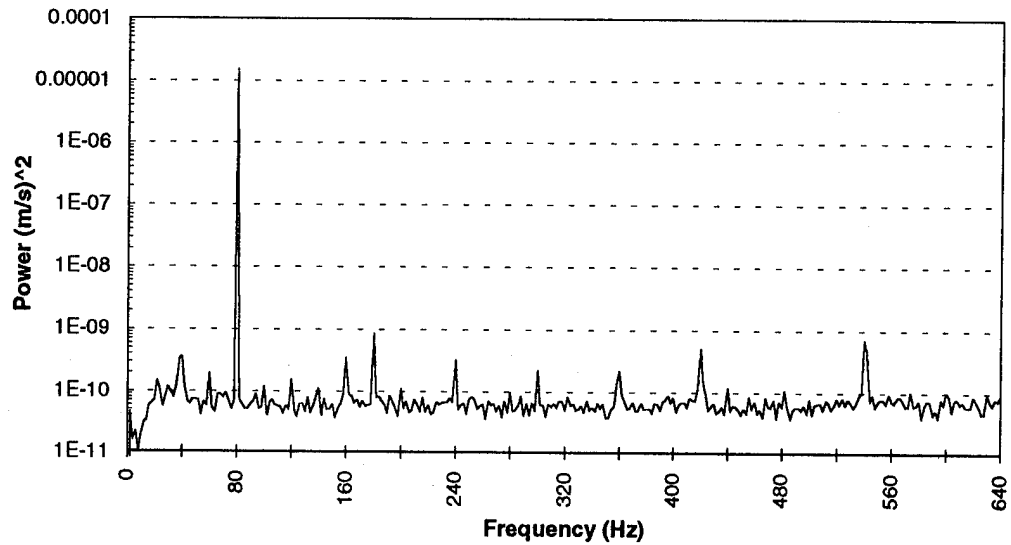
\bar{C} is a square matrix, with M rows and M columns. Thus, the number of modes used to represent the response is equal to M . In Eq. A.4, $\bar{w}[i]$ is a vector referring to the response measured at each spatial location at time i . $\bar{A}[i]$ represents the amplitude of the modal coefficients for the deformation of the ring at time i .

Solving Eq. A.4 for the wavenumber or modal coefficients, $\bar{A}[i]$,

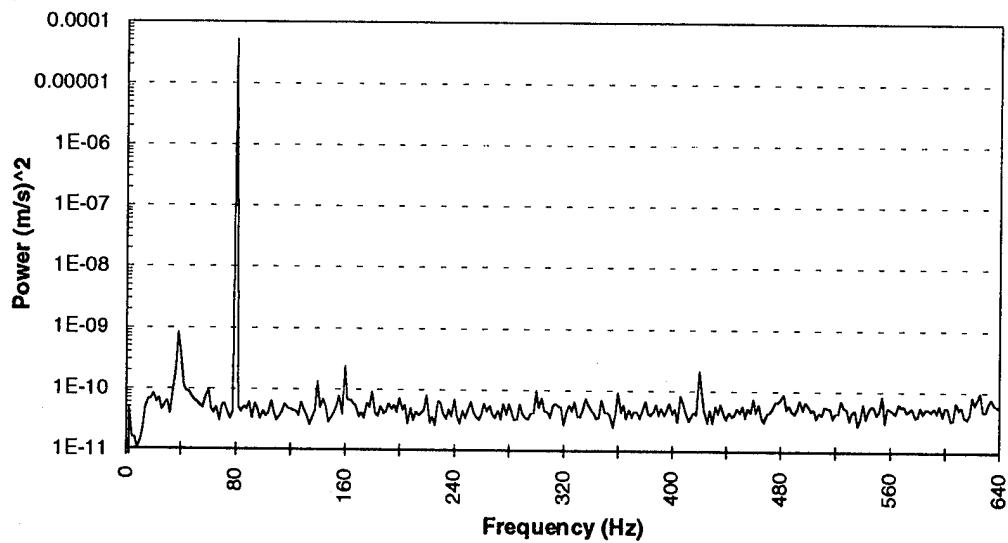
$$\bar{A}[i] = \bar{C}^{-1} \bar{w}[i] \quad . \quad (A.6)$$

Therefore, the deformation of the ring at a given instant in time, i , is calculated using Eq. A.6. The resulting vector, $\bar{A}[i]$, represents the amplitude of each mode, zero through $M-1$, at the instant i in time. Calculating this vector for each i yields the dynamic response of each mode.

Appendix B: Additional Experimental Results



a.) Spatial Location $m=1$



b.) Spatial Location $m=2$

Figure A.1: Power Spectrum of 0.86 mm Thickness Ring Response,
Affine Configuration

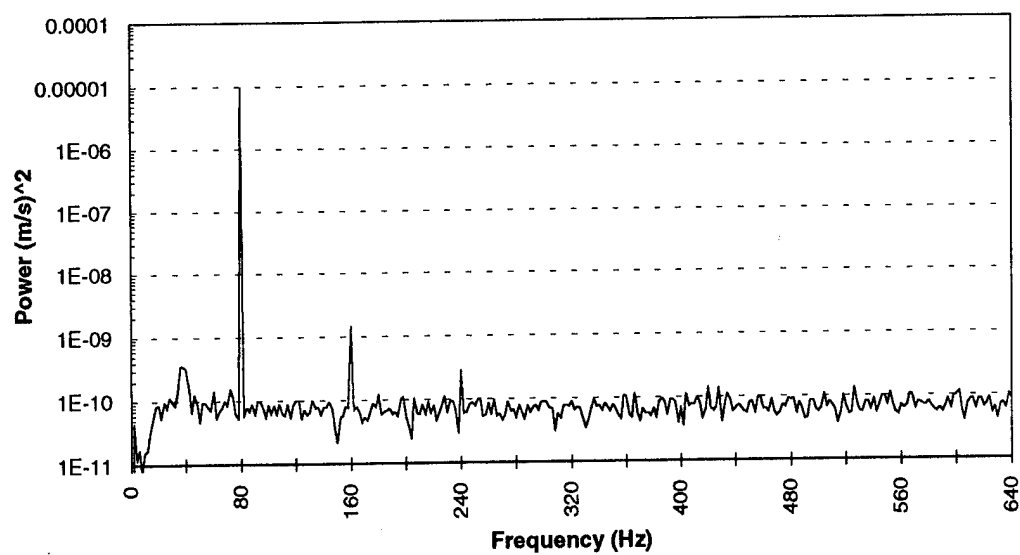
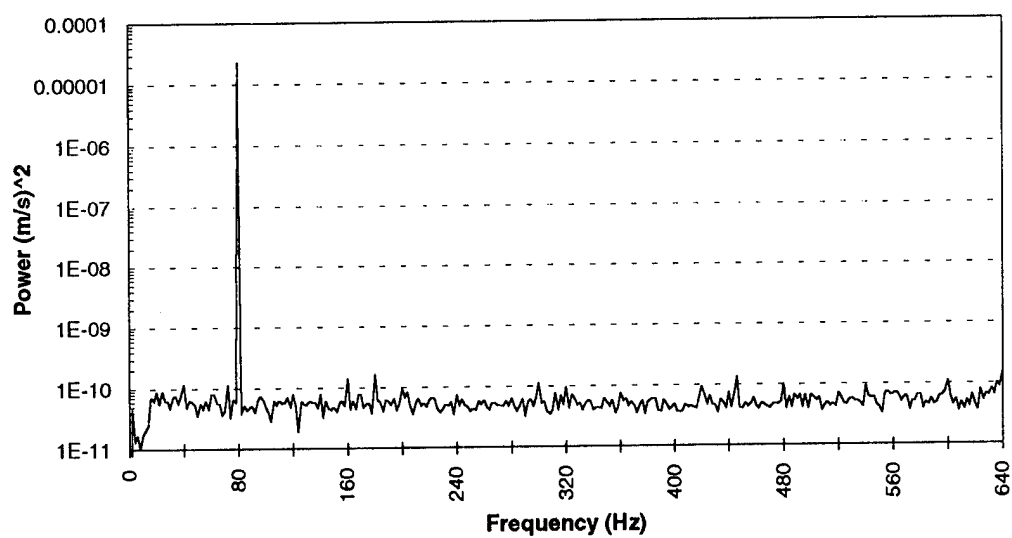
a.) Spatial Location $m=3$ b.) Spatial Location $m=4$

Figure A.2: Power Spectrum of 0.86 mm Thickness Ring Response,
Affine Configuration

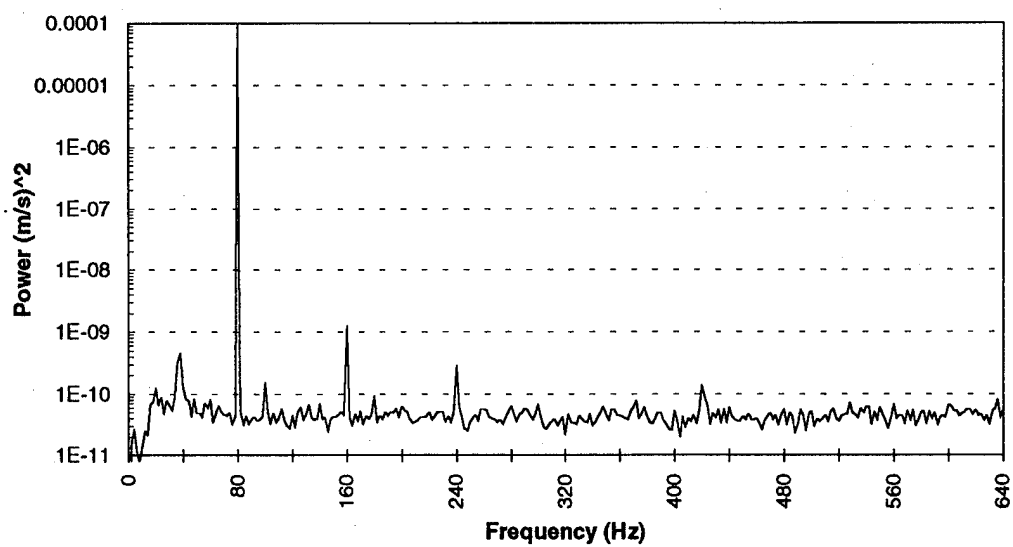
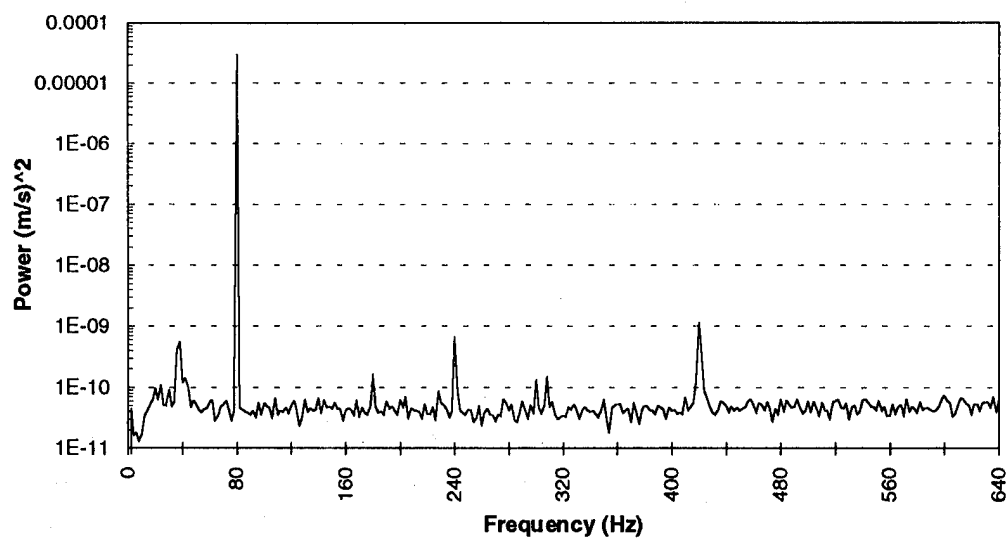
a.) Spatial Location $m=5$ b.) Spatial Location $m=6$

Figure A.3: Power Spectrum of 0.86 mm Thickness Ring Response,
Affine Configuration

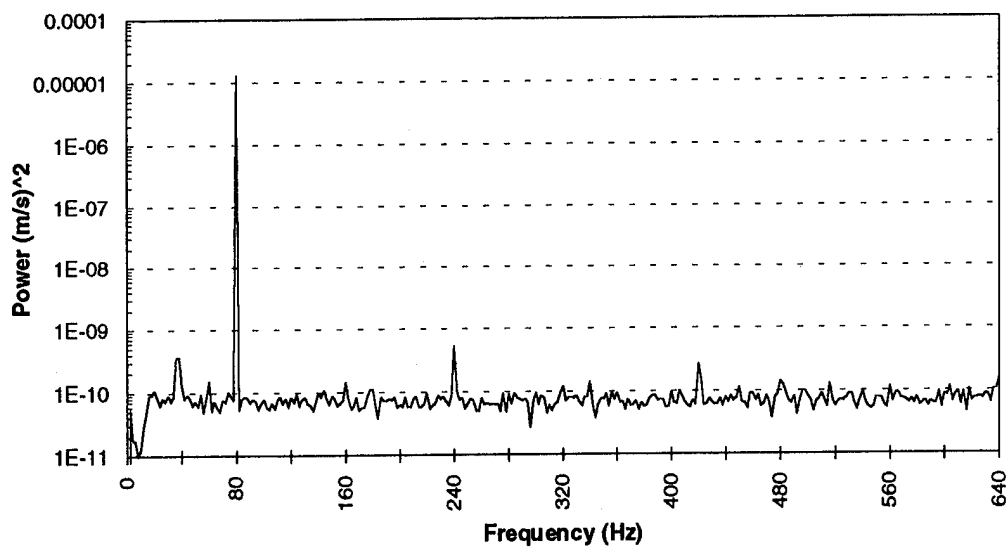
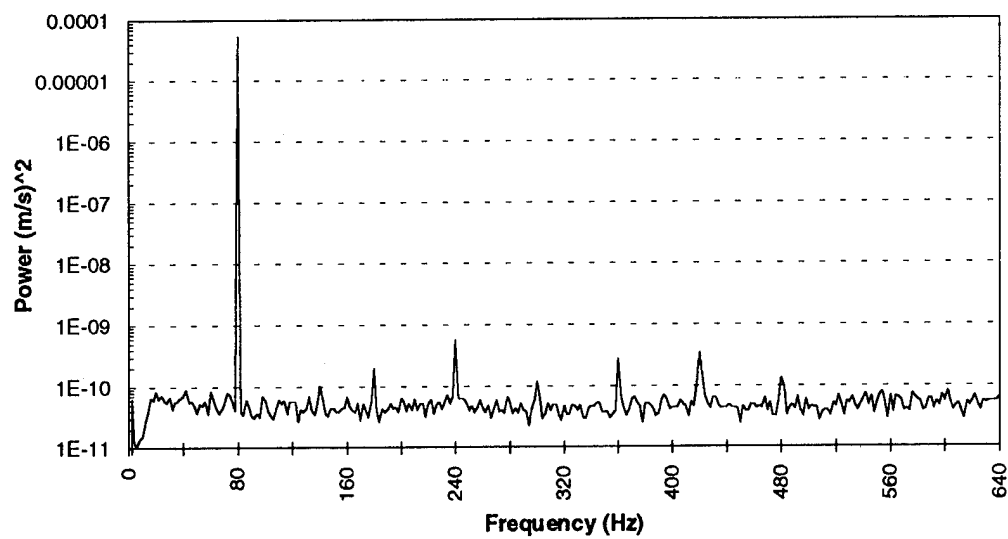
a.) Spatial Location $m=7$ b.) Spatial Location $m=8$

Figure A.4: Power Spectrum of 0.86 mm Thickness Ring Response,
Affine Configuration

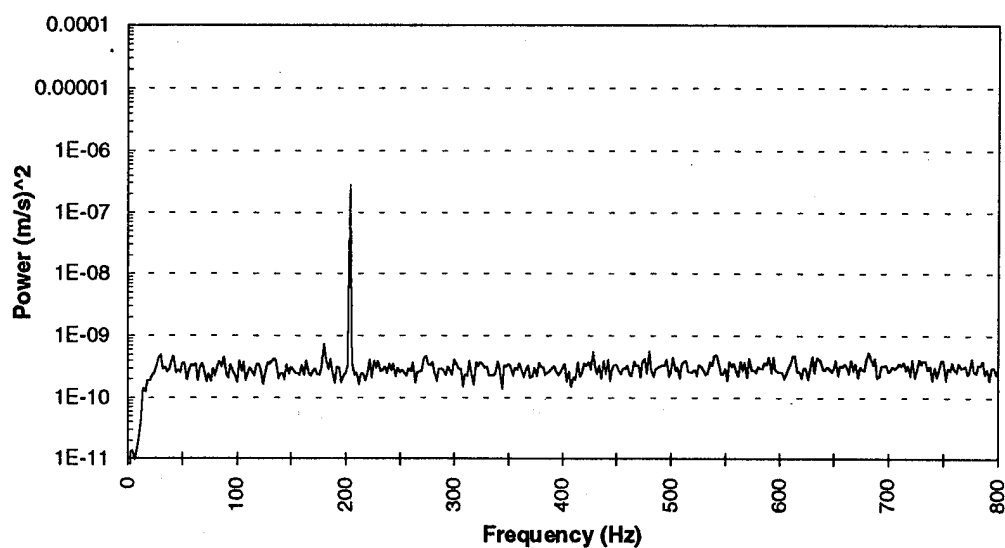
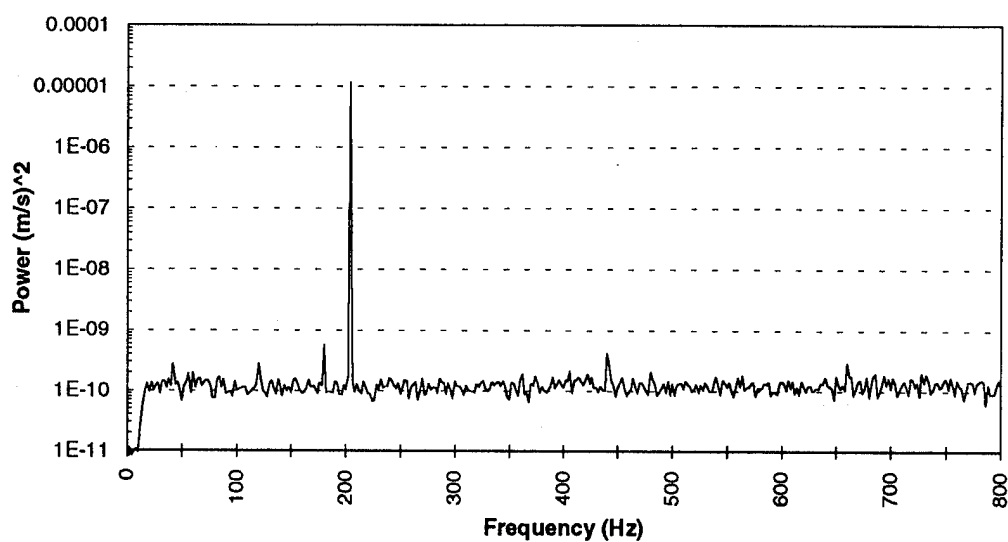
a.) Spatial Location $m=1$ b.) Spatial Location $m=2$

Figure A.5: Power Spectrum of 1.7 mm Thickness Ring Response, Orthogonal Case

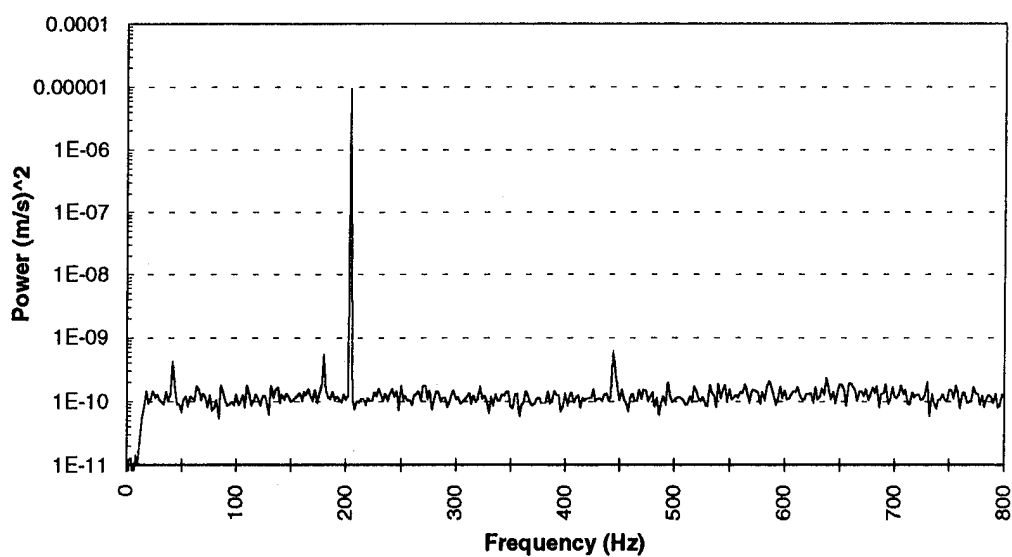
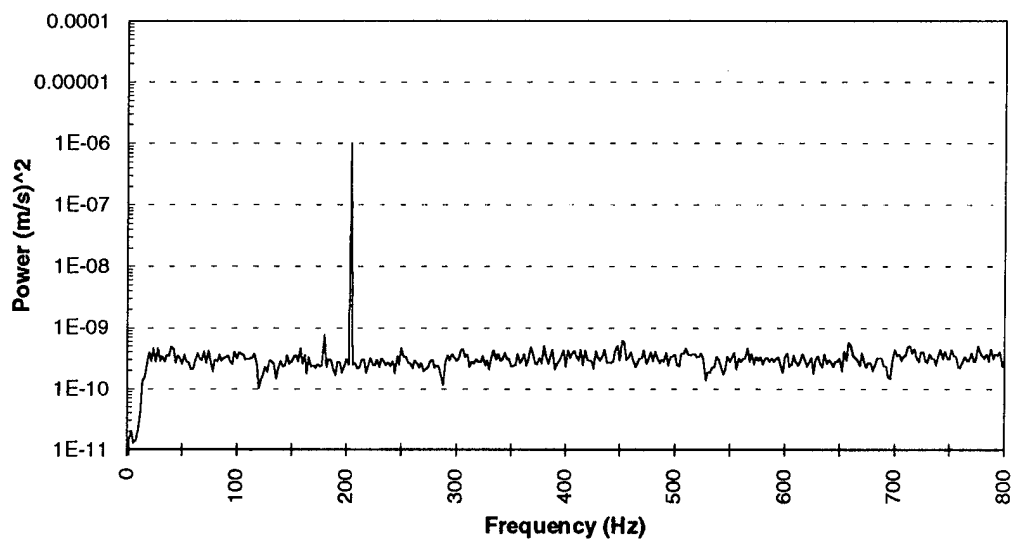
b.) Spatial Location $m=3$ b.) Spatial Location $m=4$

Figure A.6: Power Spectrum of 1.7 mm Thickness Ring Response, Orthogonal Case

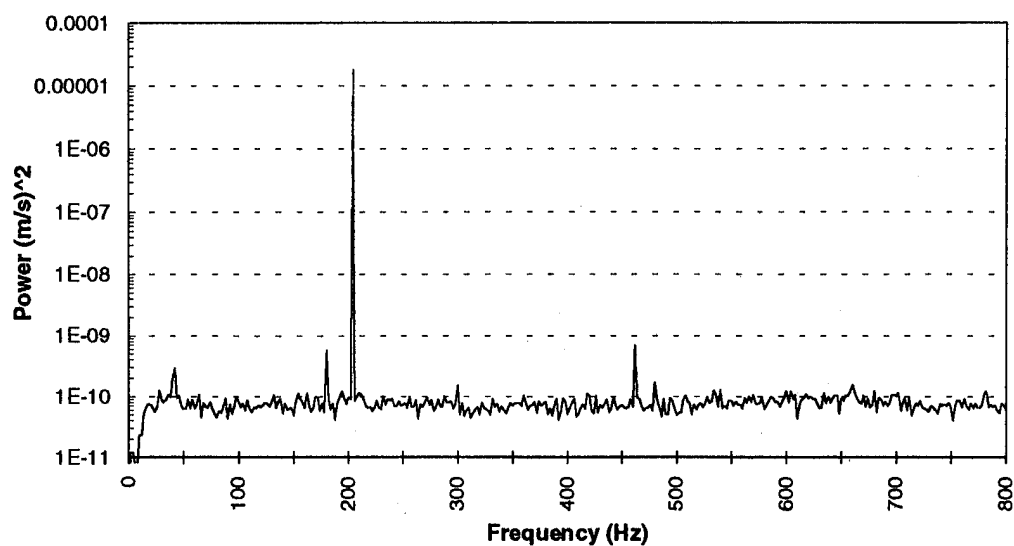
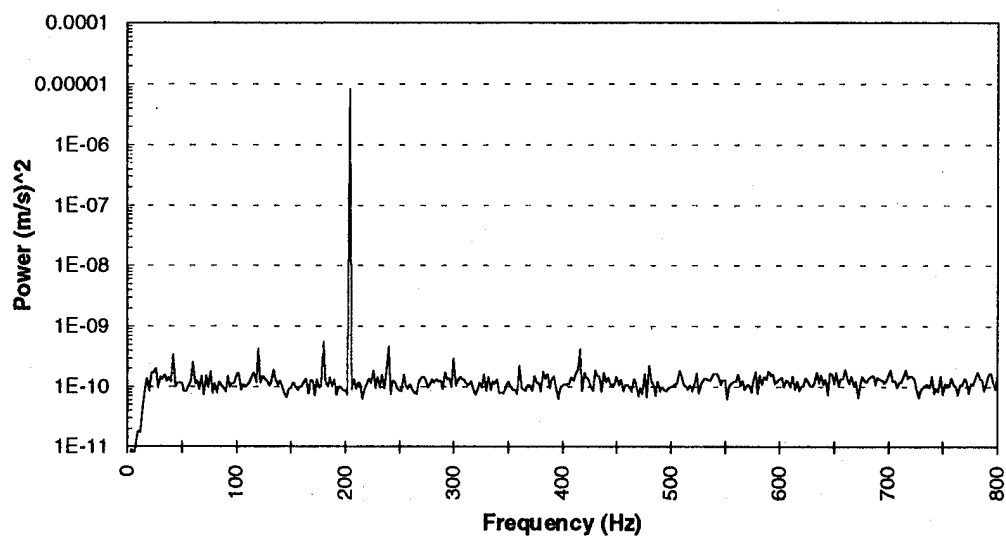
a.) Spatial Location $m=5$ b.) Spatial Location $m=6$

Figure A.7: Power Spectrum of 1.7 mm Thickness Ring Response, Orthogonal Case

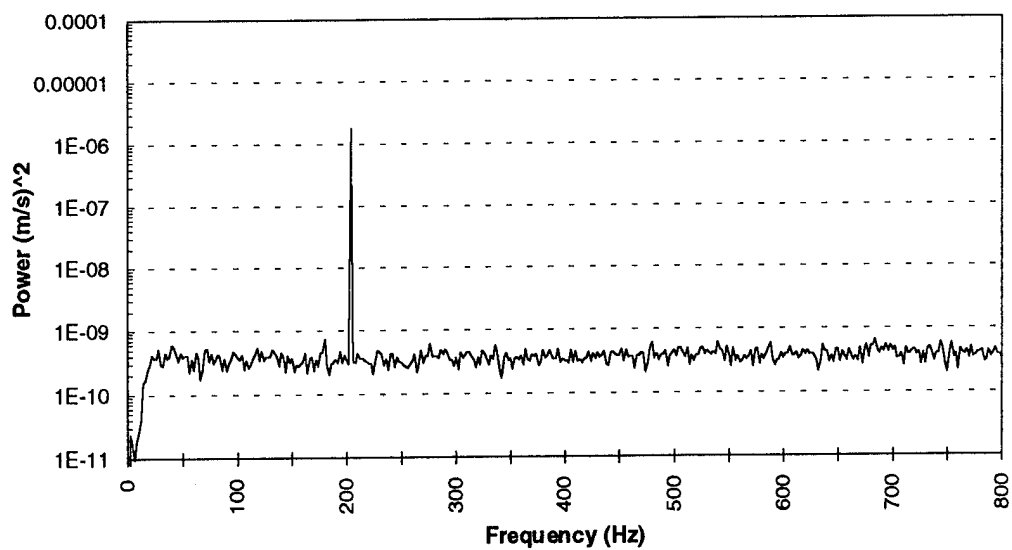
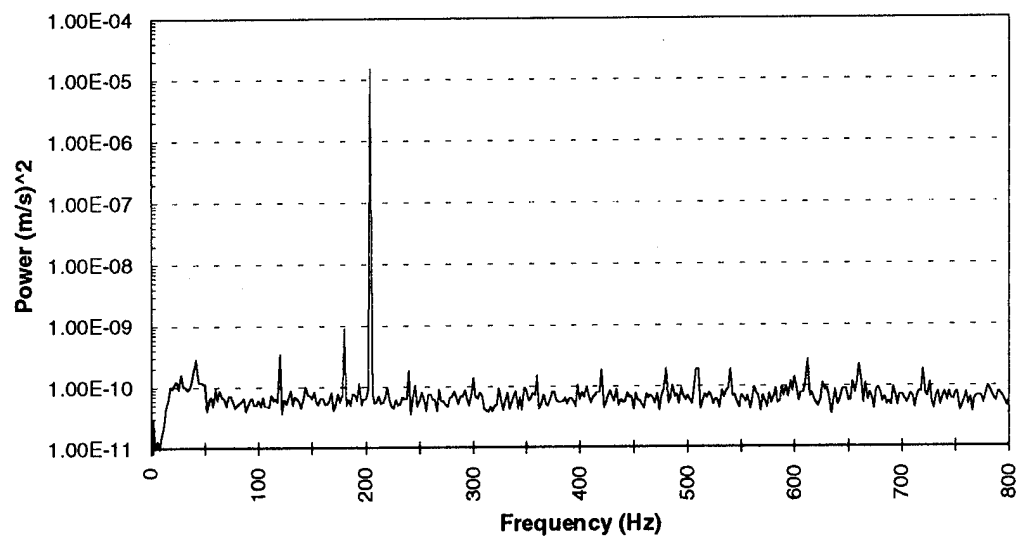
a.) Spatial Location $m=7$ b.) Spatial Location $m=8$

Figure A.8: Power Spectrum of 1.7 mm Thickness Ring Response, Orthogonal Case

References

Arbocz, Johann, and Babcock, Charles D., Jr., "The Effect of General Imperfections on the Buckling of Cylindrical Shells," *Transactions of the ASME, Journal of Applied Mechanics*, vol. 36, March 1969, pp. 28-38.

Blackstock, David T., Unpublished Class Notes for Acoustics II Course, The University of Texas at Austin, 1993.

Chu, Hu-Nan, "Influence of Large Amplitudes on Flexural Vibrations of a Thin Circular Cylindrical Shell," *Journal of Aerospace Science*, vol. 28, no. 8, Aug. 1961, pp. 602-609.

Corrado, Charles N., Jr., "Mid-Frequency Acoustic Backscattering from Finite Cylindrical Shells and the Influence of Helical Membrane Waves," Doctoral Dissertation, Massachusetts Institute of Technology, 1993.

Craig, Roy R., Jr., *Structural Dynamics: An Introduction to Computer Methods*, John Wiley and Sons, New York, 1981.

Cwach, Emil E., and Stearman, Ronald O., Experimental Observations on the Nonlinear Flexural Vibrations of Thin-Walled Circular Cylinders, AFOSR 68-0516, Air Force Office of Scientific Research, Arlington, VA, 1968.

Elgar, S., and Guza, R. T., "Statistics of Bicoherence," *IEEE Trans. on Acoustics, Speech and Signal Processing*, vol. 36, no. 10, Oct. 1988, pp. 1667-68.

Evensen, D. A., "Non-linear Flexural Vibrations of Thin Circular Rings," Doctoral Dissertation, California Institute of Technology, 1964.

Evensen, D. A., "Nonlinear Flexural Vibrations of Thin-Walled Circular Cylinders," NASA TN D-4090, National Aeronautics and Space Administration, Washington, D. C., 1967.

Fox, Douglas J., "Higher Order Spectral Investigations of Nonlinear Transverse Vibrations of Circular Rings," Master's Thesis, The University of Texas at Austin, 1993.

Hol, J. M. A. M., "The Effect of General Imperfections on the Natural Frequencies of Axially Compressed Stiffened Cylinders," Delft University of Technology: Dept. of Aerospace Engineering, The Netherlands, 1983.

Kim, Y. C., and Powers, Edward J., "Digital Bispectral Analysis and Its Applications to Nonlinear Wave Interactions," *IEEE Trans. Plasma Sci.*, PS-7, June 1979.

Lamb, James L., III, "Small Amplitude Interactions of Parametrically Excited Periodic Beams," Doctoral Dissertation, The University of Texas at Austin, 1993.

Liu, D. K., and Arbocz, J., "Damped Nonlinear Vibrations of Imperfect Thin-Walled Cylindrical Shells" LR-462, Delft University of Technology: Dept. of Aerospace Engineering, The Netherlands, 1985.

Liu, D. K., and Arbocz, J., "Influence of Initial Geometric Imperfections on Nonlinear Vibrations of Thin Circular Cylindrical Shells" LR-467, Delft University of Technology: Dept. of Aerospace Engineering, The Netherlands, 1985.

Liu, D. K., and Arbocz, J., "Influence of Initial Geometric Imperfections on Undamped Vibrations of Thin Circular Cylindrical Shells," LR-457, Delft University of Technology: Dept. of Aerospace Engineering, The Netherlands, 1986.

Mack, Lawrence R., and Yew, Ching-Hsie, "Nonlinear Flexural Oscillations of a Thin Elastic Ring," EMRL 1052, Engineering Mechanics Research Laboratory, The University of Texas at Austin, 1968.

Morley, L. S. D., "An Improvement on Donnell's Approximation for Thin-Walled Circular Cylinders," *The Quarterly Journal of Mechanics and Applied Mathematics*, vol. 12, pt. 1, 1959, pp. 89-99.

Novozhilov, V. V., *Foundations on the Nonlinear Theory of Elasticity*, Graylock Press, Rochester, N. Y., 1953.

O'Donnell, Richard B., "Bispectral Investigation of Active Control Processes," Master's Thesis, The University of Texas at Austin, 1990.

Powers, Edward J., "Polyspectral Analysis and Its Applications," Unpublished Class Notes, The University of Texas at Austin, 1990.

Rosen, Aviv, and Singer, Josef, "Effect of Axisymmetric Imperfections on the Vibrations of Cylindrical Shells under Axial Compression," *AIAA Journal*, vol. 12, No. 7, July 1974, pp. 995-997.

Stearman, Ronald O., and Lamb, James L., III, "Applications of Higher-Order Statistics to Aircraft Aeroelastic Stability and Fluid-Structural Interactions," Technical Report, Dept. of Aerospace Engineering, The University of Texas at Austin, August 1992.

Tomlinson, G. R., "Force Distortion in Resonance Testing of Structures with Electrodynamic Vibration Exciters," *Journal of Sound and Vibration*, vol. 63, no. 3, 1979, pp. 337-350.

Wilson, Gary R., "Detection and Time Delay Estimation of Non-Gaussian Signals in Noise," ARL-TR-90-25, Applied Research Laboratories, The University of Texas at Austin, 1990.

Wolinsky, M. A., "An Invitation to the Bispectrum," ARL-TR-88-7, Applied Research Laboratories, The University of Texas at Austin, 1988.

2 February 1995

DISTRIBUTION LIST
ARL-TR-95-3
Technical Report under
ARL:UT Independent Research and Development Program and
Grant N00014-90-J-1366

Copy No.

1	Office of Naval Research Department of the Navy 800 North Quincy Street Arlington, VA 22217-5660 Attn: Kam Ng, Code 334
2	Douglas Lake, Code 313
3	Geoff Main, Code 334
4	Commanding Officer Naval Research Laboratory Washington, DC 20375-5000 Attn: Library
5	Commanding Officer Naval Research Laboratory Stennis Space Center, MS 39529-5004 Attn: Library
6	Commanding Officer Naval Oceanographic Office Stennis Space Center, MS 39522-5001 Attn: Library
7	Commander Space and Naval Warfare Systems Command 2451 Crystal Drive Arlington, VA 22245-5200 Attn: Library
8	Commanding Officer Naval Command Control and Ocean Surveillance Center RDT&E Division 53560 Hull St. San Diego, CA 92152-5001 Attn: Library
9	Commander Dahlgren Division Naval Surface Warfare Center Dahlgren, VA 22448 Attn: Library

**Distribution List for ARL-TR-95-3 under ARL:UT IR&D Program and
Grant N00014-90-J-1366
(cont'd)**

Copy No.

- | | |
|----|---|
| 10 | Commanding Officer
Coastal Systems Station, Dahlgren Division
Naval Surface Warfare Center
Panama City, FL 32407-5000
Attn: Library |
| 11 | Commander
Carderock Division
Naval Surface Warfare Center
Bethesda, MD 20084-5000
Attn: Library |
| 12 | Officer in Charge
Naval Undersea Warfare Center
New London Detachment
New London, CT 06320-5594
Attn: Library |
| 13 | Advanced Research Projects Agency
3701 N. Fairfax Dr.
Arlington, VA 22203-1714
Attn: Library |
| 14 | Defense Mapping Agency
Hydrographic/Topographic Center
Washington, DC 20315-0030
Attn: Library |
| 15 | National Academy of Sciences
National Research Council
2101 Constitution Avenue
Washington, DC 20418
Attn: Library |
| 16 | National Aeronautics and Space Administration
Langley Research Center
Hampton, VA 23665
Attn: Library |
| 17 | Applied Physics Laboratory
The Johns Hopkins University
Johns Hopkins Road
Laurel, MD 20810
Attn: Library |

**Distribution List for ARL-TR-95-3 under ARL:UT IR&D Program and
Grant N00014-90-J-1366
(cont'd)**

Copy No.

- | | |
|----|---|
| 18 | Applied Physics Laboratory
The University of Washington
1013 Northeast 40th Street
Seattle, WA 98105
Attn: Library |
| 19 | Applied Research Laboratory
The Pennsylvania State University
P.O. Box 30
State College, PA 16801
Attn: Library |
| 20 | Scripps Institution of Oceanography (G&E)
The University of California, San Diego
La Jolla, CA 92093-0175
Attn: Library |
| 21 | Woods Hole Oceanographic Institution
86-95 Water Street
Woods Hole, MA 02543
Attn: Library |
| 22 | Advanced Research Projects Agency
Maritime Systems Technology Office
3701 North Fairfax Dr.
Arlington, VA 22203-1714
Attn: Dr. Theo Kooij |
| 23 | DTIC-OCC
Defense Technical Information Center
8725 John J. Kingman Road, Suite 0944
Fort Belvoir, VA 22060-6218 |
| 24 | Electrical and Computer Engineering Department
University of Texas at Austin
Austin, TX 78713
Attn: Prof. Ed Powers |
| 25 | Jay L. Lamb
Aeronautics Dept., BBE
The Johns Hopkins University
Applied Physics Laboratory
Laurel, MD 20723-6099 |
| 26 | Paul Daniel Till
777 N. Silver Springs, #1816
Wichita, KS 67212 |

**Distribution List for ARL-TR-95-3 under ARL:UT IR&D Program and
Grant N00014-90-J-1366
(cont'd)**

Copy No.

27	Martin Barlett, ARL:UT
28	Melvin J. Hinich, ARL:UT
29	Tom Muir, ARL:UT
30	Ronald O. Stearman, ARL:UT
31	Joe Thornhill, ARL:UT
32	Gary R. Wilson, ARL:UT
33	Signal Physics Group, ARL:UT
34	Library, ARL:UT
35 - 42	Reserve, Signal Physics Group, ARL:UT